Chem Soc Rev

ROYAL SOCIETY OF CHEMISTRY

REVIEW ARTICLE

View Article Online
View Journal | View Issue

Check for updates

Cite this: *Chem. Soc. Rev.*, 2026, **55**, 4244

Engineering MXene surfaces and heterostructure interfaces for efficient heterogeneous catalysis

Liang Tian,[a] Feiyan Xu,*[ab] German Sastre,[a] Ana Primo,[a] Jiaguo Yu[b] and Hermenegildo García*[a]

Received 30th October 2025

DOI: 10.1039/d5cs00376h

rsc.li/chem-soc-rev

The surfaces and interfaces of catalysts dictate activity, selectivity, and stability in heterogeneous catalysis, yet achieving atomic-level control over charge density flow and reaction energetics across these regions remains challenging. MXenes, a rapidly expanding family of two-dimensional transition-metal carbides, nitrides, and carbonitrides, offer an exceptional platform to address these challenges owing to their compositional tunability, rich surface terminations, and the strong influence of these groups on their physicochemical properties. Surface engineering provides the foundation for tailoring MXene reactivity, where controlled regulation of terminations, heteroatom doping, defect generation, and morphology enables precise tuning of active sites, adsorption energies, and redox potentials. Nevertheless, optimizing a single material may not provide sufficient control over surface charge dynamics and reaction energetics. For this reason, interface engineering that couples MXenes with metals, semiconductors, or carbon materials has become essential, as such heterostructures create Fermi-level equilibration, built-in electric fields, and orbital hybridization that govern charge transport and reshape catalytic pathways. Together, these hierarchical design strategies transform MXenes from simple conductive supports into dynamic catalytic mediators that bridge electro-, photo-, and thermocatalysis. This review summarizes recent progress in MXene surface and interface engineering, elucidates how atomic configurations regulate charge dynamics and catalytic behavior, and outlines design principles for programmable, self-adaptive, and stable MXene catalysts toward sustainable heterogeneous catalysis.

---

[a] *Instituto Universitario de Tecnología Química (CSIC-UPV), Universitat Politècnica de València, Avda. de los Naranjos s/n, 46022 Valencia, Spain. E-mail: hgarcia@itq.upv.es*

[b] *Laboratory of Solar Fuel, Faculty of Materials Science and Chemistry, China University of Geosciences, 68 Jincheng Road, Wuhan 430078, P. R. China. E-mail: xufeiyan@cug.edu.cn*

Liang Tian

Liang Tian is currently a pre-doctoral researcher at the Institute of Chemical Technology, Polytechnic University of Valencia, under the supervision of Prof. H. Garcia and Prof. G. Sastre. He received his B.Sc. (2015), M.Sc. (2018) in materials science and engineering from Wuhan University of Science and Technology, China. His research interests center on the controllable synthesis of nanomaterials and the structure–activity relationships in heterogeneous catalytic applications. His work involves investigating material synthesis mechanisms and catalytic properties using a combination of theoretical simulation calculations and in situ characterization techniques.

Feiyan Xu

Feiyan Xu is currently an Associate Professor at the School of Materials Science and Chemistry, China University of Geosciences (Wuhan). She received her PhD from Wuhan University of Technology in 2019 and has been a visiting scholar at the Polytechnic University of Valencia since December 2024. Her research focuses on the application and mechanistic investigation of composite nanophotocatalytic materials. By designing novel heterojunction photocatalysts, she aims to enhance photocatalytic activity for hydrogen evolution, CO_2 reduction, and CH_4 oxidation, while also exploring the underlying performance enhancement mechanisms and photocatalytic reaction pathways.

1. Introduction

Heterogeneous catalysis, a cornerstone of the modern chemical industry, underpins energy conversion, large-scale chemical synthesis, and environmental protection. Nearly 90% of chemical processes rely on heterogeneous catalysts, from ammonia synthesis in the Haber–Bosch process to petroleum refining and clean-fuel production. By enabling selective chemical transformations with reduced energy consumption, heterogeneous catalysis plays a pivotal role in the global energy transition and carbon-neutrality agenda.[1–5] It is central in hydrogen technologies such as water electrolysis and fuel cells, and in carbon utilization exemplified by CO_2 hydrogenation to methanol. Despite these achievements, conventional catalysts suffer from intrinsic trade-offs among activity, selectivity, and stability. Precious metals such as Pt and Pd offer excellent catalytic performance but are costly and scarce. Highly active nanoparticles are prone to sintering or poisoning, and improvements in selectivity often compromise reaction kinetics. These limitations arise from the difficulty of tailoring the catalytic surface microenvironments and from the complex relationships between surface structure and reaction performance. Consequently, the rational design of catalytic materials through atomic-level structural engineering and coordinated surface and interface regulation remains a pressing challenge.

German Sastre

German Sastre is Research Scientist at Instituto de Tecnología Quimica (ITQ). He made a postdoc at The Royal Institution of Great Britain with Sir Richard Catlow in 1995–1996. Since then, in ITQ, he employs computational chemistry methods to simulate synthesis of zeolites, catalytic and adsorption/diffusion processes, and physico-chemical properties of microporous materials (zeolites and metal–organic frameworks) and new families of materials such as Mxenes using big-data screening algorithms. He is, since 2013, member of the Structure Commission of the International Zeolite Association, and has served as scientific chair and member of research projects funding panels for FWO, NCN, GACR, EPSRC, FONCYT and FONDECYT.

Ana Primo

Ana Primo received her PhD in chemistry at the Universidad Politécnica de Valencia (Spain) in 2006. From 2007 to 2009, she did a postdoctoral stay in the Institute Charles Gerhardt of Montpellier, France. Currently, she is tenured scientist in the "Instituto de Tecnología Química" (UPV-CSIC). Her research interests include the synthesis of 2D materials (graphene, boron nitride, MXenes) and their application in catalytic and photocatalytic processes as CO_2 reduction for obtaining methanol or water splitting for H_2 production. She has published more than 100 papers, received more than 7000 citations, and has an h-index of 44.

Jiaguo Yu

Jiaguo Yu received his B.S. and M.S. in Chemistry from the Central China Normal University and Xi'an Jiaotong University, respectively and PhD in Materials Science from the Wuhan University of Technology (WUT). His research interests include semiconductor photocatalysis, photocatalytic hydrogen production, CO_2 reduction, perovskite solar cells, and electrocatalysis. He is Foreign Member of Academia Europaea (2020) and Foreign Fellow of the European Academy of Sciences (2020). He obtained the 35th Khwarizmi International Award (2022). His name is also in the lists of Highly Cited Researchers from Clarivate Analytics (previously Thomson Reuters) in Chemistry, Materials Science and Engineering from 2014–2023.

Hermenegildo García

Hermenegildo García is a full Professor at the Instituto de Tecnología Química of the Technical University of Valencia and Honorary Adjunct Professor at the Center of Excellence in Advanced Materials Research of King Abdullaziz University. He is working in the field of heterogeneous catalysis with porous solids as well as in the photocatalytic production of solar fuels having published over 900 articles. Prof. Garcia is Doctor Honoris Causa from the University of Bucharest, Spanish National Research award (2021), Janssen-Cilag award of the Spanish Royal Society of Chemistry (2011), Jaume I prize for Novel Technologies (2016) and Medal Lecturer award by the International Association for Advanced Materials (2021).

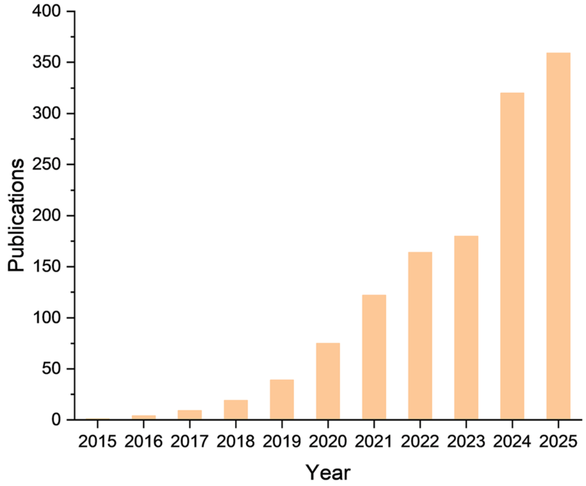

Fig. 1 The number of publications over the past decade obtained from a Scopus search crossing the keyword "MXene & Catalysis".

Two-dimensional (2D) materials have emerged as promising candidates to address these challenges because of their large surface-to-volume ratios, tunable electronic structures, and versatile surface chemistries.[6–8] Among them, MXenes, a family of transition-metal carbides, nitrides, and carbonitrides, stand out for their metallic conductivity, controllable compositions, broad chemical space, adjustable surface terminations, and distinctive electronic properties.[9–11] Beyond their applications in supercapacitors,[12–16] batteries,[17–20] electromagnetic shielding,[21–24] sensing,[25–27] anticorrosion coatings,[28,29] and biomedicine,[30–32] MXenes are now attracting increasing attention in heterogeneous catalysis.[33–37] Notably, research on MXene-based catalysts has advanced significantly, with a clear upward trend in publications over the years (Fig. 1). Compared with other 2D materials such as graphene or transition-metal dichalcogenides, MXenes provide greater tunability of active sites, stronger interfacial coupling, and superior charge-transport efficiency. Representative MXenes including $Ti_3C_2T_x$, V_2CT_x, and Mo_2CT_x have demonstrated notable catalytic activity and tunability in hydrogenation,[38] dehydrogenation,[39,40] and water-gas shift (WGS) reactions.[41]

Despite these advantages, pristine MXenes still suffer from critical limitations when used as standalone catalysts. Their surfaces oxidize readily, layered structures tend to restack, and the density of exposed active sites is limited, which collectively restricts efficiency and durability. To overcome these drawbacks, two complementary strategies have been developed.[42] On the one hand, surface engineering, which includes composition tuning, termination modulation, defect generation, and morphology control, allows precise regulation of electronic structure and surface chemistry. On the other hand, heterostructure construction by integrating MXenes with metals, metal compounds, carbon materials, or polymers creates interfacial synergies that facilitate charge transfer, optimize adsorption energetics, and accelerate reaction kinetics. The coordinated application of these strategies has proven effective in simultaneously improving catalytic activity and stability.

Research on MXene surface and interface engineering has advanced rapidly, and mechanistic insights are now being validated across electrocatalysis, photocatalysis, and thermocatalysis. While prior reviews have addressed MXene-based photocatalysts or selected composite architectures,[43–45] a unified, mechanism-oriented framework linking surface modification, heterostructure design, and catalytic function across all major reaction classes remains absent. To address this gap, the present review provides an integrated perspective that connects termination chemistry, defect evolution, interlayer engineering, and interfacial electronic structure with catalytic performance. The discussion begins with an overview of MXene synthesis routes and intrinsic physicochemical properties, followed by a systematic examination of surface engineering strategies. Subsequent sections analyze MXene-based heterostructures and elucidate how interfacial design governs catalytic pathways. The final part summarizes key challenges and emerging opportunities, including termination-controlled active-site design, AI-assisted MXene discovery, long-term stability engineering, and scalable synthesis routes suitable for practical implementation. By establishing a coherent surface–interface conceptual framework, this review provides a foundation for the rational development of next-generation MXene catalysts and highlights promising directions for future advances in heterogeneous catalysis.

2. MXene overview: basics and properties

MXenes are a class of 2D transition-metal carbides, nitrides, and carbonitrides that have attracted substantial attention over the past decade. The first MXene, $Ti_3C_2T_x$, was synthesized in 2011 by Gogotsi and co-workers through the selective etching of the Al layer from a Ti_3AlC_2-type MAX phase, thereby transforming a three-dimensional (3D) layered precursor into a 2D nanosheet.[46] In the parent MAX phases ($M_{n+1}AX_n$), M is an early transition metal, A is a group IIIA–VIA element such as Al, Ge, Sn, Si, or In, and X is C and/or N, giving rise to layered $M_{n+1}X_nT_x$ structures ($1 \leq n \leq 4$; T = –OH, =O, –F, –Cl) with M layers exposed at the surface (Fig. 2a).[47,48]

Since their initial discovery, MXenes have become a key platform in 2D materials research owing to their layered structure, high electrical conductivity, tunable surface chemistry, and large accessible surface area. Research has expanded from titanium-based carbides to a much broader family incorporating diverse early transition metals and non-metal elements, providing a rich compositional space for tuning physicochemical properties.[10,49] In parallel, diverse surface modification and interlayer engineering strategies allow precise regulation of electronic states and ion accommodation in the galleries. These advances have considerably broadened the application scope of MXenes, which now show promise across electrochemical energy storage (supercapacitors, lithium-, sodium-, and zinc-ion batteries), electromagnetic interference shielding, anticorrosion

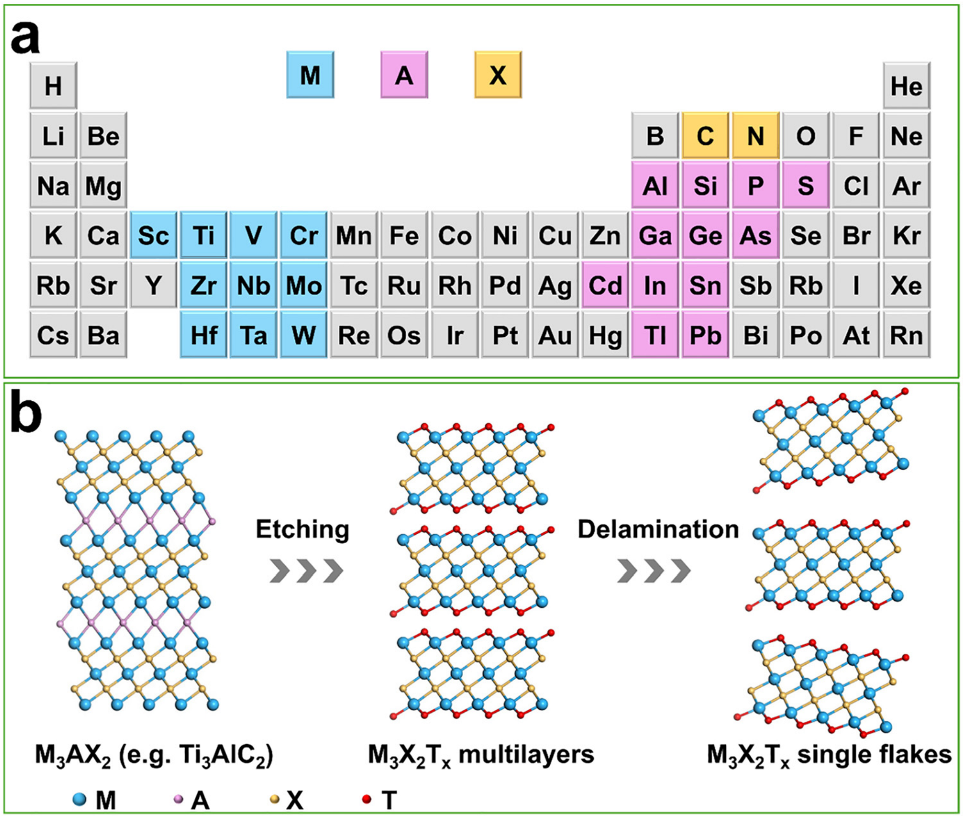

Fig. 2 (a) Fragment of periodic table illustrating "M", "A", and "X" elements that can form a MAX phase. (b) Schematic illustration of the etching synthesis of MXenes.

coatings, chemical sensing, biomedical applications, and environmental remediation.[50–55]

Substantial progress has also been made in expanding synthesis methods, understanding structural regulation mechanisms, and clarifying structure–property relationships, as comprehensively reviewed elsewhere.[56–61] Here, we only briefly introduce the principal preparation methods and catalysis-relevant properties of MXenes, focusing on features directly related to heterogeneous catalysis.

2.1. Synthesis routes and catalysis-relevant properties of MXenes

MXenes are most commonly prepared by selectively removing the A-site element from layered MAX phases ($M_{n+1}AX_n$), thereby exposing 2D M–X slabs with rich surface chemistry (Fig. 2b). The synthesis route determines surface terminations (T = –F, –O, –OH, –Cl, –S), defect density, interlayer spacing and hydration, intercalated species, and morphology (accordion-like stacks, few-layer colloids, films), all of which govern electronic structure, charge transport, adsorption energetics, and catalytic stability. Different synthetic methods thus often yield MXenes with markedly different termination ensembles and defect populations, leading to diverging catalytic behaviors and complicating mechanistic comparisons.

Established synthetic strategies include aqueous HF-based etching, fluorine-free hydrothermal alkali etching, molten salt routes (fluoride melts and Lewis acidic melts), electrochemical etching and purely physical exfoliation. In parallel, bottom-up methods such as salt templating and chemical vapour deposition (CVD) expand the accessible compositions and offer precise control over layer number and surface terminations (Fig. 3). These routes differ in scalability, environmental compatibility and termination control, providing complementary tools to tailor MXenes for thermo-, electro-, and photocatalytic applications, but the sensitivity of termination chemistry to small variations in precursor quality or moisture also introduces reproducibility challenges across independent studies.

2.1.1. Synthesis routes and termination control

Fluoride-based etching. Direct hydrofluoric acid (HF) etching[11] and *in situ* HF generation using fluoride salts with mineral acids[62–64] are the most established approaches to MXenes. They efficiently remove the A-layer and yield MXenes that are typically terminated by mixed –F, –O and –OH groups.[65,66] Intercalation of small cations or organic species facilitates delamination to few-layer colloids and freestanding films.[67,68] These advantages explain the central role of fluoride-based etching in early MXene research. For catalysis, however, the fluorine-rich termination ensemble presents important limitations. Strongly electronegative –F groups lower electronic conductivity, modify the work function and can partially block surface active sites. As a result, MXenes obtained by HF or fluoride molten salts often require post-treatments such as thermal annealing, alkali washing or

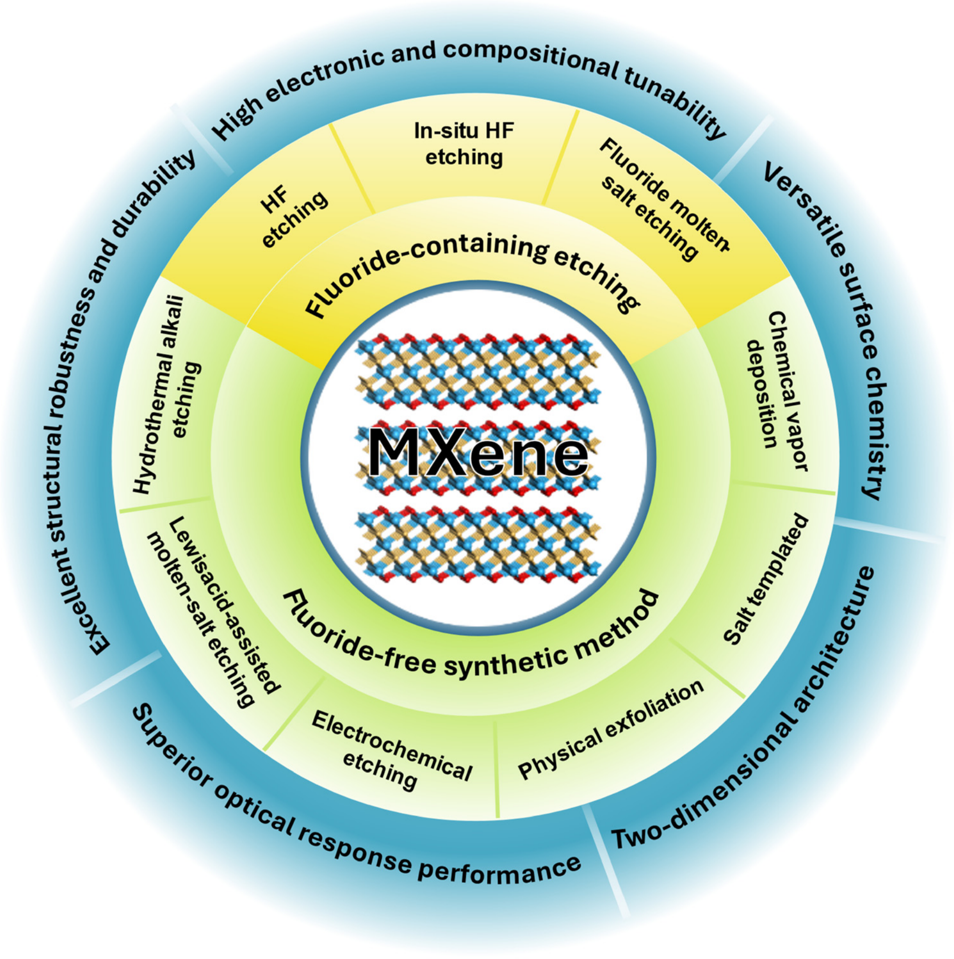

Fig. 3 Synthesis techniques and advantages of MXene catalysts.

plasma modification in order to enrich –O or –OH terminations and recover favourable electronic properties.[69–71] Fluoride molten-salt routes share similar F-rich surfaces,[72,73] so both liquid- and molten-fluoride methods generally need subsequent defluorination when catalysis-oriented electronic properties and active-site accessibility are required.[74,75]

Fluorine-free etching. Hydrothermal alkali etching[74] and Lewis-acidic molten-salt methods[76,77] have been developed in order to avoid fluorine and to obtain cleaner active surfaces. Concentrated alkaline solutions under hydrothermal conditions convert the A-site element into soluble aluminate and leave MXenes predominantly terminated by –O and –OH groups.[78] These fluorine free MXenes usually show higher intrinsic conductivity, improved hydrophilicity and more accessible active sites, which are advantageous for electrocatalysis and thermocatalysis. The main limitations are narrow processing windows and strong parameter sensitivity (risk of incomplete etching or overoxidation), together with high operating temperatures and metallic byproducts for molten salts, which can cause batch-to-batch variations in crystallinity and defect density.

Electrochemical etching. Electrochemical etching offers a more environmentally benign and electronically programmable alternative.[79] In this method, the MAX phase serves as the anode in an electrolyte that can be acidic, alkaline, neutral salt based or even molten. The A-site element is oxidised under an applied potential and removed as soluble complexes, while simultaneous intercalation of cations expands the interlayer spacing and promotes delamination. Because fluoride reagents are not required, the nature of surface terminations is largely dictated by the electrolyte. Chloride media introduce –Cl groups, alkaline media favour –O and –OH terminations,[80,81] and sulfur-containing electrolytes can incorporate –S species. This high degree of control over termination ensembles, work function and defect distribution is particularly attractive for catalysis. At the same time, overly high bias or prolonged anodisation can induce overetching or partial transformation to carbide-derived carbon, and the strong dependence of termination chemistry on local potential and cell geometry leads to noticeable variability in catalytic performance among ostensibly similar electrochemically prepared MXenes.

Physical exfoliation. Physical exfoliation relies on mechanical forces such as high power ultrasonication,[82] ball milling[83] or laser ablation[84,85] to separate pre-activated MAX phases or partially-etched precursors into thinner sheets. These techniques generally preserve the intrinsic surface stoichiometry and termination fidelity of the MXene framework. Although yields are modest and lateral sizes are often limited, the products are especially valuable for mechanistic studies because they allow the intrinsic influence of structure and anisotropy to be examined without strong chemical modification. However, their low throughput, heterogeneous flake thickness and defect distributions limit direct use in large-scale catalysis and complicate quantitative comparison with chemically etched analogues.

Bottom-up synthesis. Bottom-up strategies, primarily salt templating and CVD, complement top-down etching routes and extend the accessible MXene space to compositions that cannot be obtained from MAX phases. Salt templating confines the growth of layered intermediates inside salt matrices and enables subsequent conversion to nitride-type MXenes with clean, fluorine free surfaces and good crystallinity.[86] CVD directly deposits MXene films such as Mo_2C or Ti_2CCl_2 on suitable substrates while allowing fine control over thickness, lateral size and termination composition.[87–89] These methods are particularly useful for preparing well defined heterostructures, membranes and device grade electrodes for catalytic studies. Their drawbacks include high temperature and energy demands, limited throughput, and open questions regarding film uniformity and scalability for realistic catalytic modules.

Top-down routes, including HF based, fluorine free and electrochemical etching as well as physical exfoliation, dominate current MXene synthesis because they are experimentally accessible and can produce substantial quantities of material. The associated termination ensembles are largely set by the reaction medium, and post-synthetic termination engineering is usually required for catalytic optimisation. Bottom-up methods provide cleaner and more precisely controlled structures and surfaces, although at higher experimental cost. In all cases, the synthesis route establishes the initial termination chemistry, defect landscape and interlayer structure, which in turn govern the density, nature and stability of active sites in MXene-based catalysts. Despite significant progress, inconsistencies across studies and the sensitivity of MXene chemistry to subtle synthetic variables remain major barriers to establishing universally accepted structure–function relationships. Reducing this synthetic variability is essential for reliable catalyst design and for assessing the true potential of MXenes in practical catalytic processes.

2.1.2. Key properties for heterogeneous catalysis. The synthesis-dependent structural and chemical features described above translate into a set of physicochemical properties that make MXenes highly attractive platforms for heterogeneous catalysis.[10] These properties can be grouped into five main aspects. It is important to note that many reported catalytic performances depend strongly on synthesis-specific features such as termination distribution or defect density, which explains why different studies occasionally reach conflicting conclusions about the same MXene composition.[90]

Electronic and compositional tunability. MXenes exhibit remarkable compositional flexibility, since many early transition metals and both carbon and nitrogen can be incorporated into the $M_{n+1}X_n$ framework.[91] This modular chemistry allows systematic adjustment of the metal to nonmetal ratio, coordination environment and crystal symmetry, and therefore precise tuning of the electronic configuration.[47] Substituting different metals or forming multimetallic and high entropy MXenes alters the distribution of d orbitals and the density of states near the Fermi level, which provides a direct lever to regulate the binding strength of key intermediates and the kinetics of multielectron transfer processes.[92] In addition, most MXenes show metallic or quasi-metallic conductivity that supports fast charge transport and minimises resistive losses in electro- and photocatalytic systems.[93] The work function and Fermi level can be further adjusted through compositional and termination engineering, which facilitates energy level alignment with coupled semiconductors, cocatalysts and adsorbed molecules. At the same time, this high tunability implies that even small variations in composition or termination can markedly change catalytic activity, underscoring the need for rigorous reporting and control of synthetic conditions.

Surface chemistry and catalytic microenvironment. The surface chemistry of MXenes is highly adaptable. Terminations such as –O, –OH, –F, –Cl and –S, together with vacancies, edges and heteroatom dopants, define the local catalytic microenvironment. Termination engineering by chemical substitution, exchange reactions or annealing allows deliberate adjustment of surface hydrophilicity, charge density and work function, which shifts adsorption free energies and electron transfer kinetics.[94,95] Defect engineering introduces low coordination sites and localised states that often serve as catalytic hot spots.[96–98] MXenes also provide robust supports for single atoms, nanoparticles and molecular complexes, since their surfaces contain abundant functional groups and strong metal support interactions.[99,100] Such hybrid structures enable strong electronic coupling and tailored charge transfer across interfaces. Nonetheless, inconsistent termination control across synthesis methods has led to contradictory reports on whether certain terminations, particularly –F or –Cl, promote or inhibit specific catalytic pathways. Addressing this issue will require more standardized termination characterization and better correlation between surface chemistry and catalytic metrics.

2D architecture, interlayer engineering and processability. MXenes possess a 2D morphology with high surface-to-volume ratio and extended lateral dimensions.[47,60,87] This structure exposes a large fraction of basal plane and edge sites to reactants and ensures efficient charge percolation through interconnected sheets.[101] The interlayer galleries can host a wide range of intercalated ions and molecules, which expand the spacing, introduce electrostatic or dipolar fields and create additional active sites within the stacked structure.[65,67] To prevent restacking and to maintain accessible transport channels, MXenes can be assembled into hierarchical architectures such as aerogels, foams and patterned films, often with inorganic or polymeric pillars.[102–105] Their hydrophilicity and colloidal stability enable scalable processing into films, membranes and coatings by filtration, spin coating, printing or spraying, which is important for realistic catalytic modules. However, interlayer water and spontaneous restacking significantly affect electron transport and catalytic accessibility, and the sensitivity of MXene colloids to humidity and oxidation has raised concerns about their long-term stability in aqueous catalytic environments.

Optical response, photocarrier management and photothermal effects. Many MXenes and their derivatives display strong optical absorption across a broad spectral range together with ultrafast carrier dynamics.[106] These features can be exploited in photocatalysis and photoelectrocatalysis. MXenes can act as efficient electron or hole collectors when coupled with semiconductors or quantum dots, which promotes charge separation and reduces recombination. In addition, MXenes often exhibit pronounced plasmonic and photothermal responses.[107,108] Localised surface plasmon resonances and nonradiative decay generate enhanced electromagnetic fields and local heating, which can accelerate reaction kinetics and enable synergistic photothermal–photocatalytic processes. Nevertheless, reported photothermal contributions vary widely across studies, with some attributing rate enhancements to plasmonic effects and others to conventional thermal heating, highlighting the need for more rigorous control experiments and quantitative heat measurements.

Structural robustness and durability. MXenes are built from strongly bonded M–X layers, which provide high mechanical strength and thermal stability in the absence of air and confer resilience against collapse under repeated catalytic cycling or electrochemical operation.[58,109,110] Many compositions retain layered morphology and conductivity over a wide pH range. At the same time, surface oxidation, particularly in humid or strongly oxidising environments, can lead to the formation of insulating oxides that passivate active sites and degrade conductivity. Stabilisation strategies, including termination control, heterostructure integration, protective coatings and controlled storage, are therefore critical for long-term operation. However, MXene oxidation remains a major bottleneck for industrial catalysis, as many catalytic processes require prolonged exposure to water, high temperatures or oxidative intermediates. Current stabilisation strategies have improved, but long-term durability under industrially relevant conditions remains insufficiently demonstrated.

Taken together, electronic and compositional tunability, adaptive surface chemistry, 2D architecture, rich optical and photothermal responses and intrinsic robustness define a multidimensional design space for MXene-based catalysts.[111–115] These properties act in concert rather than in isolation, and careful control of synthesis-derived structure–property relationships is essential for the rational design of MXene surfaces and heterostructure interfaces for efficient heterogeneous catalysis. Equally important is the recognition that variability in synthesis and instability under ambient or aqueous conditions continue to create inconsistencies across catalytic studies. These caveats should be kept in mind when interpreting mechanistic trends and benchmarking MXene-based catalysts.

2.2. Challenges of MXenes for catalysis

Despite these attractive features, MXene catalysts face three key intrinsic challenges. First, their surfaces are prone to oxidation under ambient or aqueous conditions, generating insulating oxides that passivate active sites and reduce conductivity; the extent and kinetics of this process vary widely with synthesis, storage, and measurement protocols, leading to inconsistent stability assessments. Second, MXene nanosheets tend to restack and aggregate *via* van der Waals interactions, which decreases accessible surface area, blocks interlayer channels and restricts charge and mass transport, and performance gains are often not simply proportional to the apparent degree of exfoliation. Third, the density of intrinsic active sites is relatively low because basal planes are largely inert and only edge or defect sites contribute significantly, complicating the mechanistic attribution of activity between the MXene framework, *in situ* formed oxides/hydroxides, and possible metal impurities. Together, these factors limit specific production rates, compromise selectivity and reduce operational stability, particularly under harsh electrochemical or photochemical conditions.

Overcoming these limitations requires deliberate surface and interface engineering. Termination tuning, controlled defect generation and selective functionalization can increase active-site density, optimize adsorption energetics and suppress oxidation, while intercalation or spacer insertion mitigates restacking and preserves open ion/electron pathways. In parallel, constructing MXene-based heterostructures with metals, oxides, sulfides, carbons or polymers creates interfacial synergies that accelerate charge transfer, stabilize reactive intermediates and enhance robustness, reflecting the fact that MXene catalysts typically operate as components of complex, dynamically evolving interfaces rather than as isolated materials.

Recognizing these oxidation-, aggregation- and activity-density challenges highlights the importance of rational surface and heterostructure engineering as the foundation of MXene-based catalysis. Accordingly, the following sections focus on how advanced surface modification and interface construction strategies reshape catalytic mechanisms and guide the design of next-generation MXene catalysts.

3. Surface engineering of MXenes

MXenes, as a unique family of 2D transition-metal carbides and nitrides, possess intrinsically attractive features such as high electrical conductivity, compositional diversity, and chemically active surfaces. Nevertheless, their pristine forms often exhibit limitations in stability, surface uniformity, and structural integrity, which restrict their broader functional implementation. To unlock their full potential, it is essential to move

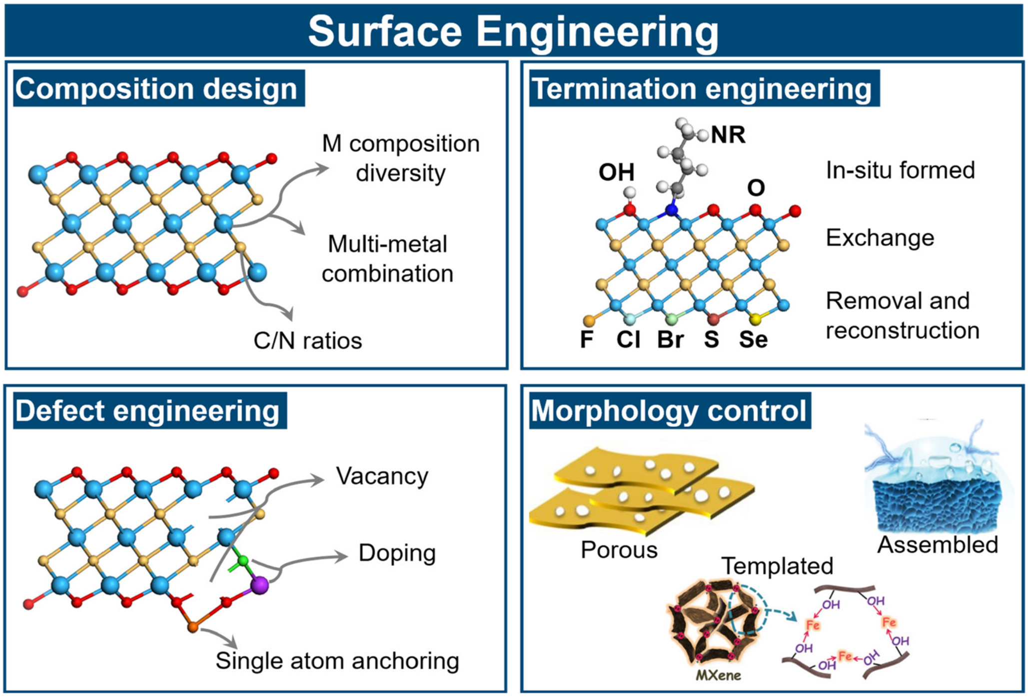

Fig. 4 Classification of surface engineering strategies for MXenes. Reproduced from ref. 116–118 with permission from Wiley, copyright 2016 and 2019.

beyond the as-synthesized state and deliberately manipulate their atomic-scale surface characteristics.

Surface engineering has therefore emerged as a central strategy for tailoring the fundamental properties of MXenes. Unlike direct catalytic studies that emphasize reaction mechanisms, surface engineering focuses on intrinsic material optimization at the atomic and nanoscale, elucidating how composition, surface groups, defects, and morphology can be systematically tuned during synthesis or by post-synthetic treatments to regulate the physicochemical behavior of MXenes. Such approaches provide the foundation for controlling their electrical, chemical, and structural characteristics, which in turn determine their suitability for advanced functional applications.

In this context, surface engineering can be broadly classified into four main directions (Fig. 4): (i) surface-composition design, involving regulation of transition-metal elements, multimetallic high-entropy MXenes, and in-plane-ordered (i-MXenes); (ii) surface-termination engineering, focusing on the deliberate modulation of functional groups such as –O, –OH, –F, –Cl, or –Br; (iii) defect and doping regulation, including creation of vacancies, introduction of heteroatoms, or anchoring of single atoms; and (iv) morphology control, encompassing porous structuring, vertical alignment, or curled architectures to increase accessible surface areas and optimize transport properties. By systematically integrating these atomic-level strategies, this chapter clarifies how the intrinsic surface and structural properties of MXenes can be rationally engineered and thereby establishes the foundation for subsequent discussions on heterostructure-interface design and catalytic implementation.

3.1. Surface composition design

The intrinsic properties of MXenes are strongly dictated by their elemental composition. The layered $M_{n+1}X_n$ framework offers remarkable chemical flexibility, as different transition-metal elements (M) and light elements (X = C or N) can be combined to construct tailored crystalline backbones. Beyond the primary M–X slabs, compositional design extends to multimetallic systems, such as high-entropy MXenes, and ordered double-metal architectures, such as in-plane ordered i-MXenes. Through such regulation, the distribution of electronic states, structural symmetry, interlayer interactions, and overall stability can be precisely modulated at the atomic scale. Compositional engineering thus serves as a foundational dimension of MXene surface design. By varying the type and combination of transition metals, one can tune the density of states (DOS) near the Fermi level, work function, and bonding characteristics, and thereby exert systematic control over charge transport, local electronic structure, and framework stability. Similarly, incorporating multiple metals in a random manner within the M-layers introduces heterogeneity in orbital occupation and lattice strain, while ordered arrangements of different metal cations expand the range of accessible electronic and structural configurations. These strategies not only enrich the family of available MXenes but also establish direct pathways to regulate their intrinsic physical and chemical behaviors. Within this framework, three principal sub-strategies have emerged, namely transition-metal regulation, the design of multimetallic (including high-entropy and ordered) MXenes, and the regulation of the C/N ratio in MXenes. The following subsections examine these approaches in detail and highlight how compositional design provides a versatile tool for tailoring the fundamental characteristics of MXenes.

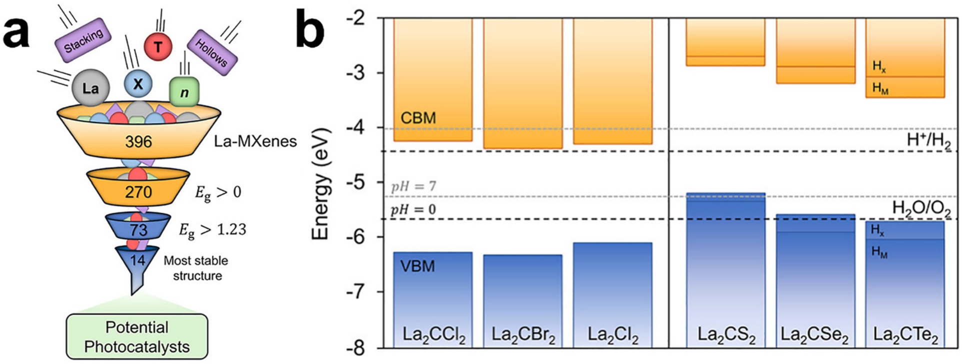

Fig. 5 (a) Schematic representation of the screening using the best obtained ML model. Out of an initial set of 396 La-MXenes, 14 emerged as promising photocatalysts (b) Band alignment diagrams relative to the H_2/H^+ and H_2O/O_2 redox potential energy levels (dotted lines), for the six cases with correct band alignment identified through the screening. The blue and orange bars indicate the VB and CB, respectively. For the Janus chalcogen-terminated MXenes, the band edge position is represented for each surface (H_M or H_X). Reproduced from ref. 120 with permission from American Chemical Society, copyright 2025.

3.1.1. Transition metal element selection. A fundamental strategy in MXene surface composition design is the intentional regulation of transition-metal (M) sites within the $M_{n+1}X_n$ framework. By substituting or incorporating different transition metals, the distribution of d-orbital energies, DOS near the Fermi level, and surface charge density can be finely tuned. These changes not only govern intrinsic conductivity and work function but also influence termination affinity, interlayer spacing, adsorption energies, and overall structural stability. Compared with the intrinsic compositional diversity introduced earlier in Section 2.2, transition-metal regulation is considered here as a deliberate atomic-scale design lever that directly dictates the physicochemical properties of MXenes.

Density functional theory (DFT) studies have revealed systematic variations in MXene characteristics across different transition metal families. Ontiveros *et al.* reported that Group III–IV MXenes (M = Sc, Y, Ti, Zr, Hf) typically exhibit wider band gaps ($\approx$ 1.8–3.1 eV), while Group V–VI MXenes display narrower gaps and higher conductivity, reflecting differences in orbital hybridization and electron delocalization.[119] Such compositional control enables continuous modulation between metallic and semiconducting behavior and exerts a strong influence on photocatalytic and optoelectronic properties. Building on these insights, Ontiveros *et al.* employed hybrid DFT calculations on 4356 MXene structures to train multiple machine-learning (ML) models (Fig. 5).[120] The resulting classification–regression framework achieved 92% accuracy for distinguishing metallic *vs.* semiconducting MXenes and predicted band gaps with a mean absolute error of 0.17 eV. Integrated into the MXgap toolkit, the model enables rapid screening; for example, evaluation of 396 unexplored La-based MXenes identified six candidates with suitable band-edge positions for photocatalytic water splitting and strong visible-light absorption. Feature-importance analysis revealed that structural descriptors dominate band-gap predictions, while incorporating PBE-level DOS further improved accuracy. These results highlight the value of data-driven compositional screening for discovering MXenes with targeted properties, although experimental validation remains essential. Experimentally, Zeraati *et al.* demonstrated that $Ti_3C_2T_x$, prepared under optimized etching conditions, exhibited an ultrahigh conductivity of ~24 000 S cm^{-1}, illustrating how M-site selection directly influences electron-transport properties.[121] Ti-based MXenes are also known to have a broad tunable work-function range (~1.6–5.8 eV),[122] enabling flexible energy-level alignment, whereas Mo-based MXenes exhibit greater structural stability and generally lower termination density due to weaker Mo–termination interactions.[123]

The connection between electronic structure and surface reactivity is commonly described by d-band centre theory. The position of the d-band centre governs the adsorption free energy (ΔG_{ads}) of key intermediates such as *H, *O, and *OH. Computational screening by Seh *et al.* across a series of M_2XT_x MXenes (M = Sc, Ti, Zr, Hf, V, Nb, Ta, Cr, Mo, W; X = C, N; T = –H, –O, –OH, $-H_2O$) revealed systematic shifts in ΔG_{ads}, highlighting how transition metal choice alters adsorption energetics (Fig. 6).[124] Several carbides (*e.g.*, Sc_2C, Mo_2C) and nitrides (*e.g.*, V_2N, Hf_2N, Nb_2N) exhibited values close to thermoneutral adsorption, illustrating the capacity of transition metal regulation to tune intermediate binding strength at the atomic scale. Experimentally, Mo_2CT_x has been reported to display markedly different adsorption characteristics compared with Ti_2CT_x, further emphasizing the role of M-element choice in dictating surface affinity and electronic redistribution.

In addition to electronic effects, the atomic radius and electronegativity of the transition metal also play crucial roles in determining interlayer spacing, termination bonding, and resistance to external stress. Heavier transition metals with larger radii can expand interlayer galleries, mitigating restacking tendencies, while more electronegative metals may strengthen termination bonding and improve tolerance under high-temperature or strongly acidic/alkaline conditions. These variations highlight how the intrinsic chemistry of the M-site governs both the microstructural robustness and the dynamic surface chemistry of MXenes.

Overall, transition metal element regulation provides a powerful tool for engineering MXene properties at the atomic

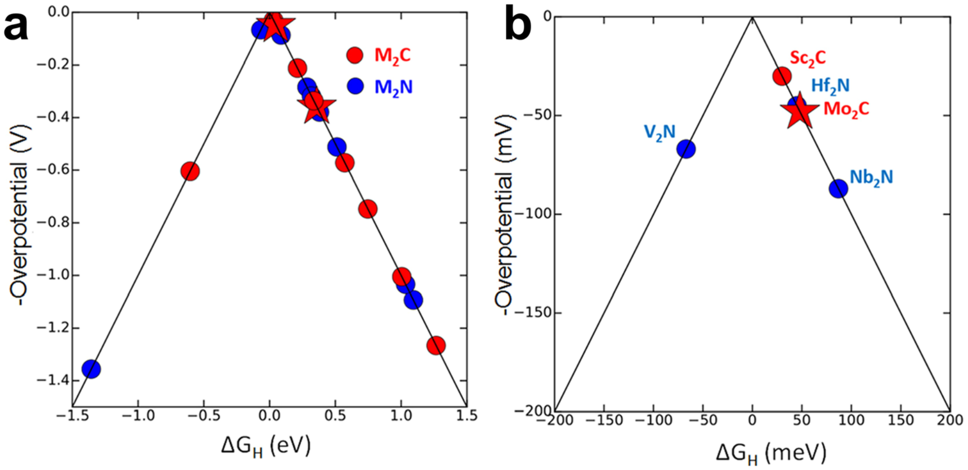

Fig. 6 (a) HER volcano plot with the theoretical overpotentials for the investigated MXenes. Red (blue) circles represent MXenes that are carbides (nitrides). The two MXenes that are investigated in the experiment (Ti_2C and Mo_2C) are indicated by stars. (b) The zoomed-in portion of the top of the volcano. Reproduced from ref. 124 with permission from American Chemical Society, copyright 2016.

scale. Through appropriate selection of M-site elements, one can precisely modulate orbital energetics, DOS distribution, work function, and termination affinity while considering stability under demanding conditions. However, reported trends are sometimes inconsistent across studies because variations in termination composition, defect density, and precursor quality can mask intrinsic M-site effects. More rigorously controlled synthesis protocols and *operando* characterization of both bulk and surface states will therefore be required to establish reliable and transferable composition–property correlations.

3.1.2. Multimetallic MXene design. Incorporating multiple transition metals into the M-layers of MXenes is a versatile strategy to expand compositional diversity and further tune physicochemical properties at the atomic scale. Unlike single-metal MXenes, which rely on the intrinsic chemistry of a single transition metal, multimetallic MXenes introduce additional degrees of freedom through configurational element distribution and compositional heterogeneity. Such systems can adopt several structural motifs, including solid-solution alloys, intermediate-entropy MXenes (m-MXenes), high-entropy MXenes (h-MXenes), and ordered MXenes with in-plane or out-of-plane atomic distributions. Each configuration offers unique opportunities for modulating electronic structure, surface activity, and structural stability.

A defining feature of multimetallic MXenes is their ability to redistribute electronic states across different transition metal sites. The d-orbital contributions of each constituent element interact, altering the DOS near the Fermi level and thereby modifying conductivity, charge localization, and orbital hybridization. For example, Guan *et al.* demonstrated that incorporating Nb into TiC MXene reduces and splits its energy levels, thereby enhancing electronic conductivity and electron transport.[125] Concurrently, electron redistribution shifts the Ti d-band centre closer to the Fermi level, strengthening its chemical affinity and adsorption toward oxygen-containing functional groups. This tailored surface chemistry lowers the ion diffusion barrier, accelerates reaction kinetics, and improves chemical stability. Han *et al.* investigated three binary solid-solution MXene systems based on Ti, Nb, and V: $Ti_{2-y}Nb_yCT_x$, $Ti_{2-y}V_yCT_x$, and $V_{2-y}Nb_yCT_x$ (Fig. 7a).[126] Starting from MAX-phase precursors, elemental substitution at the M-site yielded continuous solid solutions, which were subsequently converted to MXenes. Experiments confirmed infinite mutual solubility at the M-site, with metal atoms randomly distributed across the sublattice. Combined theoretical and experimental analyses demonstrated that the M-site metal type strongly governs MXene electronic structure, optical response, and electrical conductivity. Tuning the M-site composition enabled nonlinear control of absorption peak positions from the ultraviolet to the near-infrared. DFT predicted that the electrical conductivity of $Ti_{2-y}Nb_yCT_x$ and $Ti_{2-y}V_yCT_x$ would increase with greater Nb or V content (Fig. 7b). In contrast, four-point probe measurements revealed an opposite trend: conductivity in certain systems decreased as Nb concentration rose, and Ti-rich samples (lower y value in the formulae) exhibited higher conductivity (Fig. 7c). This mismatch between theory and experiment is likely attributable to differences in the proportion of surface functional groups (O, F), which showed no clear correlation with bulk composition. This case illustrates that, in multimetallic MXenes, surface termination chemistry and defect populations can override idealized bulk electronic trends and must be explicitly considered when interpreting composition–property relationships.

High-entropy MXenes represent a distinctive subclass within this family.[127] By incorporating four or more transition metals in near-equimolar ratios, the system achieves high configurational entropy that thermodynamically stabilizes single-phase structures, which would otherwise tend to segregate. A representative case is the work of Nemani *et al.*, who synthesized two high-entropy MAX phases, $TiVNbMoAlC_3$ and $TiVCrMoAlC_3$, *via* conventional pressureless reaction sintering (Fig. 8).[128]

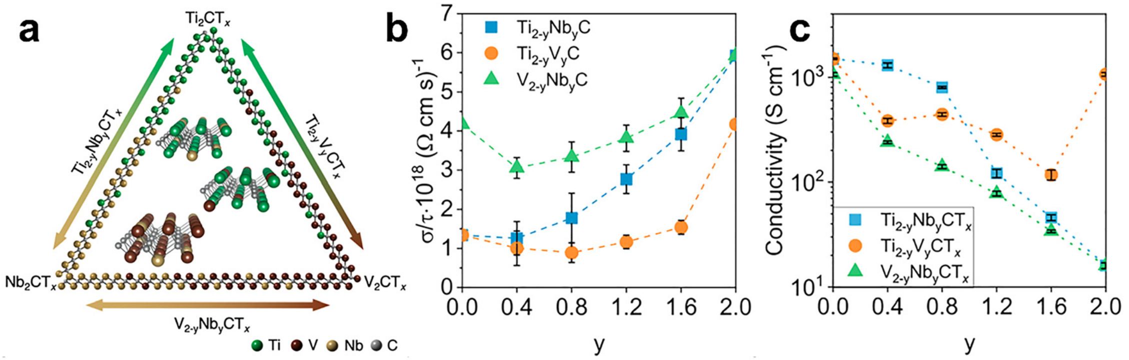

Fig. 7 (a) The compositional triangle of $Ti_{2-y}Nb_yCT_x$, $Ti_{2-y}V_yCT_x$, and $V_{2-y}Nb_yCT_x$ showing the continuous solid solutions of M_2C-type MXenes. (b) The calculated electrical conductivity of bare $M'_{2-y}M''_yC$ MXenes, showing the conductivity change with varying solid solutions. (c) The electrical conductivity of $Ti_{2-y}Nb_yCT_x$, $Ti_{2-y}V_yCT_x$, and $V_{2-y}Nb_yCT_x$ MXenes measured by four-probe method at room temperature showing the conductivity change with varied composition. Reproduced from ref. 126 with permission from American Chemical Society, copyright 2020.

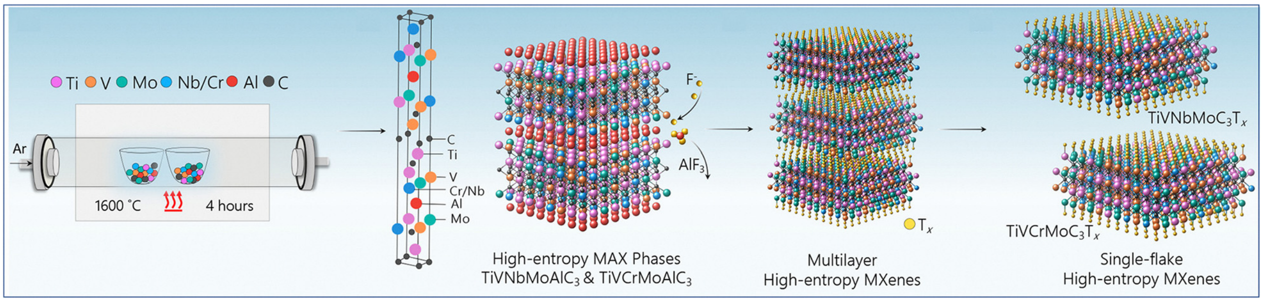

Fig. 8 Schematic for the synthesis of high-entropy MAX and MXenes. Reproduced from ref. 128 with permission from American Chemical Society, copyright 2021.

These were subsequently transformed into high-entropy MXenes, $TiVNbMoC_3T_x$ and $TiVCrMoC_3T_x$, containing equimolar ratios of the primary transition metals (Ti : V : Nb : Mo and Ti : V : Cr : Mo, respectively), through hydrofluoric-acid-based selective etching followed by tetramethylammonium hydroxide delamination. This entropy-driven stabilization expands the range of accessible MXene compositions beyond conventional binary or ternary systems. Moreover, the coexistence of multiple metal sites results in an enriched landscape of orbital contributions, yielding highly adjustable electronic structures and a broad distribution of potential surface terminations. Such complexity creates a spectrum of accessible binding environments and enhances the robustness of the lattice against external perturbations. The presence of multiple metal centers also lays the groundwork for multifunctional surface properties, where different elements provide complementary contributions, for example by tuning electronic density in distinct ways or modulating different types of adsorbate interactions, though the specific property-level consequences of such synergies will be addressed in later sections.

Another important configuration is ordered multimetallic MXenes, where the spatial arrangement of two transition metals is highly controlled rather than randomly distributed.[129–131] In-plane ordered MXenes (i-MXenes), such as $(Mo_{2/3}Sc_{1/3})_2$-Al-derived MXenes ($Mo_{4/3}Sc_{2/3}CT_x$), exhibit periodic atomic alternation of different metals within the same M-layer.[132] This precise distribution imparts highly regular band structures and well-defined site-specific charge densities, providing sharper control over electronic properties compared to random solid solutions. Out-of-plane ordered MXenes (o-MXenes), such as $Mo_2TiC_2T_x$ and $Mo_2Ti_2C_3T_x$, display vertical ordering, where different metals occupy inner *versus* outer M-layers. Anasori *et al.* used density functional theory (DFT) calculations to predict the existence of two new families of two-dimensional MXenes (Fig. 9a).[129] Using Mo_2TiC_2 as an example, they found that the fully ordered Mo_2TiC_2 configuration (Fig. 9b, leftmost inset) exhibits the lowest energy, corresponding to a Mo–Ti–Mo stacking sequence. In contrast, partially ordered configurations (Fig. 9b, centre and right insets) are energetically less favourable. Moreover, the total energy of Mo_2TiC_2 increases almost linearly with the proportion of Mo atoms occupying the middle layer. Additional DFT analyses revealed two general stability trends for ordered MXenes: (1) transition metals that do not crystallize in the rock-salt structure of binary carbides (*e.g.*, Mo, Cr) tend to avoid the central layer, whereas (2) elements such as Nb and Ta prefer the middle layer. These computational predictions were experimentally validated by the successful synthesis of $Mo_2TiC_2T_x$, $Mo_2Ti_2C_3T_x$, and $Cr_2TiC_xT_x$. In particular, the electrochemical performance of $Mo_2TiC_2T_x$ was shown to be dominated by the properties of its surface

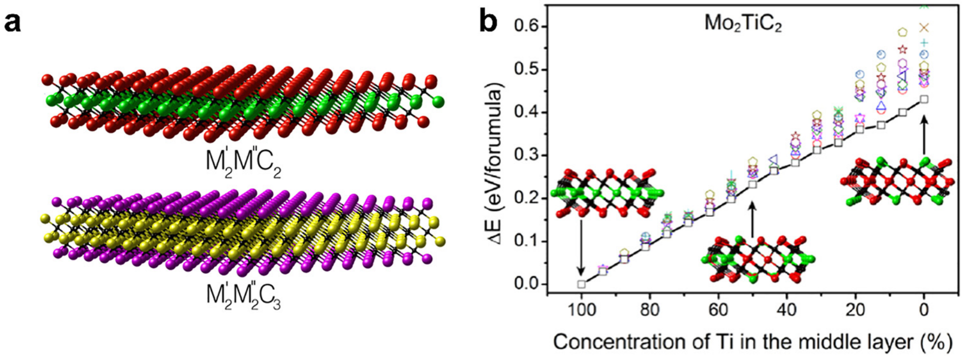

Fig. 9 (a) Structures of double transition metal MXenes, with two structures as $M'_2M''C_2$ and $M'_2M''_2C_3$. (b) Total energy diagram of Mo_2TiC_2 monolayer as a function of Ti concentration in the middle layer, relative to fully ordered Mo_2TiC_2. Reproduced from ref. 129 with permission from American Chemical Society, copyright 2015.

Mo layer. This layered distribution can generate distinct inner and outer surface terminations, modify interfacial dipoles, and influence interlayer coupling. Ordered MXenes therefore provide a structural platform to program surface states and electronic anisotropy with high fidelity, enhancing stability and enabling reproducibility in property control.

Overall, the design of multimetallic MXenes, whether through random solid solutions, high-entropy stabilization, or ordered architectures, provides a powerful route for atomic-scale engineering of surface and electronic properties. By judiciously choosing and arranging multiple transition metals, one can create diverse electronic states, surface terminations, and interlayer characteristics. At the same time, achieving true atomic-scale homogeneity in multimetallic systems remains challenging, and partial disorder or phase segregation can obscure intrinsic trends and lead to misleading structure–property correlations. Improved synthetic control, together with quantitative structural mapping across multiple length scales, will therefore be essential for translating multimetallic design into reproducible functional outcomes.

3.1.3. Regulation of the C/N ratio.

In MXenes, the X-site is typically occupied by carbon (C), nitrogen (N), or their combinations, forming carbides, nitrides, or carbonitride solid solutions such as Ti_3CNT_x.[133,134] The relative fraction of C and N in the lattice profoundly influences the chemical bonding, lattice parameters, and electronic configuration of MXenes, thereby providing a powerful strategy for tailoring their intrinsic physicochemical properties.[135]

The substitution of C by N modifies the electronic environment of the M–X framework due to the distinct atomic characteristics of these two elements. Nitrogen possesses a slightly smaller atomic radius (0.75 Å for N *vs.* 0.77 Å for C) and higher electronegativity ($\chi_N = 3.04$ *vs.* $\chi_C = 2.55$), leading to shorter and stronger M–N bonds compared to M–C bonds.[136] This substitution not only reduces lattice constants and alters interlayer spacing but also increases the ionic character of the M–X bonding network. Such changes modify local charge distribution, orbital hybridization, and vibrational properties, which collectively reshape the structural stability and electronic response of MXenes under different operating environments.

Computational investigations provide critical insight into these effects. Enyashin *et al.*, using density functional tight binding (DFTB) calculations, demonstrated that Ti–N bonding interactions are particularly strong, with $Ti_3CN(OH)_2$—where C and N atoms are randomly distributed—identified as the most stable hydroxylated carbon–nitrogen MXene configuration.[137] This finding underscores that the coexistence of C and N in the lattice can enhance thermodynamic stability by balancing covalent and ionic contributions to bonding.

The modification of electronic properties through C/N regulation has been confirmed by both theory and experiment. Replacing carbon with nitrogen generally increases electron density in the M–X slabs, raises the Fermi level, and strengthens charge delocalization, thereby improving conductivity. For instance, Zhu *et al.* reported that Ti_3CN exhibited markedly higher electronic carrier density compared to Ti_3C_2, directly linked to the stronger electron donation ability of nitrogen relative to carbon.[138] This effect highlights how N incorporation enriches the density of states near the Fermi level, facilitating faster charge transport.

Systematic experimental studies have extended this concept to a wide range of carbonitride MXenes. Zhang *et al.* synthesized sixteen solid-solution MAX precursors with varying C/N ratios and subsequently converted them into MXenes such as $Ti_2(C_{1-y}N_y)T_x$, $Ti_3(C_{1-y}N_y)_2T_x$, and $Ti_4(C_{1-y}N_y)_3T_x$ through molten chloride salt treatment (Fig. 10).[139] Their work demonstrated that the precise adjustment of C/N composition modulates lattice dimensions, modifies electronic band structures, and tunes mechanical rigidity. These systematic variations confirm that controlling the X-site occupancy provides a direct and versatile lever for property engineering at the atomic scale.

Overall, the regulation of the C/N ratio in MXenes offers an effective means of optimizing structural stability, electron mobility, and interlayer dynamics. By tuning the interplay between covalency and ionicity in M–X bonds, carbonitride MXenes bridge carbide-like conductivity with nitride-like robustness. Yet, accurately determining and controlling local C/N distributions remains difficult, and discrepancies between nominal and actual compositions often complicate mechanistic interpretation. Routine integration of high-resolution

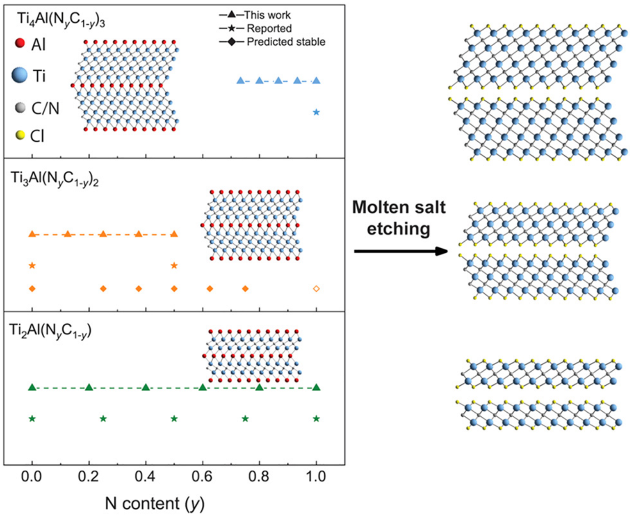

Fig. 10 Illustration of the synthesis of $Ti_2(C_yN_{1-y})$, $Ti_3(C_yN_{1-y})_2$, and $Ti_4(C_yN_{1-y})_3$ titanium carbonitride MXenes (right) from $Ti_2Al(C_yN_{1-y})$, $Ti_3Al(C_yN_{1-y})_2$, and $Ti_4Al(C_yN_{1-y})_3$ titanium aluminum carbonitride MAX phases (left) with tunable X-site stoichiometry, along with feasibility of MAX synthesis for compositions with a varying number of layers and N content. Reproduced from ref. 139 with permission from American Chemical Society, copyright 2023.

structural and compositional analysis, including atomically resolved spectroscopy and microscopy, will therefore be necessary to establish reliable links between C/N tuning and functional performance.

3.1.4. Challenges and perspectives. Compositional engineering, encompassing transition-metal selection, multimetallic design, and C/N ratio adjustment, offers a powerful tool to fine-tune the orbital energetics, electronic density of states, lattice parameters, and bonding characteristics of MXenes. At the same time, many of these compositional strategies face practical constraints that arise during precursor synthesis and multicomponent integration. Accurate control of transition-metal stoichiometry and spatial distribution during precursor synthesis remains nontrivial, particularly for elements with substantial differences in atomic size or oxidation state, which often lead to local phase segregation or uneven bonding environments. In multimetallic and high-entropy MXenes, achieving homogeneous atomic mixing without compromising lattice order or producing undesirable secondary phases requires sophisticated kinetic control and high-resolution compositional mapping. Likewise, the precise determination of the C/N ratio and its local fluctuations within carbonitride systems remains experimentally demanding, complicating efforts to establish direct correlations between atomic composition, electronic structure, and emergent properties.

Moving forward, progress will depend on more deterministic control of precursor chemistry and multiscale compositional analysis, integrated with advanced synthesis routes such as molten-salt growth, atomic-layer-controlled processing, and post-synthetic substitution, so that targeted electronic landscapes can be obtained in a reproducible manner.

3.2 Surface termination engineering

Surface termination engineering represents one of the most effective approaches for tailoring the surface chemistry and electronic structure of MXenes at the atomic level.[140,141] During synthesis, unsaturated transition-metal atoms at the surface readily react with species present in the etching media, forming a variety of terminal groups (T_x) such as –O, –OH, –F, –Cl, or –Br.[142] These terminations strongly influence local charge distribution, surface dipoles, and work function, thereby governing the physicochemical behavior of MXenes.[143,144] Owing to their dynamic and environment-dependent nature, surface terminations not only define the interfacial properties but also determine how MXenes interact with external species, and thus constitute a fundamental factor controlling MXene functionality.[145,146]

3.2.1. Origin and electronic influence of terminations. The type and uniformity of terminal groups are closely linked to the synthesis route. Conventional HF or LiF/HCl etching typically yields mixed –F, –OH, and ═O terminations, whereas Lewis acidic molten-salt methods favour halogen terminations (*e.g.*, –Cl, –Br). Each termination introduces distinct local dipoles and modifies the surface potential, thereby tuning both the Fermi level and work function (Φ). For instance, $Ti_3C_2T_x$ can exhibit Φ values ranging from approximately 1.6 to 5.8 eV, depending on termination composition: a higher fraction of –O– terminations increases Φ due to stronger electron withdrawal, whereas –OH groups decrease Φ by inducing opposite dipole moments. DFT calculations further indicate that the nature of the terminations directly modulates the electronic DOS near the Fermi level, affecting band alignment, carrier mobility, and charge redistribution at the surface. Schultz *et al.* investigated the work function of $Ti_3C_2T_x$ as a function of annealing temperature.[94] As shown in Fig. 11a, pristine $Ti_3C_2T_x$ exhibits a relatively low work function of ~3.9 eV, which increases to 4.8 eV after annealing at 380 °C. This rise is attributed to the removal of residual surface contaminants. At higher temperatures, fluorine desorption leads to a subsequent decrease in the work function, which plateaus at ~4.1 eV close to the theoretical prediction for bare Ti_3C_2 (3.9 eV). Comparison of these experimental results with detailed DFT calculations reveals that the observed work function is not simply the average of values for uniformly terminated Ti_3C_2 surfaces (red curve in Fig. 11b). Instead, it depends critically on the interplay between different surface terminations and their associated local dipole moments. To capture this effect, the work function of the smallest supercell matching the surface stoichiometry measured by XPS, with terminations randomly distributed, was calculated. This model produced a value (blue curve in Fig. 11b) that agrees qualitatively with experimental results at elevated annealing temperatures. The remaining discrepancy at low temperatures is likely due to surface contamination, which is not incorporated in the computational model.

Despite these insights, reported work function values and termination compositions often vary significantly across different studies because of differences in etching protocols, surface cleanliness, and environmental exposure. These inconsistencies

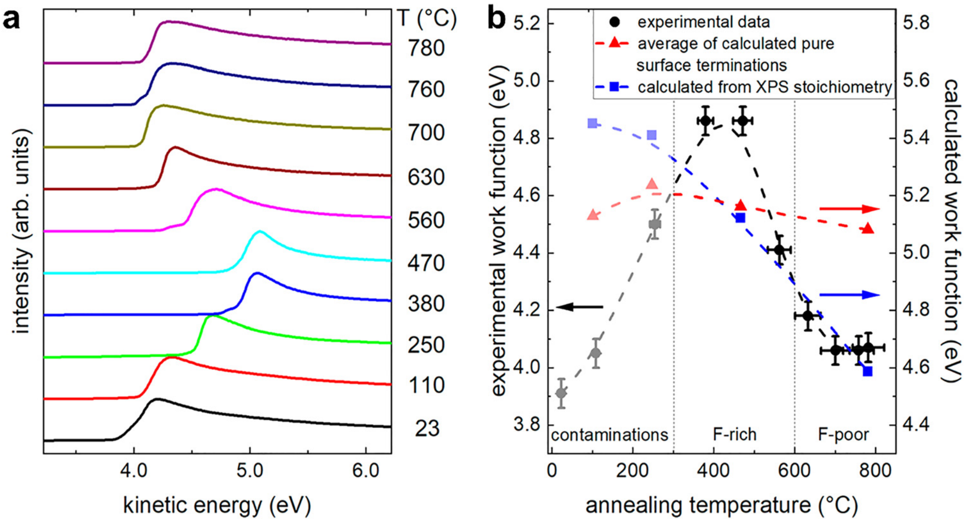

Fig. 11 (a) Secondary electron cutoff (SECO) spectra of $Ti_3C_2T_x$ annealed at different temperatures. (b) Work function values determined from the SECOs in (a) as a function of annealing temperature. Work functions obtained from DFT for different surface terminations, calculated by using the real surface stoichiometry obtained from XPS (blue) and obtained by averaging the work functions of purely terminated $Ti_3C_2O_2$, $Ti_3C_2F_2$, $Ti_3C_2OH_2$, and Ti_3C_2 surfaces, weighted by the experimentally determined stoichiometry (red). Reproduced from ref.[94] with permission from American Chemical Society, copyright 2019.

complicate the establishment of universal structure–property relationships. Addressing this issue will require standardized synthesis–characterization workflows, explicit reporting of environmental history, and *operando* techniques capable of capturing the dynamic evolution of terminations, so that reported trends become genuinely comparable across laboratories.

3.2.2. Synthetic and post-treatment strategies for termination control. The composition of surface terminations can be precisely adjusted through both synthetic control and post-synthesis modification. In solution-based etching, varying the HF concentration or introducing buffering agents can alter the ratio between –F and –O/–OH groups: lower HF concentrations or buffered systems generally favour oxygen-rich surfaces.[147] Subsequent alkaline treatments (*e.g.*, NaOH immersion) promote cation intercalation (Na^+) between layers, which replaces –F terminations with –OH *via* nucleophilic substitution, as confirmed by energy-dispersive X-ray spectroscopy (EDX) and corresponding interlayer expansion.[148]

Beyond aqueous methods, molten-salt etching offers a versatile low-temperature route for tailoring MXene terminations and interlayer spacing. Zhang *et al.* developed a Lewis-basic $AlBr_3$–NaBr–KBr eutectic, in which reduced $AlBr_3$ content (<50 mol%) generates desolvated Br^- and Na^+/K^+ species capable of nucleophilic substitution of –F groups and simultaneous cation intercalation (Fig. 12).[149] This process expands the d-spacing (*e.g.*, $Ti_3C_2T_x$: 11.2 → 14.7 Å) and increases –Br coverage, which is supported by DFT showing $\Delta H < 0$ for Br–F exchange. The strategy is generalizable to $Nb_4C_3T_x$, $Mo_2Ti_2C_3T_x$, and iodide-based systems, enabling halogen substitution and structural modulation within one step. Although powerful, reproducible control remains challenging due to sensitivity to melt composition, hydration, and intermediate states; standardized protocols will therefore be essential.

Similarly, chloride-terminated MXenes can be synthesized using Lewis-acidic molten salts such as $ZnCl_2$, $CuCl_2$, or $FeCl_3$, and further modified through *in situ* substitution reactions in molten halides. Kamysbayev *et al.* established a general molten-salt transformation strategy that enables both installation and elimination of diverse surface groups, producing MXenes terminated with O^{2-}, NH_2^-, S^{2-}, Se^{2-}, Te^{2-}, Cl^-, Br^-, or even bare-metal surfaces (Fig. 13).[150] In this approach, preformed $Ti_3C_2Cl_2$ and $Ti_3C_2Br_2$ MXenes are dispersed in low-melting eutectic halide mixtures such as CsBr–KBr–LiBr, which provide a highly ionic, diffusion-permissive medium for surface-exchange reactions. Reactive chalcogen or pnictogen precursors, such as Li_2S, Li_2Se, Li_2Te, Li_2O, and $NaNH_2$, donate anions that replace labile halide terminations *via* anion-exchange reactions driven by the large difference in formation enthalpies between M–X (X = O, S, Se, Te, NH) and M–Cl/Br bonds. The weaker Ti–Cl and Ti–Br bonds, combined with enhanced ion mobility in molten salts, allow complete substitution within minutes at 300–600 °C, yielding products such as Ti_3C_2S, Ti_3C_2Se, and Ti_3C_2Te with distinct lattice expansions (up to 18% for Te-terminated $Ti_3C_2T_x$). Moreover, reductive elimination reactions using LiH remove surface halides entirely, generating bare MXenes with tunable vacancy concentrations.

These chemical transformations highlight the reactivity hierarchy of surface terminations, from labile halides to strongly bound chalcogenides and oxides, and establish molten-salt substitution as a powerful, broadly applicable route for covalent surface modification. Importantly, Nb_2C MXenes derived through this strategy exhibit termination-dependent superconducting transitions (T_c = 4–7 K), confirming that surface chemistry directly modulates electronic transport and lattice strain in two-dimensional carbides. However, despite these versatile methods, achieving reproducible termination

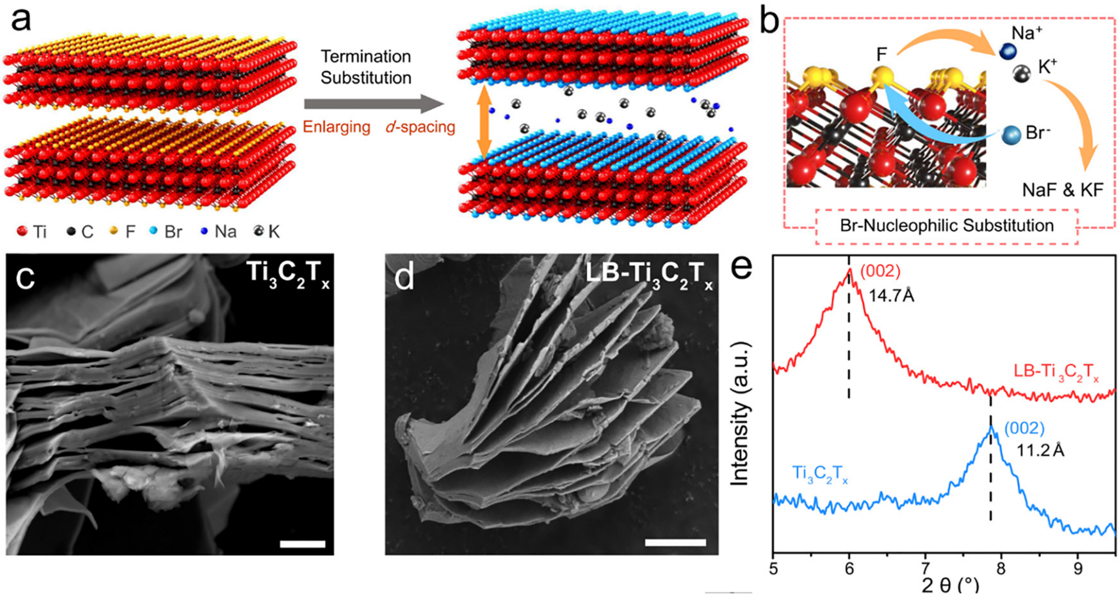

Fig. 12 (a) Schematic of the preparation of LB-$Ti_3C_2T_x$. After Lewis-basic halides treatment, $Ti_3C_2T_x$ is intercalated by desolvated Na and K, inducing the increased interlayer spacing. Simultaneously, the surface –F termination is replaced by desolvated halogen anions. (b) The process of the nucleophilic substitution between desolvated Br and F atoms (red balls: titanium, black balls: carbon, yellow balls: fluorine, cyan balls: bromine, blue balls: sodium, silver ball: potassium). SEM (Scale bar 1 μm) of multilayer $Ti_3C_2T_x$ (c) and LB-$Ti_3C_2T_x$ (d). (e) XRD patterns of multilayer $Ti_3C_2T_x$ and LB-$Ti_3C_2T_x$. Reproduced from ref. 149 with permission from Springer Nature, copyright 2022.

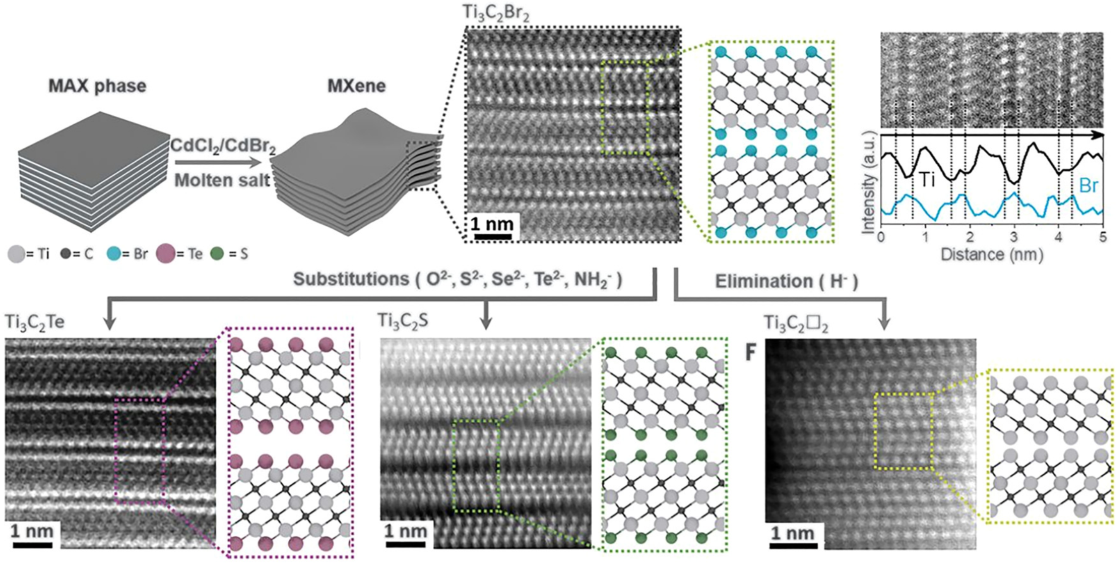

Fig. 13 Surface reactions of MXenes in molten inorganic salts. Reproduced from ref. 150 with permission from AAAS, copyright 2020.

control remains challenging. Small variations in melt composition, precursor hydration or impurity content can lead to substantial differences in termination ratios and interlayer chemistry. Furthermore, many substitution pathways proceed through transient intermediate states that are difficult to monitor, resulting in inconsistent reports of termination stability and exchange completeness. More quantitative kinetic studies, real-time structural characterization and rigorously standardized processing conditions will therefore be required to convert these synthetic concepts into reliably scalable protocols for MXene termination control.

3.2.3. Advanced termination substitution and complex surface modification.

More sophisticated substitution reactions have further broadened the chemical diversity of MXene surfaces, allowing the rational construction of multifunctional hybrid interfaces. Zhou *et al.* demonstrated that halogen-terminated MXenes can undergo nucleophilic substitution with *in situ* deprotonated amines to form covalently anchored amide and imide terminations, producing robust organic–inorganic hybrid MXenes (Fig. 14).[151] In this strategy, halide-terminated $Ti_3C_2T_x$ or Nb_2CT_x was treated with alkali-activated amines

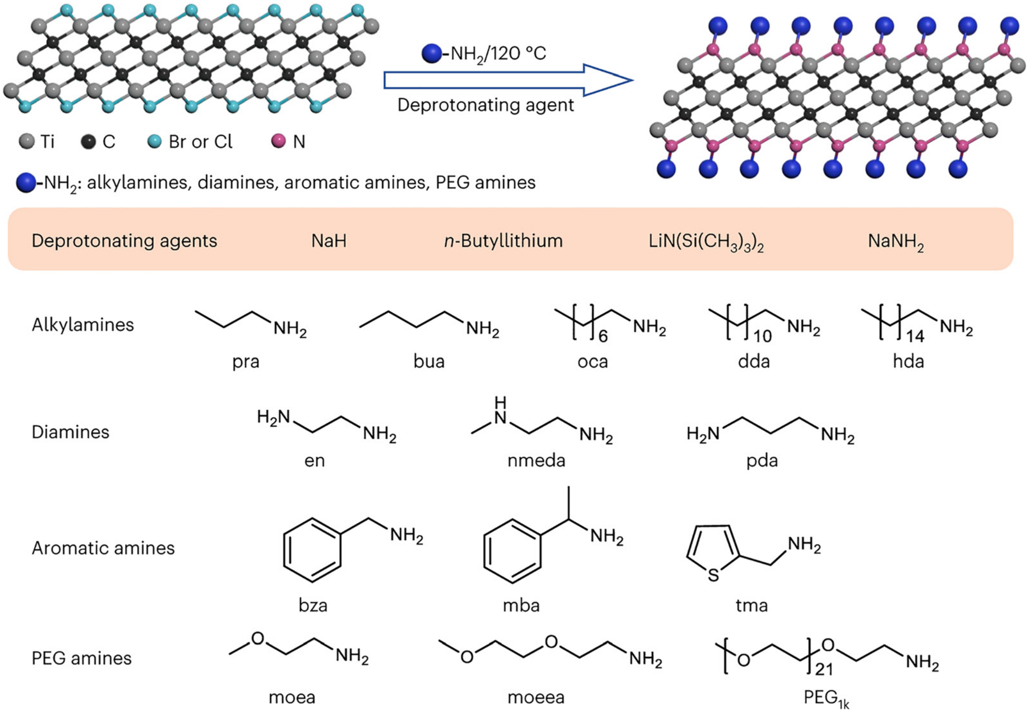

Fig. 14 Schematic of organic–inorganic h-MXene synthesis and examples of the studied deprotonating agents and organic amines. Reproduced from ref. 151 with permission from Springer Nature, copyright 2023.

(RNH^- or R_2N^-, generated by NaH, *n*-butyllithium, $LiN(SiMe_3)_2$, or $NaNH_2$), enabling the replacement of surface halides by amido species. Both aliphatic and aromatic amines, including monoamines, diamines, and PEG-based ligands, could be introduced, forming ordered interfacial layers with chain-length-dependent interlayer expansion. Solid-state ^{15}N NMR and XPS confirmed strong Ti–N coordination and the coexistence of –NHR and =NR species. The resulting molecularly grafted surfaces not only enhance hydrolytic stability but also provide tunable surface dipoles and electronic coupling through the controllable polarity and conjugation of organic groups. Such hybrid terminations thus bridge molecular functionality with metallic conductivity, opening new avenues for surface electronic tailoring, wettability regulation, and chemical selectivity in MXene-based catalysis and sensing.

Li *et al.* further advanced termination control by introducing three-atomic-layer borate polyanions (O–B–O configuration) through a flux-assisted eutectic-melt etching method (Fig. 15).[152] In a $CuCl_2–Na_2B_4O_7$–NaCl–KCl melt, Lewis-acidic $CuCl_2$ selectively removes the A-element from MAX precursors, while borax-derived BO_2^- species uniformly decorate both MXene surfaces, producing highly ordered O–B–O trilayer terminations. Spectroscopic and microscopic analyses (^{11}B NMR, XPS, and HAADF-STEM) revealed symmetric coverage that increases the interlayer spacing and smooths local potential fluctuations. The O–B–O framework effectively suppresses carrier backscattering and trap states, leading to improved electronic mobility and structural uniformity. Conceptually, this flux-assisted approach provides a blueprint for creating other bridging terminations such as O–Si–O, O–V–O, or even O–P–O, which could form lattice-matched, covalently anchored overlayers on MXene basal planes. Such heteroatomic surface architectures hold promise for constructing epitaxial, composition-tunable, and functionally coupled interfaces that unify chemical stability with electronic versatility.

Collectively, these studies exemplify the transition of termination engineering from conventional anion exchange to chemically programmable hybridization, where both organic ligands and inorganic polyanions can be integrated into MXene frameworks. This evolution provides a molecular-level handle to manipulate surface dipoles, electronic structures, and interfacial reactivity, establishing a foundation for next-generation MXenes with adaptive, multifunctional, and electronically coherent interfaces. Despite these advances, significant challenges remain. Achieving uniform coverage without multilayer formation is often difficult, and the compatibility of complex organic or inorganic terminations across different MXene compositions is not yet fully understood. Furthermore, the long-term thermal and chemical stability of such hybrid terminations under catalytic or electrochemical operating conditions has rarely been systematically investigated. Future work should therefore combine controlled kinetic studies, improved synthetic precision, and *operando* characterization techniques capable of resolving the structural evolution of multifunctional surface terminations, in order to clarify which hybrid motifs are truly robust under realistic working conditions.

3.2.4. Termination removal and reconstruction. While surface terminations stabilize MXenes during synthesis, they are

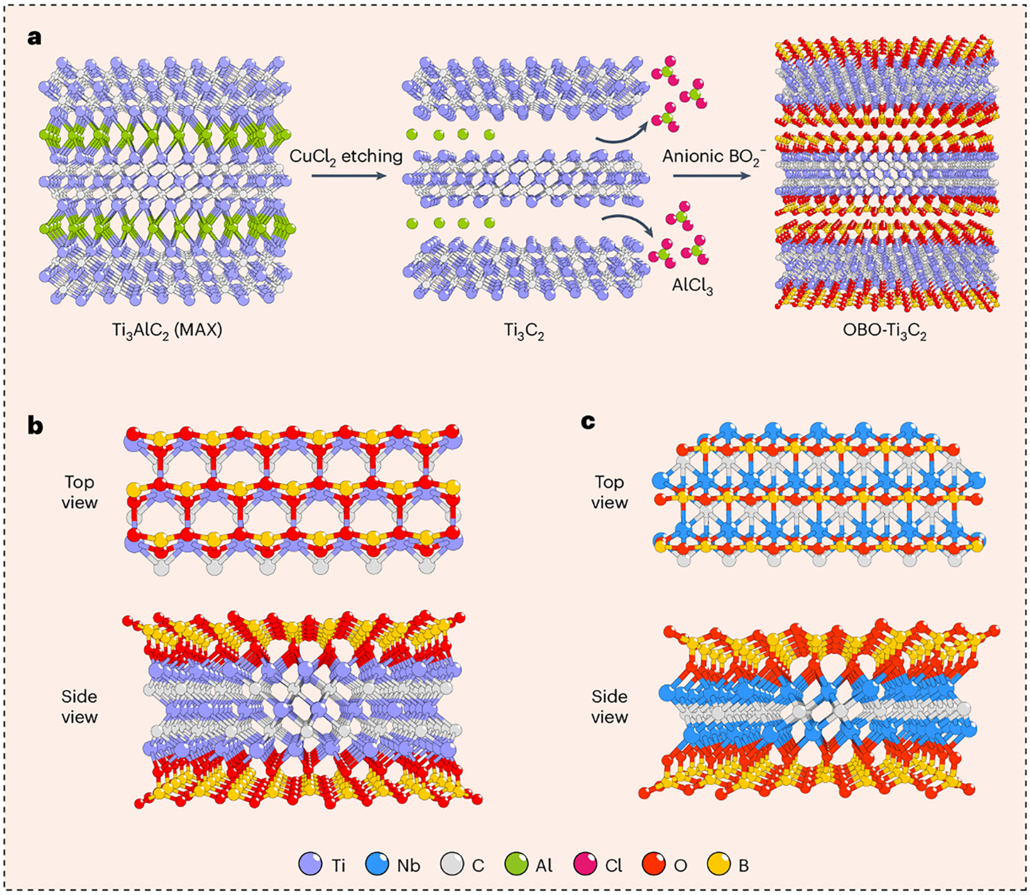

Fig. 15 (a) Schematics showing the synthesis process of OBO-MXenes by the flux-assisted eutectic molten etching approach. Atomic structures of OBO-Ti$_3$C$_2$ (b) and OBO-Nb$_2$C (c). Reproduced from ref. 152 with permission from Springer Nature, copyright 2024.

not strictly required for structural integrity under all conditions. High-temperature hydrogen reduction, plasma treatment, or vacuum annealing can selectively remove or reconstruct terminations, exposing partially bare metallic surfaces.[153–155] DFT studies predict that complete or partial termination-free MXenes exhibit altered band structures and higher surface energies, which can substantially enhance adsorption and activation of small molecules, enabling reactions with very inert molecules like CO_2 or N_2.[156–160] *In situ* transmission electron microscopy (TEM) and spectroscopic investigations by Hart *et al.* revealed that progressive removal of surface terminations leads to a measurable increase in conductivity, confirming a direct correlation between surface reconstruction and electron transport (Fig. 16).[161] These observations underscore the importance of balancing termination stability and reactivity, as carefully controlled, partially termination-free surfaces can create metastable surface states with distinct catalytic functionalities.

Nonetheless, generating stable and spatially uniform partially bare MXene surfaces remains challenging. Termination removal often produces heterogeneous mixtures of exposed metal sites, residual functional groups, and vacancy clusters, complicating mechanistic interpretation. Fully bare surfaces are prone to rapid re-functionalization when exposed to air or solution, and precise control over the extent of reconstruction requires tight regulation of temperature, atmosphere, and plasma dosage. Moreover, the transient intermediates formed during termination desorption are difficult to characterize with conventional *ex situ* techniques. To move beyond qualitative observations, future studies will need *operando* methodologies capable of resolving ultrafast surface restructuring, together with predictive thermodynamic and kinetic models that can guide the controlled generation and stabilization of catalytically relevant termination-free states.

3.2.5. Challenges and perspectives. Although extensive advances have been achieved, quantitative determination and dynamic tracking of MXene terminations remain challenging. Experimental techniques such as XPS, nuclear magnetic resonance (NMR), and neutron pair distribution function analysis often yield inconsistent termination ratios due to spectral overlap among elements and environmental sensitivity. Moreover, terminations can undergo continuous rearrangement or exchange during operation, complicating the establishment of structure–property relationships. A key unresolved issue is that catalytically relevant termination states are often transient and differ markedly from those inferred from *ex situ* characterization. Future progress will rely on combined *in situ*/*operando* spectroscopy and modelling to track termination evolution in real time and relate it to changes in electronic structure,

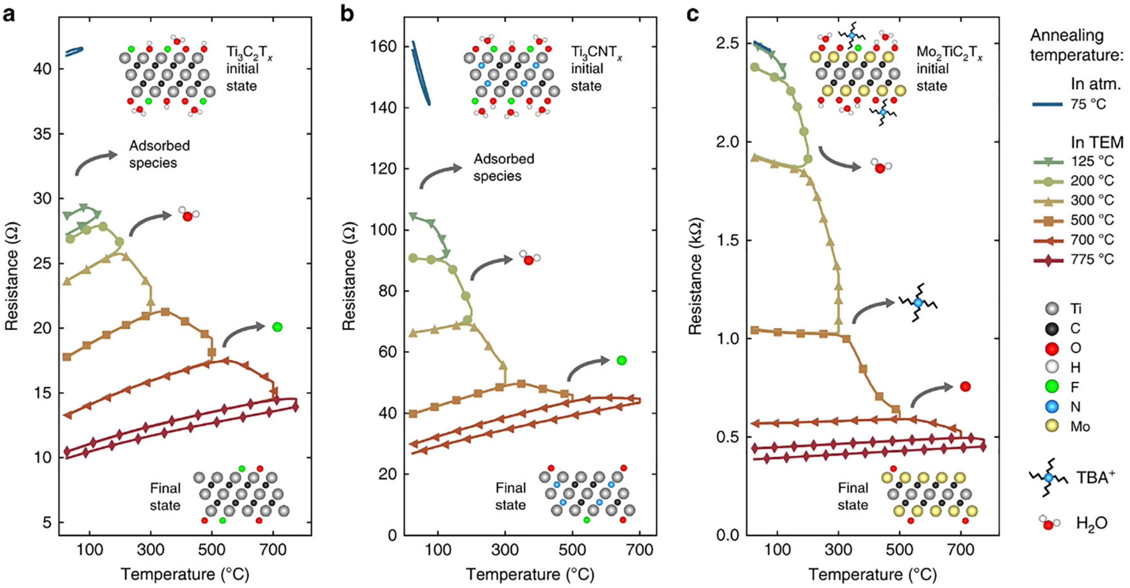

Fig. 16 Evolution of MXene electronic properties upon *in situ* vacuum annealing. Resistance *versus* temperature measurements are shown for $Ti_3C_2T_x$ (a), Ti_3CNT_x (b), and $Mo_2TiC_2T_x$ (c). Reproduced from ref. 161 with permission from Springer Nature, copyright 2019.

thereby clarifying which termination motifs are truly operative under working conditions and how they control interfacial reactivity.

3.3. Surface defect and doping engineering

Defect engineering represents one of the most powerful routes to manipulate the atomic and electronic landscape of MXenes. By intentionally introducing vacancies, heteroatoms, or isolated metal centres, the local coordination environment, charge distribution, and orbital occupancy can be finely tuned, enabling control over conductivity, carrier mobility, and surface reactivity. These atomic-scale perturbations reshape both geometric and electronic structures, offering pathways to modulate physicochemical properties and stability. Broadly, surface-defect and doping engineering encompasses three key aspects: vacancy generation, heteroatom incorporation, and single-atom anchoring.

3.3.1. Vacancy engineering. During the selective etching of MAX precursors, the removal of A-site elements frequently leads to lattice imperfections such as metal vacancies (MVs), carbon/nitrogen vacancies (XVs), and mixed vacancy clusters. Even under relatively mild etching conditions, partial atomic displacement or bond cleavage can occur, producing local distortions that profoundly affect the surface electronic landscape.[96] These defects increase the density of low-coordination sites, modify charge delocalization, and locally shift the Fermi-level position, which are key factors influencing charge transport and reactivity. Sang *et al.* employed aberration-corrected scanning transmission electron microscopy (STEM) combined with DFT to investigate monolayer $Ti_3C_2T_x$ MXene prepared by the MILD method. They identified Ti vacancies and Ti-vacancy clusters within the two outermost Ti layers as predominant defect species (Fig. 17a–c).[162] Concurrently, metal cations generated during etching were observed to adsorb onto the MXene surface, contributing to local charge redistribution. Across different MXene systems (M = Sc, Ti, V, Zr, Nb, Mo, Hf, Ta, W), C/N vacancies show lower formation energies than

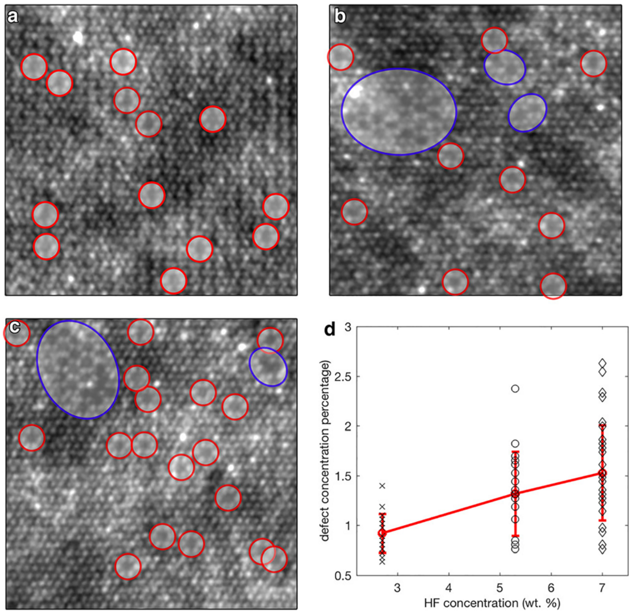

Fig. 17 HAADF-STEM images from single-layer $Ti_3C_2T_x$ MXene flakes prepared using etchants with different HF concentrations: (a) 2.7 wt% HF, (b) 5.3 wt% HF, and (c) 7 wt% HF. Single V_{Ti} vacancies are indicated by red circles, while vacancy clusters $V_{Ti}{}^{C}$ are shown by blue circles. (d) Scatter plot of defect concentration from images acquired from samples produced using different HF concentrations. The red line shows the error plot with the average and standard deviation for different HF concentrations. Reproduced from ref. 162 with permission from American Chemical Society, copyright 2016.

metal vacancies, indicating their preferential formation. Additionally, defect density is highly sensitive to etching parameters; higher HF concentrations or longer etching times lead to increased vacancy populations (Fig. 17d).

Despite these structural imperfections, MXenes generally retain high electrical conductivity owing to the metallic M–X backbone. This coexistence of long-range conductivity with localized defect-induced electronic modulation makes vacancy engineering an efficient route for fine-tuning charge transport and surface activity at the atomic scale. However, vacancy formation remains difficult to regulate precisely because defect populations are highly sensitive to small variations in etching conditions, precursor crystallinity, and post-treatment protocols. Reported vacancy densities differ widely across studies, complicating attempts to establish quantitative correlations between defect type, electronic redistribution, and catalytic function. Moreover, vacancy clustering or partial healing during thermal or chemical treatments is rarely monitored *operando*, further limiting mechanistic interpretation. These limitations highlight the need for standardized etching procedures together with *operando* defect-tracking techniques that can capture the dynamic evolution of vacancies under realistic conditions, and for quantitative models that disentangle vacancy effects from concurrent changes in terminations and interlayer chemistry.

3.3.2. Heteroatom doping. Heteroatom doping through substitutional, interstitial, or surface incorporation offers an effective means to modify MXene electronic structure, chemical stability, and defect chemistry. Introducing dopants such as N, P, or S alters electronegativity, atomic radius, and valence-state distributions within the lattice, thereby reconfiguring local charge density and the overall electronic structure. These substitutions influence the Fermi level, DOS near the Fermi level, and orbital hybridization, providing a powerful tool for tailoring intrinsic physicochemical properties.

Nitrogen doping has been most widely explored owing to its comparable atomic size to carbon and strong affinity toward transition metals. Le *et al.* introduced multiple nitrogen species including Ti–N, N–H, and O–Ti–N into $Ti_3C_2T_x$ MXene through ammonia-assisted thermal treatment (Fig. 18).[163] The coexistence of diverse N configurations induced local electronic redistribution and enhanced carrier delocalization. DFT calculations indicated that optimal nitrogen doping shifts the Fermi level and adjusts the Gibbs free energy of hydrogen adsorption ($\Delta G_{\mathrm{Had}^*}$) toward thermoneutral values, improving charge-transfer efficiency.

Phosphorus doping yields similar electronic effects. Wen *et al.* annealed $Ti_3C_2T_x$ in a sodium hypophosphite atmosphere to obtain phosphorus-doped P-$Ti_3C_2T_x$. XPS and DFT analyses showed that P atoms preferentially occupy Ti-vacancy sites with low formation energy ($\Delta G_{\mathrm{P}^*} = -0.028$ eV Å^{-2}), forming P–C and P–O bonds with surface terminations.[164] The resulting electron redistribution alters the work function and enhances conductivity. Other reports, including Qi *et al.*, indicate that P incorporation can stabilize reaction intermediates and lower activation barriers, directly influencing catalytic activity.[165]

In essence, heteroatom doping allows continuous adjustment of electronic configuration and charge mobility while preserving the structural integrity of the MXene framework. By combining dopant selection with thermal or plasma activation, it is possible to achieve defect–dopant synergy, establishing precise control over lattice distortions and local electronic polarization. Despite these advantages, heteroatom doping often suffers from limited dopant incorporation efficiency, nonuniform spatial distribution, and ambiguity in identifying true substitutional *versus* adsorbed species. These issues frequently lead to inconsistent structure–property trends. Furthermore, dopant migration or oxidation during operation is rarely monitored, making long-term stability difficult to assess. Consequently, future efforts must integrate high-resolution *in situ* spectroscopies with theoretical modelling to resolve dopant location, bonding configuration, and dynamical evolution under reactive environments, and to distinguish genuinely active dopant structures from spectator species or minor phase impurities.

3.3.3. Single-atom anchoring. MXenes, with their large specific surface area, high defect density, and abundant surface terminations, provide ideal templates for immobilizing single

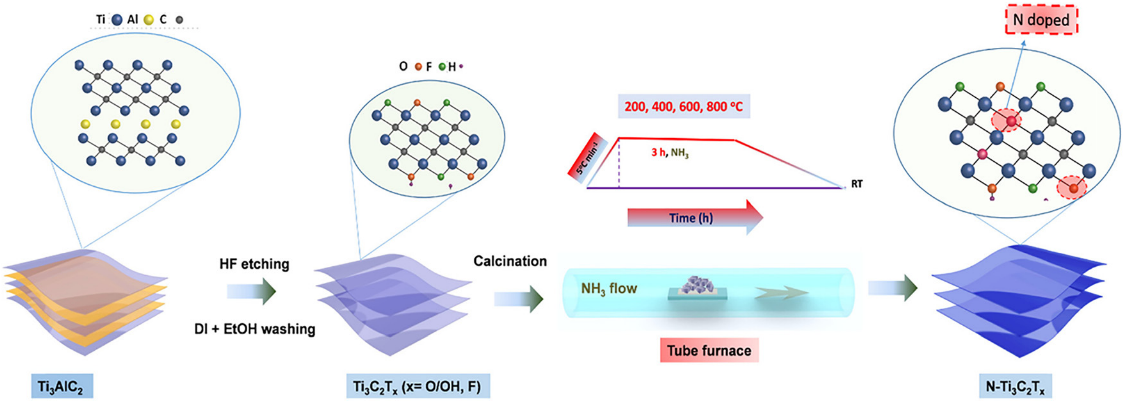

Fig. 18 Illustration of the synthesis of N-doped samples from the Ti_3AlC_2 MAX Phase. Reproduced from ref. 163 with permission from American Chemical Society, copyright 2019.

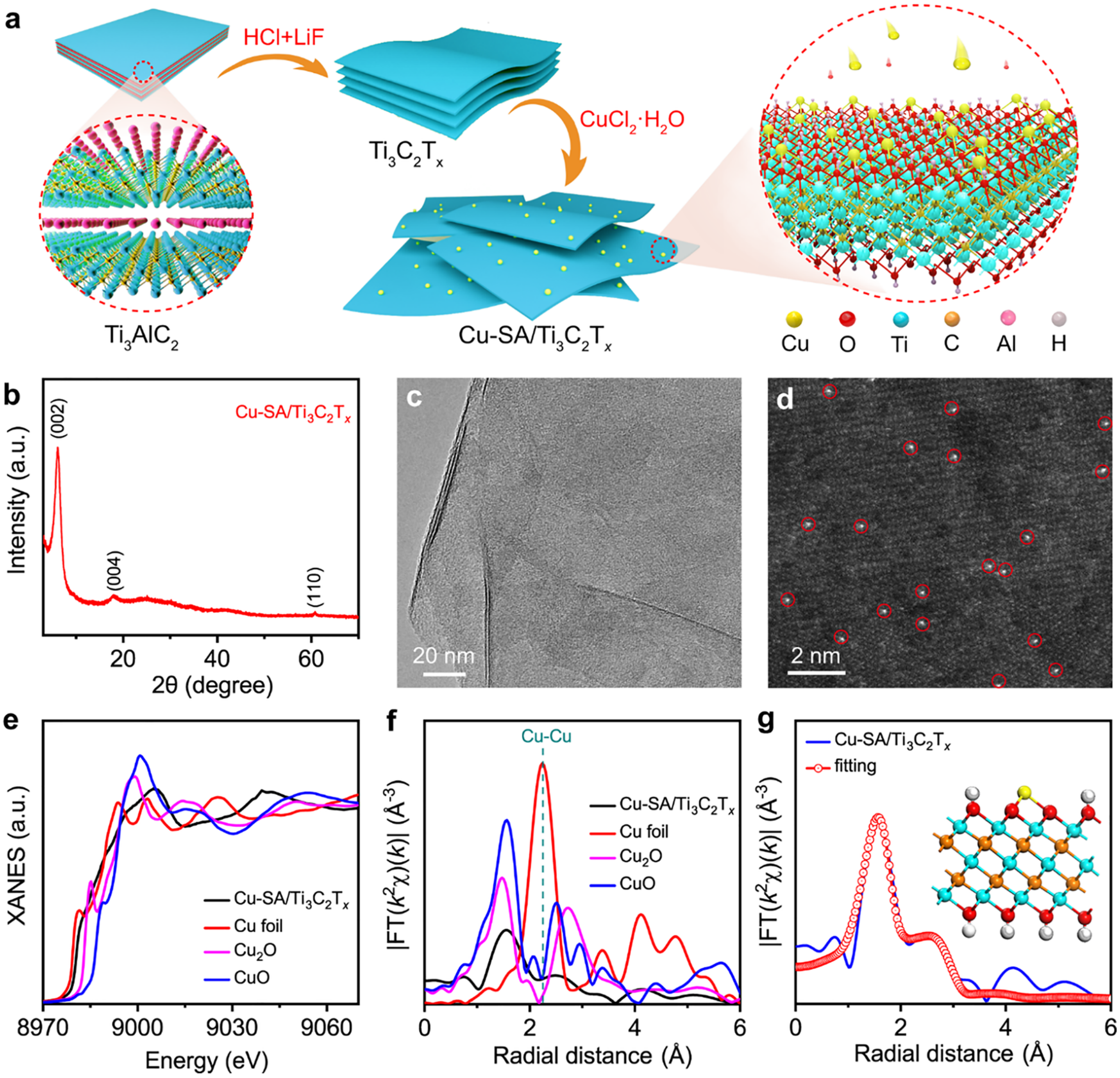

Fig. 19 (a) Schematic illustration of the synthesis procedure. (b) XRD pattern. (c) TEM image. (d) HAADF-STEM image in which some of the Cu SAs are highlighted by red circles. (e) XANES spectra at the Cu K-edge with CuO, Cu_2O and Cu foil as reference. (f) The k^2-weighted Fourier transform (FT) EXAFS curves in which $\chi(k)$ denotes the EXAFS oscillation function. (g) EXAFS fitting curve of $Cu-SA/Ti_3C_2T_x$, insert is an illustration of $Cu-SA/Ti_3C_2T_x$ structure. The yellow, blue, dark yellow, red and white balls represent Cu, Ti, C, O and H, respectively. Reproduced from ref. 167 with permission from Springer Nature, copyright 2021.

atoms. Electronegative surface groups facilitate strong adsorption of metal cations, which can subsequently undergo *in situ* reduction and coordination stabilization.[166] Vacancies generated during etching act as robust anchoring sites, offering localized electron density redistribution and strong metal–support coupling. Bao *et al.* synthesized Cu single-atom-decorated $Ti_3C_2T_x$ ($Cu–SA/Ti_3C_2T_x$) by adsorbing and reducing Cu^{2+} ions on MXene surfaces (Fig. 19).[167] Electron microscopy and X-ray absorption spectroscopy revealed isolated $Cu–O_3$ coordination motifs, indicative of uniform atomic dispersion. DFT further supports enhanced electronic coupling and reduced charge-transfer resistance at these $Cu–O_3$ sites. Similarly, Zhao *et al.* immobilized Pt atoms at Ti vacancies in $Ti_3C_2T_x$ without external reducing agents, achieving spontaneous adsorption and Pt^{4+} reduction.[168] Park *et al.* further extended this strategy by generating V-vacant V_2CT_x MXene through deep HF etching, which subsequently stabilized isolated Pt atoms.[169] Other representative systems including $Ni–SACs/Ti_3C_2T_x$,[170] $Ag–SA(Ti_v)–Ti_3C_2$,[171] and $Ru–SA–Mo_2CT_x$[172] further demonstrate the generality of this defect-driven anchoring mechanism.

Alternative routes involve direct etching of metal-doped MAX precursors (*e.g.*, $Au–Ti_3AlC_2$, $Co–Mo_2Ga_2C$, $Fe–Mo_2Ga_2C$) to yield doped MXenes ($Au–Ti_3C_2T_x$,[173] $Co–Mo_2CT_x$,[174] $Fe–Mo_2CT_x$[175]) with uniformly dispersed atomic species. Lewis acid molten-salt etching also enables controlled single-atom incorporation: during etching in eutectic halide fluxes, metal halides act simultaneously as etchants and dopant sources, while subsequent acid leaching removes excess nanoparticles, leaving atomically anchored species such as Cu,[176] Fe,[177] or Zn.[178,179]

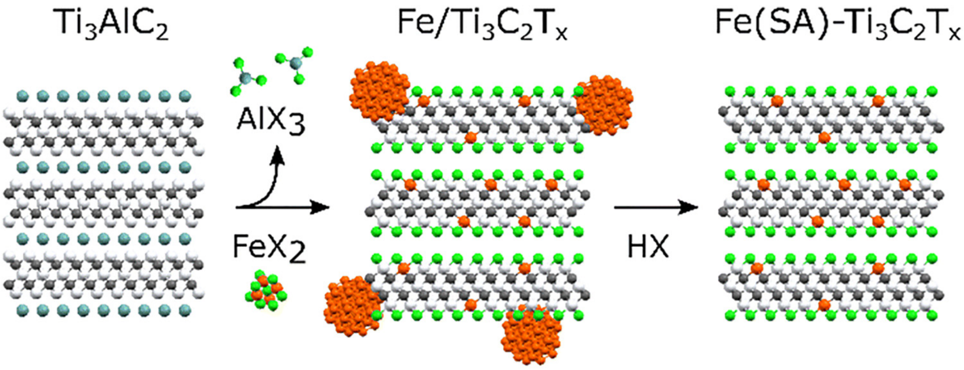

Fig. 20 Preparation of Fe single atoms on $Ti_3C_2T_x$ (T = Cl, Br) MXene. Reproduced from ref. 177 with permission from the Royal Society of Chemistry, copyright 2024.

For instance, Fe atoms stabilized on $Ti_3C_2T_x$ *via* FeX_2–AlX_3 molten salts exhibit uniform Fe–O coordination and strengthened electronic coupling (Fig. 20).[177]

Collectively, these findings demonstrate that MXene frameworks intrinsically support atom-level metal stabilization through synergistic coordination between surface terminations, native vacancies, and lattice defects. Despite this promise, achieving stable and uniform single-atom dispersion on MXenes remains challenging. Metal ions may cluster during reduction, and the true oxidation states and coordination environments of anchored atoms are often inferred indirectly. Single atoms may also migrate or aggregate under catalytic operation, but these processes are poorly understood due to the scarcity of *operando* atomic-resolution tools. Addressing these gaps will require precise precursor chemistry, strengthened anchoring environments and advanced real-time techniques capable of tracking single-atom evolution under working conditions, as well as clear criteria to distinguish genuine single-atom catalysts from systems dominated by subnanometric clusters.

3.3.4. Challenges and perspectives. While remarkable progress has been made, achieving fully controllable defect and doping engineering of MXenes remains an ongoing challenge. Quantitative characterization of vacancy concentration, dopant location, and coordination environment remains limited, as conventional techniques (*e.g.*, XPS, EPR, or STEM) lack atomic-level spatial precision. Moreover, the thermodynamic and kinetic stability of dopants or anchored atoms, particularly under reactive atmospheres or long-term cycling, remains poorly understood. Preventing dopant migration, aggregation, or defect healing under operating conditions is particularly crucial yet insufficiently explored.

Future advances will benefit from integrating *in situ*/*operando* spectroscopy with first-principles modelling and precisely tunable synthesis protocols (ion exchange, plasma-assisted etching, molten-salt substitution) to correlate defect populations with electronic structure in real time and to move from qualitative to quantitatively controlled defect engineering. Ultimately, more explicit descriptors that incorporate defect type, concentration, and dynamical behavior will be required to rationalize and compare defect-engineered MXenes across different studies.

3.4. Surface morphology control

Controlling the surface morphology of MXenes represents a fundamental dimension of atomic-to-mesoscale engineering aimed at optimizing their physicochemical behavior. Morphology governs key parameters such as surface area, interlayer accessibility, charge/mass transport, and structural resilience, all of which are crucial for performance in energy storage, electronic, and catalytic systems. Through rational design of porous, wrinkled, vertically aligned, or hierarchical architectures, one can manipulate geometric and electronic features, enhancing active-site exposure, reducing diffusion limitations, and stabilizing layered frameworks under operation. Morphological control therefore acts not only as a geometric modification but as an integrated approach to tailoring interfacial microenvironments and electronic coupling within and between MXene layers.[21,180–183]

3.4.1. Nanostructural and porosity engineering. Engineering porosity and nanoscale structure is among the most direct and effective strategies to enhance MXene functionality. Introducing ordered or disordered pores and modulating interlayer spacing enlarges accessible surface area and facilitates ion diffusion and molecular penetration. This strategy also suppresses nanosheet restacking, maintaining intrinsic 2D character and improving electrolyte wetting and charge transport. Ren *et al.* developed a mild room-temperature catalytic oxidation route to synthesize porous $Ti_3C_2T_x$ (p-$Ti_3C_2T_x$) using aqueous $CuSO_4$ solutions, in which Cu^{2+} ions catalyze the partial oxidation of MXene by dissolved O_2 to generate TiO_2 nanoparticles that are subsequently removed through acid etching (Fig. 21).[116] This self-templated process produces a well-defined mesoporous structure with abundant nanometre-scale pores distributed across the basal planes while preserving the hexagonal lattice symmetry of $Ti_3C_2T_x$. The resulting material exhibits a ten-fold increase in pore volume ($0.25\ cm^3\ g^{-1}$) and a five-fold rise in surface area ($\approx 94\ m^2\ g^{-1}$) compared with pristine MXene, arising from the combined contributions of oxidation-induced void formation and cation-intercalation expansion.

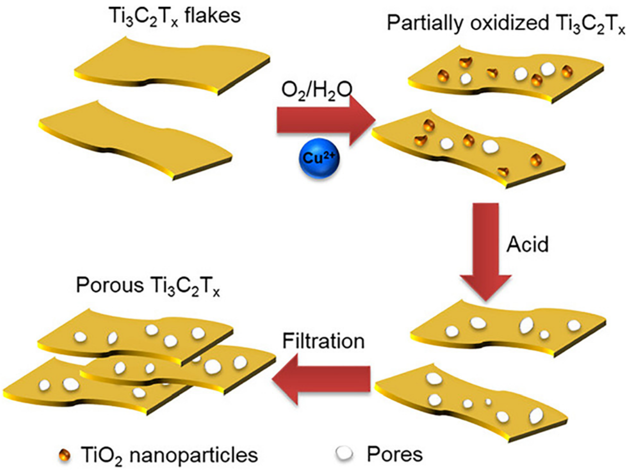

Fig. 21 Schematic showing the chemical etching of $Ti_3C_2T_x$ flakes to produce porous $Ti_3C_2T_x$ MXene structure. Reproduced from ref. 116 with permission from Wiley, copyright 2019.

Beyond structural modification, this etching mechanism involves Cu^{2+}-assisted O_2 activation and selective dissolution of TiO_2 intermediates, providing an atomic-level handle to tune termination chemistry: the proportion of –O and –OH groups increases while –F terminations decrease, resulting in enhanced surface hydrophilicity and charge accessibility. The porous $Ti_3C_2T_x$ can be readily assembled into flexible films or combined with carbon nanotubes to create hierarchical p-$Ti_3C_2T_x$/CNT composites featuring interconnected ion-transport channels and mechanical resilience. These architectures deliver remarkably high reversible Li-storage capacities up to 1250 mAh g^{-1} at 0.1 C, along with excellent rate performance and cycling stability, which clearly demonstrate the coupled roles of geometric confinement and electronic transport.

This strategy was further extended to Nb_2CT_x and V_2CT_x MXenes, as well as to other transition-metal salts (*e.g.*, $FeSO_4$, $CoSO_4$), illustrating that controlled partial oxidation followed by oxide removal constitutes a general and scalable pathway to construct porous MXenes with tunable pore size and distribution. Fundamentally, nanostructural and porosity engineering thus provide a robust means to couple surface accessibility with charge-transport pathways, balancing high electrical conductivity with efficient mass transfer and establishing the structural foundation for advanced functional integration of MXenes in energy and catalytic systems. However, several limitations remain. The formation of pores is often highly sensitive to subtle variations in precursor thickness, oxidation kinetics, or salt concentration, resulting in inconsistencies in pore uniformity and reproducibility. Furthermore, mesoporous frameworks may undergo structural coarsening or partial collapse during electrochemical cycling or thermal processing, yet such degradation processes are rarely monitored *operando*. These challenges highlight the need for more deterministic synthesis protocols and real-time structural probes to reliably correlate pore architecture with functional performance, as well as strategies to disentangle the respective contributions of porosity and termination chemistry to the observed electrochemical and catalytic metrics.

3.4.2. Supramolecular and templated morphology control. Beyond traditional chemical etching, supramolecular and template-assisted strategies offer powerful tools for directing MXene deformation and assembly across multiple length scales. Using macrocyclic molecules, polymers, surfactants, or sacrificial scaffolds, MXene layers can be induced to fold, curl, or self-organize into ordered superstructures. The resultant morphologies, ranging from wrinkled sheets to spherical or tubular forms, generate distinct interfacial environments with tunable curvature, electronic coupling, and defect density. Vaughn *et al.* developed a calixarene-directed supramolecular route to shape Ti_2C MXene into diverse architectures by employing p-phosphonic acid calix[*n*]arenes (PCX*n*, *n* = 4, 5, 6, 8) as molecular templates under ultrasonication (Fig. 22).[184] The ring size of the macrocycle dictated the resulting morphology: PCX_4 produced thin plate-like nanosheets with high lateral order, PCX_5 induced partial folding and crumpling through phosphonate coordination, PCX_6 yielded unprecedented hollow spheres *via* flexible intercalation and localized curvature, and PCX_8 generated well-defined scrolls with diameters of 0.5–0.9 μm. XPS analysis confirmed Ti–O–P bonding between MXene layers and the phosphonic acid moieties of the macrocycles, evidencing strong supramolecular and covalent interactions that stabilize the curved structures.

This work demonstrates how macrocycle geometry and conformational flexibility translate molecular recognition into mesoscale morphology, establishing a direct link between supramolecular chemistry and MXene assembly. Such curvature

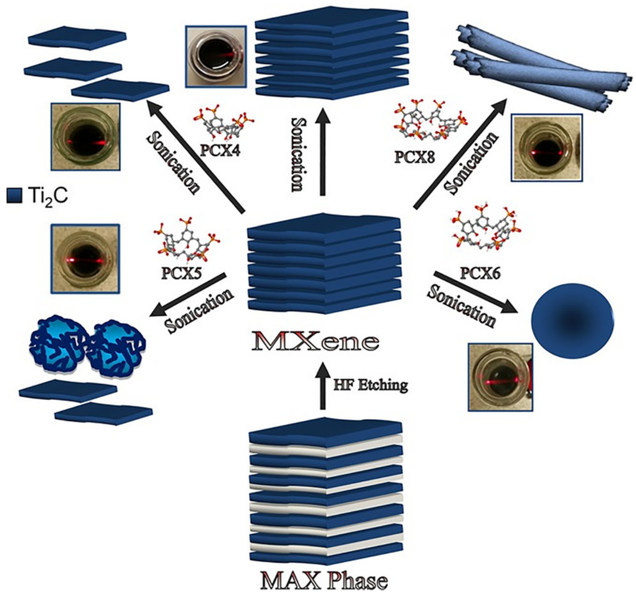

Fig. 22 Schematic illustration summarizing the synthesis of different morphologies of Ti_2C. The materials were derived from HF etched MXene, mediated by ultrasonication in the presence of *p*-phosphonic acid calix[*n*]arenes (PCX*n*). Note the Tyndall effect images for corresponding samples as confirmation of generating colloidal solution. Reproduced from ref. 184 with permission from Wiley, copyright 2017.

engineering modulates interlayer spacing, strain distribution, and d-orbital overlap, thereby tuning local DOS and surface reactivity without altering stoichiometry. Moreover, theoretical calculations predict that curved and scroll-like MXenes could exhibit strain-tunable electronic structures and band-gap modulation, underscoring the functional relevance of controlled morphology. Collectively, these supramolecular templating strategies illustrate that MXene morphology can be programmed through molecular design, enabling a new dimension of structural and electronic control. Despite these advantages, supramolecularly driven structures suffer from notable challenges, including sensitivity to solvent composition, pH, and sonication intensity, which often results in limited reproducibility. Additionally, the long-term structural stability of curved or rolled MXenes under electrochemical or thermal operation remains poorly understood. These issues indicate that further mechanistic studies and *operando* tools are needed to clarify how molecular recognition dictates mesoscale morphology and how curvature affects electronic behavior under working conditions.

3.4.3. Hierarchical and three-dimensional assembly. Constructing hierarchical or 3D MXene architectures enables the integration of atomic, nanoscale, and mesoscale features into unified frameworks. This approach mitigates sheet restacking, enhances mechanical robustness, and creates multidirectional transport channels for charge and mass. 3D structuring can be achieved through sol–gel assembly, freeze-casting, spray drying, or pyrolytic conversion, each offering distinct control over porosity and orientation.[185–187] Peng *et al.* prepared 3D porous N/P-*co*-doped $Ti_3C_2T_x$ nanosheets *via* a gel–pyrolysis route, achieving interconnected frameworks that maximized site exposure and facilitated mass transport (Fig. 23).[188] The controlled doping simultaneously modified bonding and electronic states, yielding synergistic regulation of conductivity and surface functionality. Similarly, Wu *et al.* produced 3D wrinkled $Ti_3C_2T_x$ by continuous spray drying, where the undulated morphology prevented aggregation and preserved high surface accessibility.[189] These structural motifs demonstrate that 3D hierarchical assembly extends beyond mere geometric optimization, enabling cooperative modulation of mechanical, electronic, and interfacial properties. The resulting architectures exhibit high conductivity, structural flexibility, and resistance to collapse, thereby serving as robust platforms for a wide range of electrochemical and catalytic applications.

Nevertheless, understanding how mesoscale ordering governs electronic coupling, defect distribution, and long-range charge transport remains limited. Many 3D structures rely on multi-step processing that is not easily scalable, and their mechanical integrity may degrade during extended cycling or exposure to harsh reaction media. Furthermore, the interplay between porosity, doping, and hierarchical connectivity is often evaluated qualitatively rather than quantitatively. Progress in this area will depend on multiscale simulations and *operando* imaging tools capable of directly linking structural hierarchy with electronic and transport phenomena, and on the development of quantitative descriptors that capture connectivity, tortuosity, and load-bearing capability in a manner comparable across different MXene architectures.

3.4.4. Structure–property correlation and outlook. Following substantial advances in morphological design, establishing correlations between structural parameters and functional properties remains a major challenge. Quantitative understanding of how pore topology, curvature, or hierarchical order influences electronic density and interfacial interactions is limited by the scarcity of *in situ* and multiscale characterization. Moreover, reproducibility and scalability remain obstacles, as delicate morphological features can be altered during synthesis or processing. Separating morphology-driven effects from those introduced by binders, spacers, or secondary support phases in practical environments adds further complexity. Future progress will benefit from coupling *in situ*/*operando* microscopy and spectroscopy (*e.g.*, environmental TEM, *operando* AFM, synchrotron scattering) with multiscale simulations and machine learning to map morphology–property spaces and identify optimal architectures. Such insights will be important for translating mesoscale structural design into robust and reproducible performance across electrochemical and catalytic applications.

3.5. Summary and perspectives

Surface engineering has established itself as a powerful strategy for modulating the intrinsic physicochemical properties of MXenes at the atomic scale. By integrating compositional tuning, controlled surface terminations, defect/dopant regulation, and morphology design, the preceding sections illustrate how multiple dimensions of surface control can be orchestrated to reshape electronic structure, charge distribution,

Fig. 23 Schematic illustration of the synthetic route of Pt SA-3D porous N, P codoped $Ti_3C_2T_x$ MXene. Reproduced from ref. 188 with permission from American Chemical Society, copyright 2022.

and structural hierarchy. These efforts have elevated MXenes from simple conductive sheets to highly tunable materials capable of programmable stability, conductivity, and surface reactivity. In combination, these diverse strategies create a coherent toolbox that enables fine control from atomic bonding environments to mesoscale architecture, providing a comprehensive foundation for subsequent interface engineering.

Despite these advances, the capabilities achievable within a single MXene layer remain inherently constrained by its intrinsic band structure, surface area, and charge density. Further improvements, such as directional charge transfer, spatially separated redox sites, or broadband light absorption, often require coupling MXenes with external components. Moreover, surface terminations may reach chemical or structural saturation, limiting the extent of Fermi-level alignment or carrier-dynamics modulation. Excessive defect densities may compromise stability, and *ex situ* characterizations often fail to capture the *operando* surface state. These factors collectively highlight the need to extend atomic-level control beyond individual MXene layers.

This realization naturally points to heterostructure interface engineering, in which MXenes function as electronic mediators or structural scaffolds within composite systems. By integrating MXenes with semiconductors, metals, or other layered materials, one can generate interfacial band bending, charge redistribution, and built-in electric fields, phenomena not attainable through single-phase MXenes. Such heterostructures enable directional carrier flow, enhanced exciton separation, and cooperative intermediate activation, providing a multidimensional platform for integrating conductivity, chemical activity, and photothermal response.

Therefore, while surface engineering defines the intrinsic capabilities of MXenes, heterostructure interface engineering determines how these capabilities are expressed and amplified in functional environments. The next chapter builds on this foundation, elucidating how interfacial design principles, including band alignment, charge transfer, and structural coupling, transform MXenes from tunable 2D materials into universal interface mediators bridging atomic-scale control with macroscopic catalytic performance.

4. Heterostructure interface engineering of MXenes

While surface engineering enables atomic-level modulation of MXene composition, electronic structure, and morphology, its impact is ultimately confined to a single material phase. Many key functions, such as directional charge transport, spatially separated redox sites, and coupled optical–electronic responses, cannot be achieved through further refinement of an isolated MXene layer. Accordingly, recent research has shifted from optimizing individual MXenes toward engineering the interfaces they form with other functional materials, extending structural and electronic design from the intralayer to the heterostructure level.[190]

A heterostructure is a composite system in which two or more materials with distinct compositions or electronic properties are integrated at the atomic or nanoscale. Within such architectures, MXenes serve as both conductive scaffolds and chemically adaptive platforms: their metallic or quasi-metallic nature supports ultrafast charge and ion transport, while their rich surface terminations (–O, –OH, –F, *etc.*) provide versatile bonding motifs with metals, semiconductors, carbons, and polymers. This combination allows MXenes to mediate electronic and chemical contact between materials of different dimensionalities and band structures, positioning them as active interfacial couplers rather than passive fillers.[183,191–193] Nevertheless, broadly transferable design rules remain limited because reported hybrids are often system-specific.

The essence of MXene-based interface engineering lies in emergent interfacial phenomena that arise only when multiple phases interact electronically, structurally, and chemically. These couplings manifest in several key dimensions (Fig. 24): (i) electronic regulation, where Fermi-level equilibration and charge redistribution establish built-in electric fields and reshape local densities of states; (ii) structural coupling, in which lattice matching, orbital hybridization, and termination bonding generate coherent interfaces with reduced defect density and enhanced mechanical stability; and (iii) chemical stabilization, where strong interfacial adhesion suppresses oxidation, aggregation, and phase degradation of MXenes. Together, these effects create cooperative functionalities beyond those achievable by single-phase MXenes.

Building upon these principles, MXene-based heterostructures can be broadly classified by the nature of the secondary component (Fig. 24): (i) MXene/metal interfaces characterized by Schottky or Ohmic contacts and strong metal–support interactions (SMSI); (ii) MXene/metal compound heterostructures (*e.g.*, oxides, sulfides, nitrides) that facilitate efficient charge separation *via* Z-scheme or S-scheme mechanisms; (iii) MXene/carbon hybrids (graphene or carbon nanotubes (CNTs)) that mitigate restacking and enhance structural continuity; and (iv) MXene/polymer composites that regulate interlayer spacing, mechanical elasticity, and ion/proton conductivity. These categories capture the dominant modes of electronic and chemical coupling, ranging from metallic to covalent or supramolecular interactions. This chapter therefore focuses on the underlying interfacial design principles, rather than an exhaustive catalogue of materials, and highlights how each interface type exposes general opportunities and constraints unique to MXenes as interfacial mediators.

4.1. MXene/metal heterostructure interfaces

MXene/metal heterostructures represent one of the most fundamental classes of MXene-based interfaces, in which metallic species ranging from isolated atoms to nanoparticles and nanofilms are anchored onto, or embedded within, the 2D MXene matrix. These systems integrate the metallic conductivity and structural adaptability of MXenes with the diverse electronic configurations and coordination environments of metals, creating highly interactive junctions governed by strong

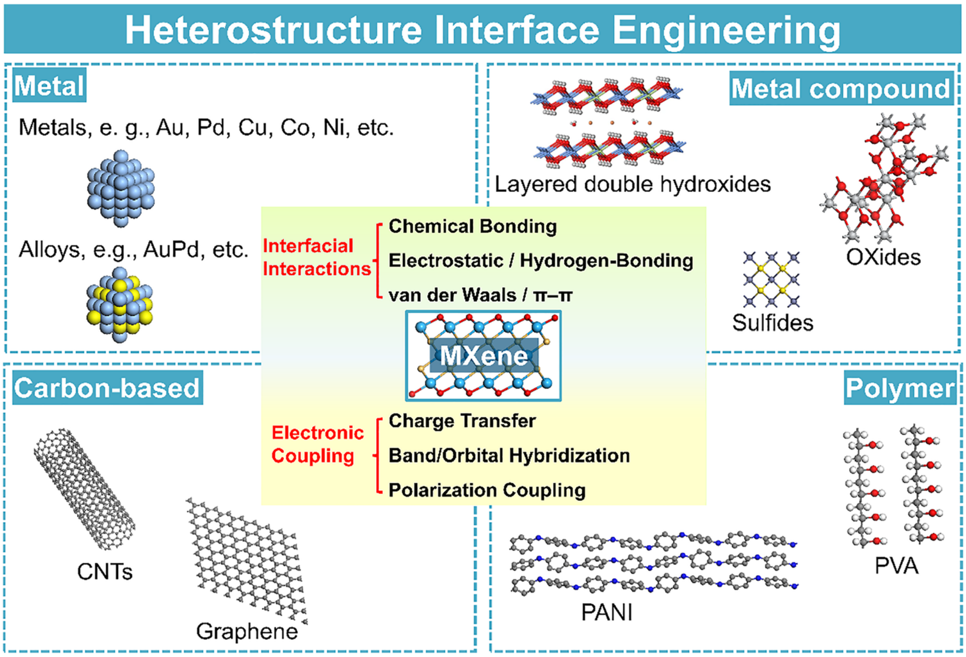

Fig. 24 Hierarchical schematic of MXene heterostructure interface engineering.

electronic and chemical coupling. The resulting interfaces exhibit complex charge redistribution, orbital hybridization, and local structural reconstruction, which collectively determine electronic alignment, bonding, and stability.[194,195]

MXenes provide an exceptionally suitable platform for metallic integration owing to several intrinsic attributes. Their metallic or quasi-metallic conductivity ensures efficient electron exchange across the interface, while hydrophilic and chemically active surface terminations (–O, –OH, –F, *etc.*) offer abundant anchoring sites for metal ions. In addition, their large surface area and tunable interlayer spacing allow uniform dispersion and spatial confinement of metal species. These features yield SMSI that markedly alter local charge density and bonding at the junction. Compared with graphene or other carbon-based hosts, MXenes exhibit higher surface polarity and interfacial reactivity, which reduces aggregation and supports more deterministic metal placement at the atomic level.

4.1.1. Synthesis pathways and structural configurations. The formation of well-defined MXene/metal interfaces relies on precisely controllable synthetic routes that dictate the distribution, bonding mode, and electronic continuity between the two phases. MXene/metal heterostructures are typically fabricated through *in situ* reduction, intercalation, or reactive diffusion methods, which enable fine control of metal loading, distribution, and coordination environment. In a representative approach, Zhang *et al.* established a general *in situ* reduction strategy that enables $Ti_3C_2T_x$ MXene to directly reduce a broad range of metal cations including Au^{3+}, Pd^{2+}, Ag^{+}, Pt^{4+}, Rh^{3+}, Ru^{3+}, and Cu^{2+} without any external reductant (Fig. 25).[196] The electron transfer originates from Ti^{2+}/Ti^{3+} surface species, which act as intrinsic reducing centers and drive the nucleation of isolated metal atoms that subsequently evolve into clusters or nanoparticles with increasing loading. The resulting composites exhibit uniform dispersion and size tunability dictated by interlayer confinement and surface defect density. DFT and spectroscopy analyses consistently show that metals preferentially anchor at Ti vacancies, where local charge density and coordination asymmetry reduce the adsorption energy barrier.

Beyond monometallic systems, the same *in situ* protocol affords bimetallic alloys and core–shell nanostructures such as AgAu-, Pd@Au-, Pt@Au-, and Ag@Pd@Au-MXenes through sequential or co-reduction steps. The deposition sequence and coordination environment modulated, for example, by ethylenediaminetetraacetic acid (EDTA) complexation influence whether alloying or epitaxial core–shell growth predominates.

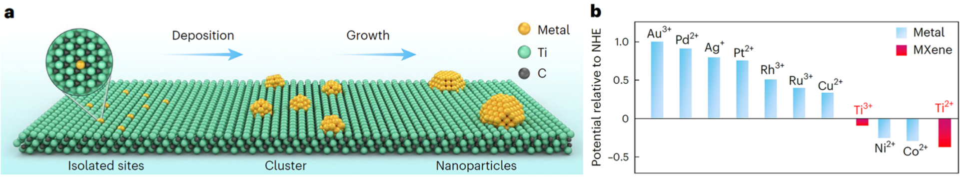

Fig. 25 (a) Schematic illustration of metal depositing on the surface of MXene by *in situ* reduction. (b) A comparison of redox potentials of the $Ti_3C_2T_x$ MXene and metal ions. Reproduced from ref. 196 with permission from Springer Nature, copyright 2024.

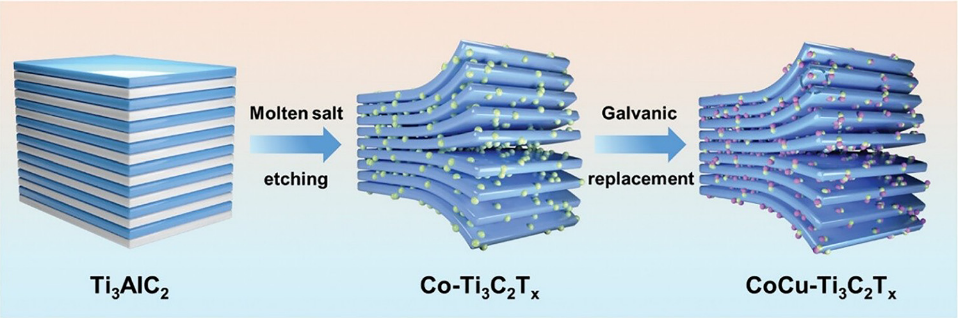

Fig. 26 The synthesis scheme of CoCu–$Ti_3C_2T_x$. Reproduced from ref. 198 with permission from Wiley, copyright 2024.

Lattice mismatch further governs spatial selectivity. Metals with small mismatches to $Ti_3C_2T_x$ (*e.g.*, Au, Ag) tend to grow continuously on basal planes, whereas larger mismatches (*e.g.*, Pd, Rh, Pt) promote edge-selective deposition. The edge-first deposition of Au, driven by the electrostatic attraction between positively charged MXene edges and negatively charged $AuCl_4^-$, highlights how local charge distribution shapes nucleation pathways. These findings reveal that the interplay among redox potential, coordination environment, and lattice strain dictates the nucleation mode, site selectivity, and final architecture of MXene/metal composites. Such examples illustrate that MXene surfaces do not merely host metals, but they actively direct their spatial organization.

In addition, Lewis acidic molten-salt etching provides a second, intrinsically interfacial route for metal incorporation. During synthesis, metal cations present in molten salt (*e.g.*, Cu^{2+}, Ni^{2+}, Co^{2+}) can be reduced on the MXene surface, forming metallic nanoclusters embedded within the layered framework. Although these inclusions are often removed to obtain pure MXenes, several studies have exploited them as functional hybrids. For instance, Cui *et al.* showed that MXene/CuNi (or Co) composites prepared *via* molten-salt reduction exhibit strong metal–support coupling and excellent compositional uniformity, resulting in enhanced structural robustness (Fig. 26).[197,198] Moreover, selective acid washing (*e.g.*, using HCl or ammonium persulfate, APS) can remove large aggregates while preserving atomic or subnanometer metal species (Fe,[177] Ni,[199] Cu[176]), offering a practical and scalable route toward single-atom metal/MXene hybrids.

Reactive metal–support interaction (RMSI) provides an additional pathway to ordered intermetallic phases directly on MXene substrates. Li *et al.* reported the formation of ordered Cu_3Au-type intermetallic compounds (IMCs) such as Pt_3Ti on $Ti_3C_2T_x$ and Pt_3Nb on Nb_2CT_x MXenes (Fig. 27a–c).[200] These

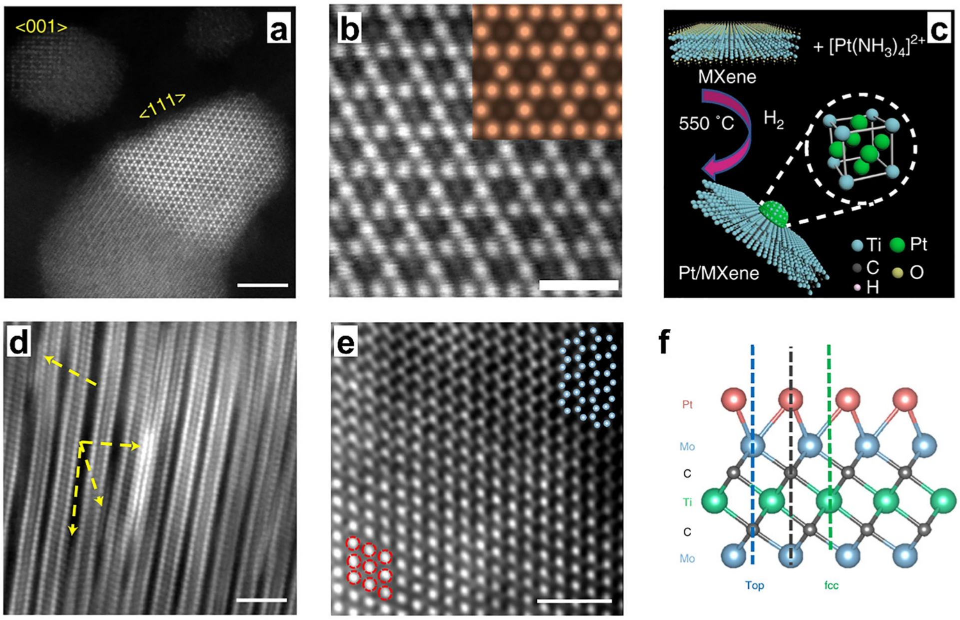

Fig. 27 Microscopy characterizations of Pt/MXene catalysts. (a) Representative HAADF-STEM image of 1% Pt/$Ti_3C_2T_x$ catalyst. (b) (111) surface of Pt_3Ti NP. Inset is a simulated STEM image of Pt_3Ti(111) surface. (c) Schematic illustration of RMSI in Pt/MXene catalysts and the structure of $L1_2$-ordered intermetallic Pt_3Ti. HAADF-STEM image of Pt/$Mo_2TiC_2T_x$ viewed from the [11$\bar{2}$0] direction (d) and the [0001] direction (e). (f) Relaxed structure showing Pt atoms occupying hcp sites on the surface of $Mo_2TiC_2T_x$ MXene. Reproduced from (a)–(c) ref. 200, (d)–(f) ref. 201 with permission from Springer Nature, copyright 2018 and 2021.

atomically ordered structures display strong intermetallic bonding between Pt and M (Ti or Nb), delivering exceptional structural stability and electronic coupling. RMSI-driven IMC formation reflects a thermodynamic preference for interfacial alloying at elevated temperatures, producing coherent metal–MXene interfaces characterized by atomic continuity and enhanced robustness.

Li *et al.* further achieved epitaxial growth of single- and double-atomic-layer Pt nanofilms on Mo_2TiC_2 MXene (Fig. 27d–f), stabilized by strong Pt–Mo interfacial bonding.[201] These atomically thin metallic layers show outstanding uniformity and precisely tunable thickness, representing a distinct regime between isolated atoms and extended metal films. Such systems exemplify the potential of MXenes to template atomic-scale ordering, driven by synergistic interplay between the transition-metal sublattice and the deposited metallic species.

In summary, these synthetic strategies demonstrate that MXenes not only act as supports but also behave as structure-directing platforms that modulate nucleation, alloying, and atomic ordering. However, the high sensitivity of MXene surfaces to subtle variations in termination chemistry or precursor conditions continues to hinder reproducibility, underscoring the need for more rigorous interface-controlled synthesis.

4.1.2. Electronic interactions and charge redistribution. With the interfacial architectures established, the next crucial question is how electronic coupling unfolds at the junction and how charge redistribution governs transport behavior. At the heart of every MXene/metal interface lies a competition between electronic hybridization and charge equilibration, which together determine Fermi-level alignment, carrier mobility, and interfacial stability. When a metal and an MXene come into contact, differences in work functions (Φ) and Fermi energies (E_F) drive charge transfer until equilibrium is established. Depending on the relative magnitudes of Φ_{MXene} and Φ_{metal}, the resulting contact exhibits either Schottky or Ohmic characteristics. For instance, deposition of high-work-function metals such as Pt, Pd, or Au on $Ti_3C_2T_x$ ($\Phi \approx 1.6$–5.8 eV, termination-dependent) induces electron flow from MXene to the metal, forming a Schottky barrier that controls interfacial carrier injection. Conversely, low-work-function metals such as Cu, Ni, or Co establish nearly barrierless Ohmic contacts, facilitating efficient bidirectional charge transport. These behaviors are further modulated by surface terminations, whose electronegativity directly determines dipole direction and band bending.

This Fermi-level equilibration produces band bending and an interfacial dipole layer, resulting in spatial variations in carrier density and surface potential. The polarity and strength of this dipole depend strongly on the surface termination chemistry: O-terminated MXenes, due to their high electronegativity, withdraw charge from adjacent metals, leading to downward band bending, whereas OH-terminated surfaces promote more symmetric coupling. DFT simulations indicate that hybridization between metal d-orbitals and Ti d- or O p-states gives rise to new interfacial states near E_F, thereby smoothing potential barriers and enhancing tunneling efficiency.

Experimental evidence supports these theoretical predictions. XPS and Kelvin probe force microscopy (KPFM) reveal core-level shifts and surface potential variations upon metal deposition, confirming substantial charge redistribution. Time-resolved spectroscopic measurements, including transient absorption and time-resolved photoemission, demonstrate sub-picosecond carrier equilibration at well-coupled interfaces, while bias-dependent KPFM mapping visualizes the evolution of interfacial dipoles under applied fields. Under optical excitation, plasmonic or hot-electron effects in MXene/noble-metal junctions can transiently lower effective barriers, linking static electronic alignment to dynamic photophysical behavior.

Despite strong experimental and theoretical progress, quantitative mapping of electronic alignment in MXene/metal interfaces remains limited. Reported Schottky barrier heights frequently vary across studies due to differences in termination chemistry, flake oxidation, and residual etching by-products, which complicate reproducibility. Moreover, most measurements rely on *ex situ* characterization, whereas interfacial dipoles and charge densities evolve dynamically during catalysis, heating, or illumination. The absence of *operando*-level electronic–structural correlation hampers the establishment of universal design rules. Developing real-time probes that resolve how terminations and defects reshape interface energetics will be essential for predictive control.

4.1.3. Interfacial reconstruction and atomic-level ordering. Beyond static electronic modulation, strong interfacial interactions often drive structural self-reorganization aimed at minimizing interfacial energy and enhancing electronic coherence. Under elevated temperatures or reactive conditions, partial interdiffusion, lattice rearrangement, and ordered phase formation can occur, yielding interfaces with atomically coherent structure and uniform bonding networks.

As reported by Li *et al.*, the formation of ordered Pt_3Ti and Pt_3Nb intermetallics on $Ti_3C_2T_x$ and Nb_2CT_x MXenes exemplifies RMSI-driven ordering. High-resolution TEM and X-ray absorption spectroscopy (XAS) confirmed continuous Pt–M coordination and strong d-orbital hybridization across the interface. This reconstruction produces atomically sharp boundaries with reduced defect densities and uniform charge distribution, ensuring mechanical integrity and electronic coherence. The epitaxial growth of Pt nanofilms on Mo_2TiC_2 MXene, stabilized through Pt–Mo bonding, further illustrates this phenomenon. The resulting ultrathin metallic layers bridge the gap between atomic and bulk regimes, providing quantum-level precision over interface thickness and electron coupling. *Operando* environmental TEM combined with electron energy-loss spectroscopy (EELS) has directly visualized adatom diffusion, nucleation, and ordering pathways on MXene surfaces, confirming that MXene terraces act as energetically favourable diffusion pathways for interfacial alloying and reconstruction. These atomic rearrangements yield graded interfaces with smooth bonding transitions, which span ionic, covalent, and metallic regimes, thereby minimizing interfacial resistance and enhancing durability. Moreover, strain accommodation within MXene layers suppresses crack propagation and helps preserve lattice coherence under thermal or electrochemical stress. Consequently, interfacial reconstruction emerges as a key self-regulating mechanism, enabling MXenes to dynamically optimize bonding uniformity and defect tolerance in response to external stimuli.

Although interfacial reconstruction can significantly enhance bonding coherence, its thermodynamic driving forces and kinetic pathways remain poorly quantified. Small variations in MXene defect density, termination composition, or metal precursor chemistry often lead to divergent reconstruction behaviors, raising concerns regarding reproducibility. In addition, prolonged operation may induce unintended interdiffusion or phase drift, which alters active-site geometry and complicates long-term performance evaluation. Systematic *operando* studies are still lacking to determine whether reconstructed interfaces are stable or gradually evolve during catalysis, electrochemical cycling, or thermal stress, highlighting the need for real-time monitoring to avoid misattributing transient phases as stable structural motifs.

4.1.4. Challenges and perspectives. Although significant progress has been achieved in tailoring MXene/metal interfaces, attaining deterministic atomic-level control over interfacial structure and composition remains challenging. The dynamic nature of metal nucleation, diffusion, and oxidation on functionalized MXene surfaces often leads to particle size dispersion, clustering, or partial passivation, complicating efforts to precisely define atomic configurations. Furthermore, decoupling electronic and geometric effects on interfacial stability requires *in situ* characterization tools capable of simultaneously resolving charge distribution and atomic structure. Future progress will rely on integrating atomic-layer deposition (ALD), molecular beam epitaxy (MBE), and controlled molten-salt methods with *in situ* electron microscopy and *operando* spectroscopy to visualize interface evolution in real time. The development of predictive computational frameworks linking Fermi-level alignment, charge redistribution, and atomic ordering will further enable rational design of MXene/metal systems with programmable interface properties.

At its core, the study of MXene/metal heterostructures underscores a central tenet of interface science: the emergent properties of a junction are not merely the simple sum of its constituents but arise from their cooperative interactions. By mastering the interplay among electronic coupling, structural reconstruction, and chemical bonding, researchers can achieve atomic-level precision in controlling interfacial conductivity, stability, and reactivity. Despite these advances, current research remains highly system-specific, and the absence of transferable descriptors or universal structure–property correlations limits the predictive power of existing design strategies. Such understanding lays the conceptual groundwork for integrating MXene-based interfaces into next-generation functional materials. While these insights primarily pertain to metallic contacts, they also provide a framework for more complex MXene/metal-compound heterostructures, where charge redistribution and built-in electric fields jointly govern directional carrier transport and interfacial dynamics.

4.2. MXene/metal compound heterostructure interfaces

While MXene/metal interfaces are dominated by metallic bonding and Fermi-level equilibration, integrating MXenes with metal compounds such as oxides, sulfides, and nitrides introduces semiconducting characteristics and band-structure complementarity that extend beyond simple charge exchange.[202,203] Compared with the MXene/metal contacts discussed in Section 4.1, these hybrid junctions add an additional degree of freedom associated with band-gap and band-edge engineering in the compound phase. In these systems, the junction typically behaves as a Schottky or Ohmic contact when the MXene exhibits metallic or quasi-metallic character, whereas under specific surface states or partial oxidation conditions, MXenes may display semiconducting behavior capable of forming Z-scheme or S-scheme heterojunctions (Fig. 28).

At the metal–semiconductor interface, a Schottky or Ohmic contact is established depending on the relative positions of their Fermi levels. When the metal possesses a larger work function (*i.e.*, a lower Fermi level) than the semiconductor, electrons flow from the semiconductor to the metal until equilibrium is reached, forming a Schottky junction with a depletion region and a built-in electric field directed from the semiconductor toward the metal. The resulting Schottky barrier height (Φ_{SB}), governed by the work-function difference between the two components, determines the efficiency of charge transfer. By tailoring MXene surface terminations or selecting metals with appropriate Φ values, Φ_{SB} can be optimized to facilitate electron injection, suppress recombination, and enhance catalytic activity. Conversely, when the metal has a smaller work function (*i.e.*, a higher Fermi level), electrons transfer from the metal to the semiconductor, producing an Ohmic contact that enables nearly barrier-free carrier transport. When MXenes couple with semiconducting metal compounds, the interfacial behavior often follows a Z-scheme or S-scheme mechanism driven by Fermi-level equilibration and internal electric-field formation. In this configuration, electrons from the reduction photocatalyst (RP), typically the component with the smaller work function, spontaneously diffuse toward the oxidation photocatalyst (OP), establishing an electric field oriented from RP to OP. Under illumination, the built-in field promotes selective recombination of low-energy carriers, namely electrons

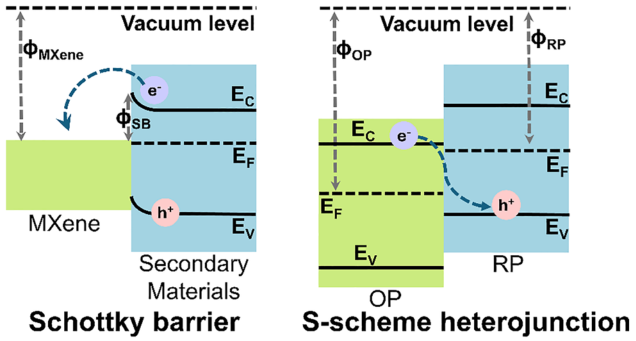

Fig. 28 Schematic illustration of interfacial electronic coupling in MXene/metal compound heterostructures.

in the OP conduction band and holes in the RP valence band, while preserving high-energy electrons in the RP conduction band and holes in the OP valence band. This selective recombination preserves strong redox potentials while maintaining spatial charge separation, making Z-scheme/S-scheme heterojunctions particularly effective for energy-intensive catalytic processes such as CO_2 reduction or oxidative pollutant degradation.[204–206]

Collectively, these interfacial configurations demonstrate how MXenes act as both conductive mediators and electronic regulators, bridging metallic, semiconducting, and redox-active components. By modulating interfacial work-function offsets and band alignment, researchers can precisely control charge flow, band bending, and catalytic energetics. However, fully resolving whether a given MXene/compound pair forms a Schottky, Ohmic, Z-scheme, or S-scheme junction remains non-trivial, because subtle variations in termination chemistry, oxidation degree, and defect distribution can shift the dominant mechanism, underscoring the need for more unified criteria for heterojunction identification.

4.2.1. Synthesis pathways and interfacial architectures. The construction of MXene/metal-compound heterostructures primarily relies on solution-phase assembly routes that ensure intimate interfacial bonding and well-controlled phase distribution. Among them, hydrothermal growth and self-assembly are the most widely employed and effective strategies.

In hydrothermal synthesis, metal compounds nucleate and grow *in situ* on the MXene surface under mild conditions, ensuring strong interfacial adhesion and atomic-level coupling. Cao *et al.* directly grew Bi_2WO_6 nanosheets on Ti_3C_2 MXene *via* electrostatically driven hydrothermal deposition, forming ultrathin 2D–2D Ti_3C_2/Bi_2WO_6 heterostructures (Fig. 29).[207] The negatively charged Ti_3C_2 surface facilitated Bi^{3+} adsorption, guiding directional growth and producing interfaces with large contact areas and short carrier migration distances. Such coherent interfacial growth enhances electronic continuity and enables efficient charge redistribution across the boundary, outperforming either single component. Similarly, Li *et al.* synthesized $Bi_2S_3/Ti_3C_2T_x$ heterostructures where the difference in work functions between the two components induced Schottky barrier formation, driving spontaneous electron transfer from $Ti_3C_2T_x$ to Bi_2S_3 and establishing a built-in potential that promoted unidirectional carrier flow and suppressed back recombination.[208] These examples highlight that hydrothermal assembly not only preserves structural integrity but also enables direct control of Fermi-level alignment and interfacial dipole strength.

Complementary to hydrothermal synthesis, self-assembly strategies rely on van der Waals or electrostatic interactions to achieve uniform dispersion of metal compounds without disturbing the MXene framework. Liu *et al.* demonstrated a versatile self-assembly route for anchoring TiO_2 nanorods and SnO_2 nanowires on Ti_3C_2 MXene *via* van der Waals coupling (Fig. 30).[209] The anchored nanostructures acted as ''spacers,'' preventing MXene restacking and maintaining open interlayer channels for efficient electron and ion transport. Zhang *et al.* further constructed Fe_3O_4/MXene heterostructures through interfacial self-assembly, enabling spontaneous deposition of Fe_3O_4 nanodots on $Ti_3C_2T_x$ nanosheets.[210] The van der Waals-driven self-organization ensured intimate contact and structural complementarity, with MXene serving as a conductive backbone and Fe_3O_4 nanodots preventing agglomeration and reinforcing structural integrity. Together, these mild assembly routes produce coherent heterointerfaces in which chemical bonding, interfacial dipoles, and charge-transport pathways are simultaneously optimized.

To conclude, hydrothermal and self-assembly approaches provide controllable pathways to coherent interfacial architectures. Nevertheless, reproducibility remains a major bottleneck,

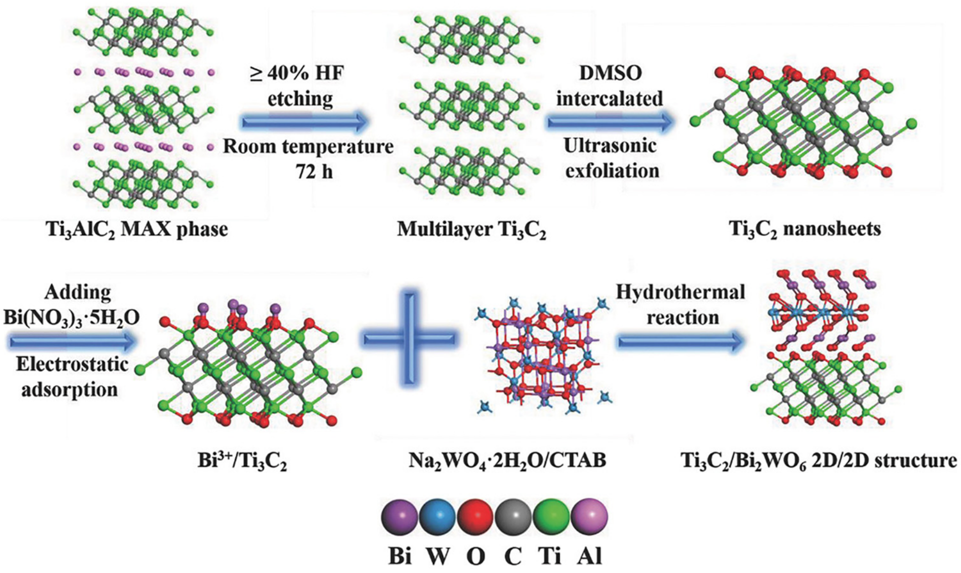

Fig. 29 Schematic illustration of the synthetic process of 2D/2D heterojunction of ultrathin Ti_3C_2/Bi_2WO_6 nanosheets. Reproduced from ref. 207 with permission from Wiley, copyright 2018.

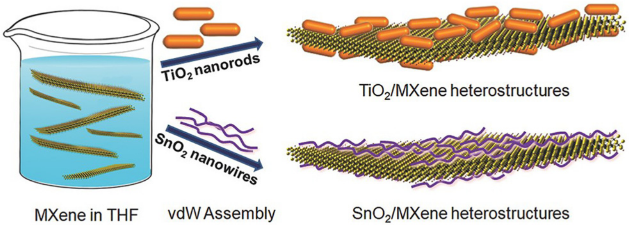

Fig. 30 Schematic diagram for the simple self-assembly of TMO nanostructures, including TiO_2 nanorods and SnO_2 nanowires, on MXene nanosheets in THF through van der Waals interactions. Reproduced from ref. 209 with permission from Wiley, copyright 2018.

as slight variations in precursor compositions, MXene termination states, or local oxidation environments can lead to markedly different nucleation behaviors. Moreover, the susceptibility of MXenes to partial hydrothermal oxidation complicates the establishment of universal synthesis conditions, underscoring the need for *operando* monitoring to prevent artefactual interfacial chemistries.

4.2.2. Electronic coupling and heterojunction mechanisms. The electronic characteristics of MXene/metal-compound interfaces depend critically on whether the MXene behaves as a metallic conductor or a semiconducting participant. In most cases, metallic or quasi-metallic MXenes (*e.g.*, $Ti_3C_2T_x$, Nb_2CT_x) establish Schottky or Ohmic contacts with semiconducting metal compounds, governed by differences in work functions. While Schottky contacts enable rectified carrier transport through built-in potential barriers, Ohmic contacts provide barrier-free pathways; both facilitate efficient carrier transfer and suppress charge recombination. When surface oxidation or specific terminations narrow the MXene band gap or lower carrier density, it can behave as a semiconductor, giving rise to Z-scheme or S-scheme heterojunctions in which built-in electric fields drive directional charge separation while preserving strong redox potentials.

At the atomic scale, Fermi-level equilibration induces interfacial band bending, orbital overlap, and dipole formation. DFT calculations show that interfacial Ti–O or Ti–S coordination generates hybridized states near the Fermi level, narrowing the local band gap and promoting electronic delocalization across the junction. Simultaneously, chemical coupling *via* –O or –S terminations mediates dipole formation and modulates work-function alignment. The resulting hybridized frontier orbitals act as conduits for interfacial charge migration, enabling efficient, spatially directed carrier flow. This cooperative interplay of electronic alignment, interfacial polarization, and orbital hybridization defines the core mechanism of MXene/metal-compound heterostructures.

Despite these insights, quantitative analysis of band alignment and dipole formation remains limited. Reported values of Schottky barriers, band offsets, and interfacial potentials often differ substantially due to variations in MXene oxidation, termination composition, and flake quality. Furthermore, most available data are obtained *ex situ*, whereas the electronic landscape can shift dynamically under illumination, electric bias, or reactive environments. This disparity highlights the need for *operando* band-structure mapping to establish reliable design rules for MXene/metal-compound heterojunctions.

4.2.3. Structural coherence and interfacial stability. The structural integrity and long-term durability of MXene/metal-compound interfaces are governed by lattice compatibility, bonding continuity, and interfacial dipole strength. The layered flexibility of MXenes allows strain accommodation and semi-coherent lattice coupling with crystalline oxides, sulfides, and nitrides, minimizing interfacial dislocations and mismatches. M–O, M–S, and M–N coordination bridges reinforce adhesion and facilitate orbital overlap across the boundary, while strong interfacial dipoles stabilize charge distribution and suppress oxidation or defect propagation. This hybrid bonding environment yields chemically graded interfaces that transition from ionic to covalent character, maintaining both electronic continuity and mechanical compliance. Moreover, the hydrophilicity and surface polarity of MXenes allow them to integrate with both polar oxides and less polar sulfides or nitrides, ensuring assembly and structural resilience under redox or thermal cycling.

However, the structural "compliance" of MXenes is a double-edged sword. While flexibility aids lattice matching, it also makes interfaces vulnerable to gradual distortion, layer delamination, or termination loss under electrochemical cycling. In addition, buried interfacial coordination structures remain poorly resolved, and the extent to which dipole-induced stabilization persists under sustained operating conditions is still unclear. More systematic *operando* structural studies are required to differentiate stable interfacial motifs from transient, synthesis-induced artefacts.

4.2.4. Challenges and perspectives. While substantial progress has been realized, achieving precise control over the electronic configuration and structural uniformity of MXene/metal-compound interfaces remains difficult. The dual metallic–semiconducting behavior of MXenes complicates junction-type prediction, as work function and band alignment are highly sensitive to surface terminations, defect density, and oxidation state. Additionally, quantitative characterization of buried interfaces, including band bending, dipole strength, and coordination structure, remains difficult due to dynamic surface reconstruction during synthesis. Ensuring phase purity, chemical uniformity, and lattice coherence during hydrothermal or self-assembly growth demands meticulous control over reaction kinetics and nucleation pathways. At present, classifications of junction type in MXene/compound systems are still largely post hoc, inferred from macroscopic performance rather than from rigorously determined interfacial energetics, which limits the transferability of current design rules.

Looking ahead, integrating *in situ*/*operando* characterization techniques (*e.g.*, synchrotron XPS, TEM-EELS, and XAS) with multiscale modelling will be crucial for visualizing interface evolution and charge redistribution in real time. Machine-learning-guided synthesis may further enable predictive control over termination chemistry and band alignment. Ultimately, developing reliable, quantitative relationships between MXene surface chemistry and interfacial electronic structure will provide the foundation for designing MXene/metal-compound heterostructures with programmable fields, directed charge transport, and superior catalytic functionality.

4.3. MXene/carbon heterostructure interfaces

MXene/carbon heterostructures represent a distinct class of hybrid interfaces that integrate the metallic conductivity, surface polarity, and chemical tunability of MXenes with the high surface area, stability, and mechanical resilience of carbon materials. From an interface-engineering standpoint, these systems exploit complementary characteristics: MXenes provide abundant surface terminations (–O, –OH, –F) that act as anchoring and coupling sites, while carbon materials such as graphene, carbon nanotubes (CNTs), and amorphous carbons contribute robust sp^2 frameworks and excellent structural stability. The combination yields electronically continuous and mechanically flexible junctions, where covalent, electrostatic, or π-mediated interactions create coherent charge-transfer networks. Importantly, these interfaces also serve as model platforms for probing how metallic and sp^2-carbon phases couple electronically and chemically at 2D boundaries, offering mechanistic insights that cannot be accessed using either material alone.

4.3.1. Interfacial bonding and structural configuration. The bonding configuration at the MXene/carbon interface governs both electronic communication and mechanical cohesion. Covalent linkages, particularly Ti–O–C and, under suitably deoxygenated conditions, Ti–C bonds, enable orbital overlap between MXene transition-metal centers and the carbon π-system, facilitating efficient charge delocalization. For example, Zhou *et al.* functionalized graphene oxide sheets with $Ti_3C_2T_x$ MXene *via* Ti–O–C coupling, yielding MXene-modified graphene oxide (MrGO) cross-linked through the conjugated molecule 1-aminopyrene-disuccinimidyl suberate (AD) (Fig. 31).[211] This dual coupling, which combines MXene–carbon covalency and π–π stacking *via* AD, promoted structural densification and interlayer alignment. *In situ* Raman spectroscopy and molecular dynamics simulations confirmed that interfacial orbital hybridization and π–π reinforcement synergistically enhance charge delocalization and lattice coherence, establishing an atomically integrated interface between the inorganic and carbon phases.

Besides covalent anchoring, noncovalent π–π and van der Waals interactions also contribute significantly to interfacial stabilization, particularly in multilayer or hierarchical composites. These weak yet dynamic forces allow interlayer slip and strain accommodation, preserving structural integrity under deformation or electrochemical cycling. From a critical perspective, however, the relative roles of covalent *vs.* noncovalent interactions remain insufficiently quantified. Variations in graphene oxidation level, MXene termination chemistry, and surface functionalization can lead to markedly different bonding motifs. More systematic, termination-controlled synthesis and *operando* spectroscopy are required to establish generalizable bonding–function correlations.

4.3.2. Morphological coupling and restacking inhibition. A persistent structural challenge for 2D MXenes lies in their tendency to restack through van der Waals attraction, blocking active surface sites and hindering mass and charge transport. Incorporation of carbon frameworks effectively mitigates this issue through morphological coupling, in which carbon architectures serve as physical spacers, conductive bridges, and mechanical reinforcements. CNTs and graphene nanosheets intercalate between MXene layers, maintaining open channels for charge and mass transfer. Gao *et al.* introduced a "knotted" CNT architecture, intertwined with Ti_3C_2 MXene (Fig. 32), forming an interpenetrating, multidirectional porous scaffold that prevented lamellar collapse and provided directional electron pathways.[212] The hybrid exhibited high surface accessibility and efficient percolation, demonstrating the decisive role of morphology in dictating transport geometry and interface coupling. In practical synthesis, MXene/CNT hybrids are commonly fabricated by mixing individually dispersed colloids of MXenes and CNTs under ultrasonic agitation or mechanical stirring, followed by vacuum-assisted filtration to yield uniform composite films, as demonstrated by Yan *et al.*[213] This straightforward, scalable approach ensures intimate interfacial contact while minimizing CNT aggregation and MXene restacking. However, such empirical routes often lack atomic-level control, and variations in CNT aspect ratio, MXene flake size, dispersion chemistry, or mixing sequence can lead to inconsistent mesoscale architectures.

Beyond physical mixing, chemical vapor deposition (CVD) offers a powerful route for *in situ* CNT growth on MXene substrates, achieving high yield and structural purity at moderate temperatures. Typically, metal catalyst precursors are preloaded onto layered MXene nanosheets, followed by introduction of a carbonaceous gas (*e.g.*, C_2H_2) to nucleate and grow CNTs directly on the surface. Li *et al.* reported such *in situ*-grown CNT/MXene heterostructures, which exhibit continuous bonding and enhanced electronic coupling due to strong

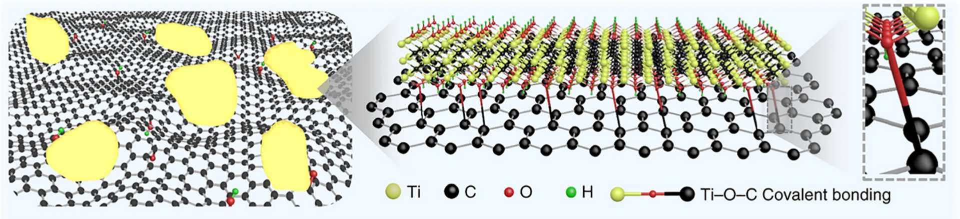

Fig. 31 Schematic model of MXene-GO platelets showing the formation of Ti–O–C covalent bonding. Reproduced from ref. 211 with permission from Springer Nature, copyright 2020.

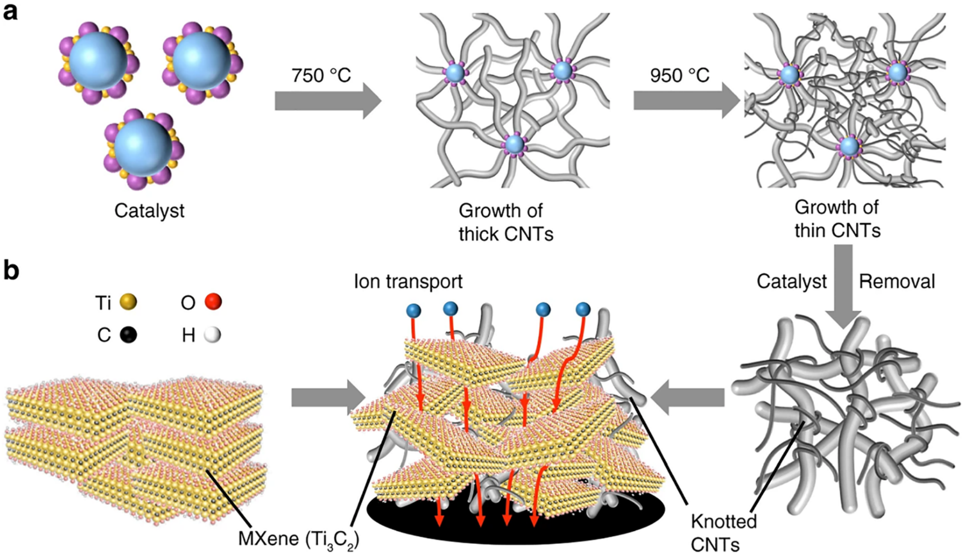

Fig. 32 (a) Schematic of the synthesis process for the knotted CNTs, where thin CNTs were intertwined with thicker CNTs. (b) Schematic of a MXene-knotted CNT composite electrode with reduced horizontal orientation and lower ion transport tortuosity through the bulk of the electrode. Reproduced from ref. 212 with permission from Springer Nature, copyright 2020.

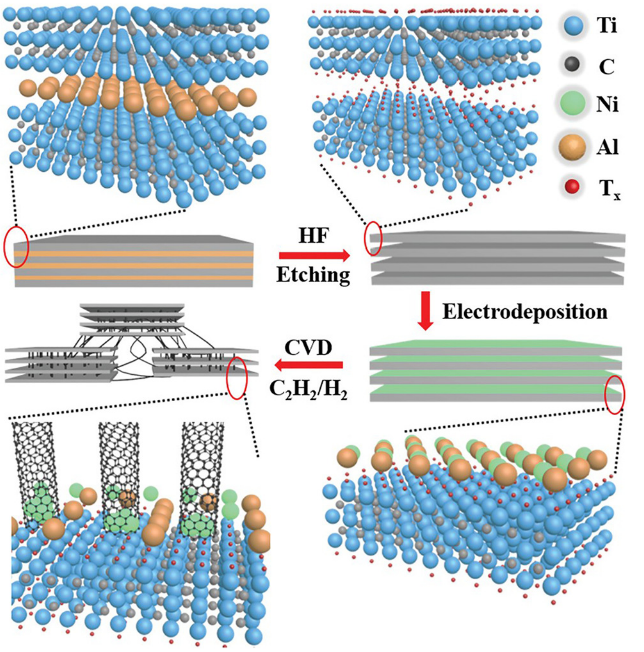

Fig. 33 Schematic illustration for the preparation of MXene and MWCNTs. Reproduced from ref. 214 with permission from Wiley, copyright 2020.

anchoring between CNT bases and MXene layers (Fig. 33).[214] Alternatively, solid-phase synthesis routes employ solid carbon sources premixed with MXenes and metal catalysts (or their precursors), followed by annealing under an inert atmosphere. Wang *et al.* demonstrated this approach in conductive-bridge MXene/CNT arrays, where CNTs grew from within the MXene framework to connect adjacent $Ti_3C_2T_x$ sheets, thereby enhancing both mechanical integrity and charge percolation.[215]

The incorporation of carbon matrices also enhances structural resilience by distributing interfacial stress and minimizing local strain. Unlike rigid inorganic scaffolds, carbon layers can elastically deform while preserving conductivity, enabling the interface to accommodate mechanical or thermal fluctuations without fracture. Such cooperative morphology–interface regulation reinforces the electronic and structural stability of MXenes under long-term operation or environmental exposure. However, morphological coupling strategies often rely on empirical mixing or growth conditions that lack atomic-level determinism. Variations in MXene flake size, CNT aspect ratio, dispersant chemistry, and processing sequence can produce significantly different mesoscale architectures and transport pathways. Moreover, quantitative relationships between morphology, tortuosity, and carrier mobility remain underdeveloped. Future advances require correlating structural metrics with electronic transport through multiscale modeling and *operando* imaging to establish predictive morphology–function rules applicable across MXene/carbon systems.

4.3.3. Electronic coupling and interfacial charge distribution. At the electronic level, MXene/carbon heterostructures exhibit distinctive charge-transfer dynamics arising from interactions between metallic d orbitals of MXenes and delocalized π states in sp^2 carbons. This coupling leads to partial electron redistribution and interfacial polarization, forming dipole layers that modulate local work function and Fermi-level positions. Upon intimate contact, interfacial charge transfer proceeds until Fermi-level equilibration is achieved, generating a built-in electric field across the interface. The magnitude and direction of this field are highly sensitive to both the termination chemistry of MXenes and the electronic structure of the carbon phase. Theoretical calculations reveal that the direction and magnitude of electron flow depend on MXene surface terminations and carbon work function: OH-rich, lower-Φ MXenes typically donate charge to carbon, whereas O-terminated, higher-Φ surfaces accept electrons from the carbon phase. Fluorine terminations, due to their strong electronegativity, suppress interfacial electron delocalization and slightly increase interfacial resistance, underscoring the tunable nature of MXene/carbon contacts at the atomic scale. This termination-dependent equilibration offers a versatile means of tailoring interfacial energy alignment, enabling contacts that range from nearly Ohmic to weakly rectifying and allowing precise control over carrier-transport directionality.

From a quantum-mechanical perspective, orbital hybridization between Ti d-states and the carbon π-network generates hybridized interfacial states near the Fermi level. These hybrid orbitals broaden the DOS and reduce potential barriers, facilitating coherent electron tunneling and enhancing electronic coupling. Time-dependent DFT simulations further indicate that such hybridization accelerates carrier relaxation and suppresses charge trapping, thereby maintaining long-range electronic continuity. Spectroscopic analyses such as XPS, ultraviolet photoelectron spectroscopy (UPS), and KPFM confirm the existence of hybridized interfacial states and localized surface-potential contrasts corresponding to interfacial dipoles. Ultrafast transient absorption spectroscopy further provides direct dynamic evidence for sub-picosecond charge equilibration across MXene/carbon interfaces, reinforcing their role as efficient charge-mediating junctions. These hybridized states smooth potential barriers, maintain low contact resistance, and ensure stable polarization under bias. Collectively, MXene/carbon interfaces act as electronically coherent junctions that bridge microscopic orbital hybridization with macroscopic charge-transport behaviour. However, quantitative determination of charge-transfer magnitude and dipole strength remains difficult, as interfacial electronic behavior is highly sensitive to termination chemistry, flake oxidation, and carbon defect levels, leading to notable variability across studies. Most available measurements are *ex situ*, whereas interfacial polarization can evolve dynamically under electrical, thermal, or electrochemical stimuli. These limitations hinder the establishment of universal structure–property relationships. Advancing the field will require *operando* electronic–structural correlation using ultrafast spectroscopy and atomic-resolution probes to capture how terminations and carbon hybridization jointly modulate the interfacial electronic landscape under realistic working conditions.

4.3.4. Structural robustness and interfacial stability. The chemical inertness and oxidation resistance of carbon materials impart critical stability advantages to MXene interfaces. Graphitic encapsulation or coating acts as a diffusion barrier that suppresses oxidation, hydrolysis, and termination loss. By impeding oxygen and moisture ingress, such carbon layers preserve the stoichiometry and surface terminations of MXenes, maintaining their intrinsic metallic conductivity. The carbon framework also relieves interfacial strain and prevents crack propagation during cycling or thermal stress, while its high thermal conductivity dissipates localized heat accumulation that could otherwise induce phase transformation or delamination.

Beyond passivation, the carbon network serves as a mechanical and electrical backbone that redistributes stress and current throughout the composite. In graphene- or CNT-based hybrids, the sp^2 lattice can flex and stretch elastically under deformation, maintaining percolative connectivity between MXene layers even at high strain. This stress-transfer mechanism mitigates fatigue and delamination during prolonged electrochemical or mechanical operation, thereby enhancing long-term reliability.

Functionalization of carbon matrices (for instance, through oxygen or nitrogen dopants) enables fine control over the hydrophilic–hydrophobic balance, optimizing adhesion and charge transfer. Nitrogen doping introduces additional lone-pair states that strengthen Ti–N or Ti–O–C coordination, while oxygenated groups promote chemical bonding and interfacial wettability. Together, these modifications stabilize interfacial dipoles and suppress charge accumulation or chemical heterogeneity under bias.

At a larger scale, hierarchical carbon frameworks bridge adjacent MXene sheets, forming interconnected conductive networks that maintain electrical continuity even under severe deformation. The combined effects of chemical shielding, mechanical reinforcement, and thermal dissipation transform MXene/carbon heterostructures into robust hybrid architectures with long-term operational stability and environmental resilience. From the standpoint of interface science, such hybridization exemplifies how chemical protection and electronic coupling can coexist to yield structures that are simultaneously conductive, flexible, and durable.

Despite these advantages, interfacial stability remains difficult to generalize, as carbon coatings vary widely in thickness, defect density, and functional-group distribution. These differences lead to inconsistent oxidation resistance and mechanical resilience across studies. Moreover, many reported systems rely on *ex situ* stability tests, whereas real interfaces undergo dynamic restructuring under electrical bias or thermal gradients. A more reliable understanding of stability will require correlating *operando* chemical evolution with local bonding environments and electronic transport, enabling predictive rather than empirical design of robust MXene/carbon interfaces.

4.3.5. Challenges and perspectives. Although MXene/carbon interface engineering has advanced rapidly, achieving rational, reproducible design at the atomic level remains challenging. The dominance of Ti–O–C covalency, π–π stacking, or electrostatic adsorption varies sensitively with processing conditions, hindering reproducible atomic-scale control. Quantitative determination of charge-transfer magnitude and dipole strength remains difficult due to overlapping electronic densities. Moreover, the long-term chemical and structural evolution of MXene/carbon contacts remains insufficiently understood, particularly regarding slow MXene oxidation, interfacial bond rearrangement, and carbon-induced termination migration during cycling. Progress will depend on integrating surface-specific spectroscopies (*e.g.*, UPS, NEXAFS) with ultrafast probes capable of capturing transient interfacial states. A further complication is that existing characterization tools often blur the distinction between intrinsic interfacial bonding and artefacts arising from beam-induced damage, surface adsorbates, or post-processing oxidation, which limits reliable correlation between interface structure and electronic behavior. Complementary first-principles modelling can correlate local bonding geometry and termination chemistry with electronic delocalization. On the synthetic side, atomic-layer deposition, molecular cross-linking, and confined-growth techniques offer promising routes to achieve deterministic control over interface thickness, orientation, and composition.

In conclusion, MXene/carbon heterostructures embody a balanced interface paradigm where electronic continuity, structural adaptability, and chemical stability coexist. A deeper mechanistic understanding of their coupling will enable the rational design of MXene-based hybrids combining atomic precision with macroscopic resilience, an essential goal for next-generation heterostructure engineering.

4.4. MXene/polymer heterostructure interfaces

MXene/polymer heterostructures represent a unique class of soft–hard hybrids that bridge the atomic precision of inorganic 2D layers with the structural versatility of organic macromolecules. Unlike metallic or ceramic systems, polymers offer molecularly tunable frameworks capable of regulating interfacial charge distribution, hydrophilicity, and mechanical compliance. When integrated with MXenes, whose surfaces are densely decorated with reactive terminations (–O, –OH, –F), the resulting interfaces exhibit multiple forms of coupling, including hydrogen bonding, electrostatic interaction, and covalent linkage. These couplings stabilize the lamellar MXene structure while tuning its electronic configuration, enabling precise control over charge transport, polarization, and molecular-scale adaptability.

4.4.1. Interfacial coupling mechanisms and chemical architectures. Among all MXene-based interfaces, MXene/polymer systems uniquely integrate soft-matter adaptability with 2D inorganic precision. Interfacial chemistry between MXenes and polymers is dictated by the compatibility between surface terminations and polymer functional groups. Hydrogen bonding dominates: surface –OH or –O groups form directional hydrogen bonds with polymeric carboxyl, hydroxyl, or amide moieties, establishing dynamic yet robust networks. Electrostatic interactions further enhance adhesion when positively charged polyelectrolytes bind to negatively charged MXene surfaces, thereby producing self-assembled multilayers.

Beyond noncovalent interactions, covalent pathways such as carbodiimide coupling, silane grafting onto surface hydroxyls, borate-ester crosslinking with diols, or surface-initiated controlled radical polymerization yield chemically robust and solvent–resistant interfaces. Selecting polymers from distinct categories including matrices (polyvinyl alcohol, polyethylene oxide), ionomers (Nafion, sulfonated polyether ether ketone), conductive polymers (polyaniline, polypyrrole, poly(3,4-ethylenedioxythiophene)), and polyelectrolytes (polydiallyldimethylammonium chloride, polyethyleneimine), provides orthogonal handles to tune interfacial charge, stiffness, and transport properties. These diverse coupling modes create hierarchical architectures where polymer chains intercalate, wrap, or graft onto MXene layers, forming continuous percolation networks that couple chemical bonding with mechanical reinforcement. However, establishing quantitative structure–property relationships remains nontrivial, as the coexistence of hydrogen bonding, electrostatic attraction, and covalent grafting complicates unambiguous assignment of bonding motifs. Additionally, polymer-induced rearrangement of MXene terminations can obscure whether observed electronic changes originate from intrinsic MXene chemistry or polymer-driven reorganization, highlighting the need for clearer bonding descriptors and cross-validated spectroscopic interpretation.

4.4.2. Molecular assembly and structural engineering. Two principal fabrication routes dominate MXene/polymer construction: direct physical mixing and *in situ* polymerization. In physical mixing, polymer molecules intercalate between MXene sheets through hydrogen bonding and electrostatic forces, effectively expanding interlayer spacing, suppressing restacking, and improving ion accessibility. For example, Ling *et al.* combined $Ti_3C_2T_x$ MXene with positively charged polydiallyldimethylammonium chloride (PDDA) and neutral polyvinyl alcohol (PVA) to produce flexible, conductive films (2.2×10^4 S m^{-1}) with tensile strengths far exceeding those of pure $Ti_3C_2T_x$ or PVA (Fig. 34).[12] The polymer intercalation improves mechanical compliance and ion transport, illustrating how confined polymer–MXene interactions dictate hybrid behaviors.

In *in situ* polymerization, monomers first anchor to MXene surfaces *via* hydrogen bonding or electrostatic attraction, then polymerize to form conformal coatings. Lu *et al.* synthesized PANI@TiO_2/$Ti_3C_2T_x$ heterostructures by polymerizing aniline monomers directly on $Ti_3C_2T_x$ nanosheets (Fig. 35).[216] The resulting framework, incorporating polyaniline and TiO_2, exhibited extended ion-transport pathways and approximately doubled areal capacitance compared to pristine MXene. These examples demonstrate that molecular-level assembly, rather than bulk blending, governs coherent polymer–MXene integration while enabling tunable electronic continuity.

However, polymerization on MXene surfaces may introduce unintended side effects, including termination displacement and partial oxidation. These changes are rarely quantified yet can substantially alter interfacial chemistry, underscoring the importance of characterizing polymerization-driven modifications to avoid misinterpreting composite performance.

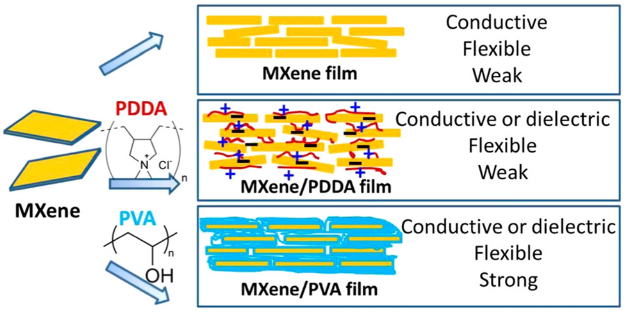

Fig. 34 A schematic illustration of MXene-based functional films with adjustable properties. Reproduced from ref. 12 with permission from the National Academy of Sciences, copyright 2014.

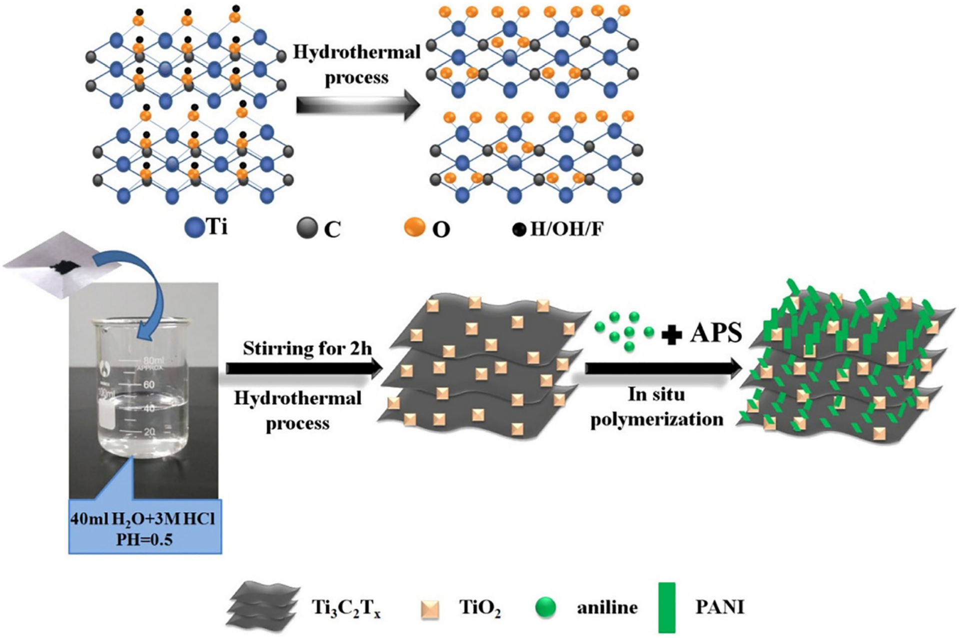

Fig. 35 Schematic illustration of *in situ* oxidation of $Ti_3C_2T_x$ and the main preparation process of PANI@TiO_2/$Ti_3C_2T_x$ ternary composite. Reproduced from ref. 216 with permission from Elsevier, copyright 2017.

4.4.3. Electronic interaction and interfacial polarization. At the electronic level, MXene/polymer interfaces act as hybrid dielectric–metal or semiconductor–dielectric junctions, where localized dipoles, charge redistribution, and dielectric mismatch dictate electronic behavior. Electron-rich terminations on MXenes can withdraw or donate charge to polymer chains, thereby inducing polarization and dipole formation that reshape local electrostatic potentials. This polarization modulates Fermi-level alignment, adjusts band offsets, and tunes charge-injection barriers, creating effects analogous to semiconductor heterojunctions but dynamically adjustable through polymer composition and chain mobility.

DFT simulations show that hydrogen-bonded or covalently linked interfaces introduce shallow trap states and broadened DOS distributions near the Fermi level, facilitating charge delocalization while maintaining dielectric insulation. In conductive polymers such as polyaniline or poly(3,4-ethylenedioxythiophene), π-conjugated orbitals hybridize with MXene d-states to form interfacial charge-transfer complexes that lower tunneling barriers and enhance carrier density. Experimental XPS, UPS, and KPFM analyses reveal core-level shifts and surface-potential changes after polymer integration, confirming interfacial charge transfer and dipole orientation. Under electric or optical excitation, these dipolar junctions exhibit nonlinear polarization and field-enhanced mobility, highlighting MXene/polymer interfaces as actively tunable dielectric layers. Nevertheless, quantifying interfacial polarization remains difficult, because polymer dielectric relaxation, hydration state variability, and chain mobility lead to transient or environment-dependent behaviors rather than intrinsic interfacial properties. Temperature- and humidity-controlled *operando* measurements will be necessary to establish reliable models for device-level operation.

4.4.4. Structural stability, mechanical compliance, and environmental adaptability. Polymer incorporation provides multidimensional stabilization extending beyond simple reinforcement. On the molecular scale, polymer chains dissipate stress *via* segmental motions and reversible bond stretching, enabling flexibility without fracture. Encapsulating MXenes in polymer matrices forms protective barriers that suppress oxidation, hydrolysis, and termination loss. The viscoelasticity of polymer phases mitigates stress concentration and prevents delamination during bending or redox cycling. Covalent and hydrogen-bonded linkages preserve adhesion, while mobile segments accommodate strain gradients, maintaining continuous charge pathways.

From a chemical perspective, the hydrophilic–hydrophobic balance, which can be tuned by introducing oxygenated, fluorinated, or nitrogen-containing substituents, allows stable operation across diverse solvents, pH ranges, and temperatures. Incorporating ion-conducting or proton-conducting polymers such as Nafion or ether-containing chains further stabilizes interfacial hydration layers and optimizes ionic mobility. Together, these mechanisms render MXene/polymer heterostructures structurally adaptive, environmentally tolerant, and mechanically robust, attributes essential for next-generation flexible and wearable platforms where conductivity, elasticity, and stability must coexist. However, long-term stability remains challenging. Polymer relaxation, moisture uptake, plasticization, and chain rearrangement can progressively alter interfacial dipoles and MXene termination chemistry, leading to performance drift that is seldom monitored. Accelerated aging tests and *operando* chemical mapping will be essential to assess true reliability.

4.4.5. Challenges and perspectives. While MXene/polymer heterostructures display exceptional versatility, several unresolved issues still limit atomic-level control and predictive design. (i) The coexistence of hydrogen bonding, electrostatic attraction, and covalent grafting complicates quantitative correlations between interfacial chemistry and charge or ion transport. Developing unified descriptors such as interfacial dipole strength or bond-energy density will be crucial for modeling. (ii) Buried interfaces are difficult to characterize because polymer layers obscure MXene surfaces, necessitating advanced *operando* probes such as vibrational sum-frequency generation spectroscopy, NEXAFS, and time-resolved electron microscopy. (iii) Functional polymer design remains underexplored. Most current systems rely on stabilizing or electronically inert polymers, while electronically active polymers capable of photoinduced charge transfer, ion conduction, or redox participation could fundamentally expand interfacial functionality. (iv) Multiscale modeling that couples molecular dynamics with first-principles simulations can connect polymer chain dynamics with MXene electronic structure and guide deterministic interface construction. (v) Stability and scalability remain limiting factors, as polymer relaxation or moisture absorption may gradually modify interfacial dipoles and morphology. Developing accelerated aging tests and self-healing or re-crosslinkable polymers will be important for practical deployment.

Moving ahead, the convergence of molecular design, *operando* characterization, and data-driven modeling will enable programmable MXene/polymer interfaces with tunable bonding chemistry, dielectric response, and mechanical resilience. These materials are expected to evolve from passive stabilizers into active interfacial regulators capable of dynamically mediating electron, ion, and energy transport. Within this broader framework, MXene/polymer heterostructures exemplify adaptive interface engineering, uniting inorganic precision with organic versatility and expanding MXene science toward flexible, durable, and reconfigurable 2D hybrid systems.

4.5. Concluding remarks and outlook

The evolution of MXene research from surface modification to interfacial design marks a conceptual transition from tailoring individual layers to architecting cooperative systems. Interface engineering transforms MXenes from passive conductive fillers into active mediators that direct charge transport, chemical reactivity, and structural dynamics across dissimilar phases. Rather than focusing on specific heterostructure types, the essence of this chapter lies in revealing how MXenes redefine interfacial chemistry itself. By merging metallic conductivity with tunable surface polarity and chemical adaptability, MXenes provide a universal ''coupling language'' that bridges metals, semiconductors, carbons, and polymers within a unified design framework.

At the conceptual level, MXene interfaces illustrate a hierarchy of interactions that transcend simple material pairing. Electronic equilibration establishes internal fields and polarization gradients that guide carrier motion; lattice coherence and strain relaxation translate these electronic effects into structural stability; and interfacial chemistry provides self-passivating mechanisms that maintain order under stress. Across metallic, semiconducting, carbonaceous, and polymeric counterparts, the MXene phase acts as a dynamic regulator that continually adjusts bonding, charge density, and local potential to preserve function. This adaptability, rooted in the interplay between delocalized d-orbitals and chemically active terminations, distinguishes MXenes from conventional 2D materials whose interfaces are more electronically rigid or chemically inert.

Beyond static understanding, a central message emerging from this chapter is the notion of ''adaptive interface coupling''. MXene heterostructures are not fixed junctions but self-equilibrating systems capable of redistributing charge, reorganizing bonds, and even reconstructing local lattices to minimize interfacial energy. This dynamic responsiveness blurs the boundary between interface and bulk, suggesting that functionality arises not from isolated layers but from the continual rebalancing of their mutual interactions. Such a perspective reframes MXene-based heterostructures as evolving interfaces that co-adapt with external stimuli, illumination, potential, or stress, reflecting a built-in feedback loop between structure and function.

In the future, the frontier of MXene interface science will shift from empirical synthesis toward predictive and programmable control. Achieving this goal demands atomic-level understanding of termination chemistry, real-time mapping of buried charge redistribution, and multiscale models that couple quantum electronic structure with mesoscale transport. Emerging *in situ* and ultrafast techniques such as *operando* X-ray and electron spectroscopy, time-resolved optical probes, and machine-learning-assisted simulations will enable direct observation of interfacial dynamics and guide rational interface design. At the same time, functional diversification through hybridization with molecular, polymeric, or bio-derived frameworks could unlock reconfigurable, stimuli-responsive interfaces capable of adapting to complex operational environments. However, such opportunities also highlight the need for standardized benchmark systems and reproducible synthesis protocols, which are currently lacking across the field.

Despite these opportunities, a major unresolved challenge is the absence of a unified framework that quantitatively links termination chemistry with interfacial electronic structure. Most reported heterostructures rely on inferred rather than directly verified interfacial configurations, limiting predictive accuracy and complicating cross-study comparisons. *Operando*-validated structure–property relationships are essential for moving from descriptive reports to mechanistically grounded design rules, particularly in systems where termination rearrangement, partial oxidation, or dynamic bonding blur the boundaries between intrinsic and extrinsic interfacial states.

In summary, the study of MXene heterostructure interfaces reveals a broader paradigm for 2D materials science: that the interface is not merely a boundary but an active state of matter. By mastering the coupling between electronic, structural, and chemical degrees of freedom, MXene-based hybrids can evolve into intelligent, self-stabilizing materials whose performance emerges from the very interactions that connect their components. This integrative perspective, where inorganic precision meets chemical adaptability, defines the next frontier of interface engineering and positions MXenes at the core of a new generation of multifunctional, resilient, and dynamically tunable hybrid systems. In this light, MXenes stand not merely as materials, but as a conceptual framework for understanding and designing adaptive interfaces across the entire spectrum of 2D materials science.

5. MXene in catalysis: applications and mechanistic insights

The surface modification strategies and interfacial coupling mechanisms described in the previous chapters show that MXenes possess tunable Fermi-level positions, flexible surface terminations, and dynamic interfacial polarization, attributes that collectively modulate charge transfer, adsorption energetics, and reaction pathways. Building on these insights, this chapter extends the discussion from structural and electronic design principles to their catalytic implications, elucidating how atomic- and interfacial-level tunability dictates activity, selectivity, and durability across diverse reaction environments. In particular, MXenes' ability to regulate local electronic density, interfacial electric fields, and adsorption energetics positions them as a versatile platform for heterogeneous catalysis driven by rational interface engineering.

The interfacial and electronic characteristics enable MXenes to assume multiple catalytic roles. When functioning as active catalytic centers, MXenes such as Ti_3C_2 and Mo_2C exhibit d-orbital characteristics and surface chemisorption properties analogous to those of noble metals, enabling efficient bond activation and intermediate stabilization. Through surface engineering, including terminal group modulation, heteroatom doping, and defect construction, their local electronic structure and reaction kinetics can be finely optimized. Beyond serving as intrinsic catalysts, MXenes also function as conductive scaffolds and cocatalysts, facilitating uniform dispersion and robust anchoring of metals, metal compounds, or molecular catalysts. The formation of MXene-based heterostructures further introduces interfacial electric fields, orbital hybridization, and charge redistribution, which collectively accelerate electron migration and reshape reaction pathways.

By bridging metallic conductivity with catalytic reactivity, MXenes provide a cohesive platform for heterogeneous catalysis. Their dual role as both electron mediators and chemically adaptive supports enables synergistic integration across a wide range of reaction systems, from hydrogen and oxygen electrocatalysis to photocatalytic CO_2 conversion and selective organic transformations. In this sense, the catalytic behavior of MXenes emerges not as an isolated property but as a manifestation of the interface-engineered electronic architecture established through surface and heterostructural design.

Accordingly, this chapter systematically delineates the catalytic functions of MXenes and the underlying mechanistic principles (Fig. 36). Section 5.1 examines MXenes as active catalytic centers, focusing on intrinsic surface reactivity, termination effects, and structure–activity correlations; Section 5.2 discusses their role as conductive scaffolds and electron mediators in composite catalysts, analyzing charge-transfer dynamics and their influence on overall catalytic processes; Section 5.3 highlights their function as structural stabilizers that preserve catalytic frameworks under operating conditions; Section 5.4 explores multi-energy synergistic catalysis, emphasizing MXene-enabled coupling

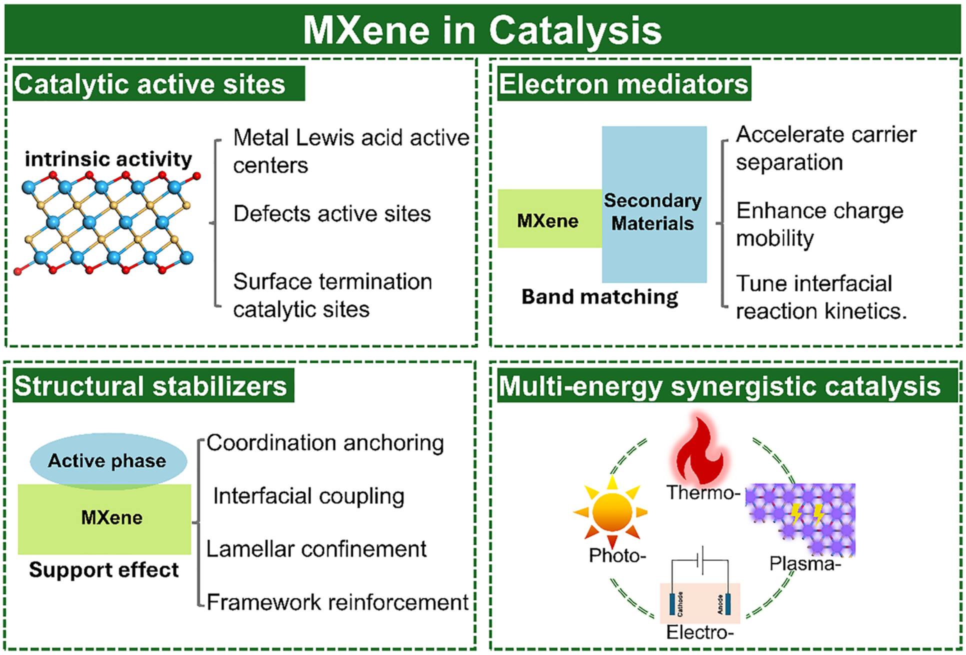

Fig. 36 Conceptual framework illustrating the multifaceted catalytic roles of MXenes.

between light, heat, and electrochemical driving forces; and Section 5.5 summarizes the unified mechanistic frameworks that link interfacial electronic structure with catalytic function. Collectively, these discussions establish MXenes as an archetype of surface- and interface-governed catalysis, in which the interplay between surface chemistry and interfacial electronic structure enables atomic-level precision, tunable reactivity, and dynamic adaptability for highly efficient and sustainable catalytic systems.

5.1. MXene as active catalytic centers

MXenes represent a distinctive class of catalytic materials whose activity originates from the synergy among their transition-metal d states, surface terminations, and defect structures. Unlike conventional bulk carbides or nitrides, MXenes expose a high density of accessible metal sites and offer tunable surface chemistry within a 2D framework. Their metallic conductivity ensures efficient charge transport, while abundant –O, –OH, –F, –Cl, –S, and –N terminations modulate local electron density and adsorption energetics. This unique duality, in which metallic conduction is coupled with oxide-like chemical versatility, enables MXenes to operate simultaneously as electron mediators, adsorption platforms, and reactive centers, bridging the gap between metallic catalysts and heterogeneous supports. This section discusses the intrinsic origins of MXene reactivity, the electronic and chemical strategies for tuning their surface states, and the mechanistic evidence that connects structure and activity across different catalytic modalities.

5.1.1. Origin of intrinsic activity: metal centers, defects, and terminations. The catalytic behavior of MXenes arises from their exposed transition-metal centers, defect structures, and surface terminations, which together determine the electronic distribution and local coordination environment. In typical $M_{n+1}X_n$ MXenes (M = Ti, Nb, Mo, V; X = C or N), the exposed transition metals provide partially filled d orbitals that can serve as Lewis acid centers or redox-active sites. These atoms are capable of forming σ- or π-complexes with reactant molecules, enabling the activation of bonds such as H–H, C–H, N≡N, or C=O through back-donation or polarization of antibonding orbitals. The subsurface X layer modulates the d-band center of the metal atoms, which directly affects adsorption strength and reactivity.

Surface terminations introduce additional acidity/basicity and polarization, shaping the adsorption of polar molecules and stabilizing key intermediates. Hydroxyl (–OH) and oxo (–O) terminations can mediate proton-coupled electron transfer, while electronegative halogens moderate binding strength. These effects complement the electronic contributions of metal centers and defects, creating a spectrum of active sites that bridge metallic and oxide-like behavior.[5,217] Lattice defects and step edges further generate under-coordinated metal atoms that enhance adsorption of polar molecules (CO_2, H_2O, NH_3) or activate nonpolar bonds (C–H, N≡N).[218] However, the density and evolution of these sites under *operando* conditions remain difficult to quantify, limiting the construction of rigorous structure–activity maps.

5.1.2. Electronic and chemical modulation of active sites. The surface chemistry of MXenes can be deliberately engineered to tune catalytic behavior and reaction selectivity. Termination modulation directly reconfigures local electron density and intermediate binding energies, making it one of the most effective approaches for tailoring reactivity. Oxygen-rich surfaces strengthen adsorption of *H, *OH, and *CO_2, whereas –F groups, owing to their strong electronegativity, weaken binding and suppress overactivation, thereby improving selectivity. A compelling example of termination control was demonstrated by Zhou *et al.* in CO_2 hydrogenation over Mo_2CT_x (T = O, OH, F) and termination-free 2D-Mo_2C.[155] A 2D, multilayer Mo_2C catalyst without surface termination groups (T_x-free) was prepared by reductive de-functionalization of Mo_2CT_x MXene in pure hydrogen at 500 °C, avoiding the formation of a three-dimensional carbide structure. The activity and product selectivity in CO_2 hydrogenation are determined by the surface coverage of T_x groups in Mo_2CT_x, which can be tuned through hydrogen pretreatment. Compared with T_x-containing Mo_2CT_x, β-Mo_2C, and the industrial Cu–ZnO–Al_2O_3 catalyst, T_x-free 2D-Mo_2C exhibits higher CO yield (close to the thermodynamic equilibrium) and outstanding stability (> 100 h TOS) (Fig. 37). Its purely Mo-terminated surface has about eight times the CO chemisorption capacity of β-Mo_2C, leading to a significant increase in CO_2 hydrogenation activity. In addition, 2D-Mo_2C is highly active for CO_2 dissociation and can be applied in CO_2–H_2 chemical looping processes, showing strong potential as an efficient and stable catalyst for CO_2 hydrogenation.

Heteroatom substitution further provides a route for tuning the d-band center and local charge environment. Introducing transition-metal dopants (*e.g.*, Co, Fe, Ni) or nonmetals (*e.g.*, N, S, P) adjusts electron distribution and creates isolated atomic sites with optimized adsorption energetics, while preserving the metallic conductivity of the host. Defect engineering further diversifies the electronic landscape, enabling cooperative activation of electrophilic and nucleophilic species. For example, Nb_2C exhibits superior turnover frequencies in aldol condensations and oxidative amine couplings compared to conventional acid–base catalysts, arising from adjacent oxygen vacancies and termination groups that cooperatively activate both electrophilic and nucleophilic species.[219,220] Although diverse modification strategies exist, systematic high-throughput exploration of termination–dopant–defect combinations remains limited, and most studies examine only isolated variables. Exploring broader compositional space will be crucial for uncovering optimal configurations for selective catalysis.

5.1.3. Structure–reactivity correlations and catalytic evidence. The intrinsic reactivity of MXenes has been confirmed across electro-, photo-, and thermocatalytic systems, where theoretical predictions, *in situ* characterization, and catalytic benchmarks jointly reveal the structure–activity relationships that govern their performance.

In electrocatalysis, the metallic conductivity and adjustable hydrogen adsorption energetics of MXenes make them effective non-noble catalysts.[221,222] DFT and surface Pourbaix diagram

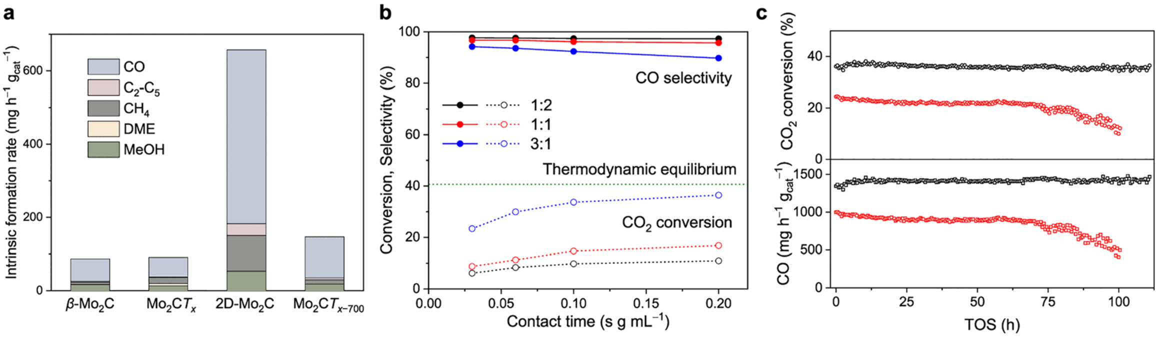

Fig. 37 (a) Intrinsic formation rates obtained after H_2 pretreatment of Mo_2CT_x at different temperatures. Reaction conditions: 230 °C, 25 bar, $H_2/CO_2/N_2$ = 3/1/1. (b) Hydrogenation of CO_2 at 430 °C and 1 bar with 2D-Mo_2C under variable $H_2 : CO_2$ ratios. (c) Stability test of 2D-Mo_2C (black) and industrial Cu–ZnO–Al_2O_3 (red) at *ca.* 100 h of TOS (430 °C, 1 bar, $H_2/CO_2/N_2$ = 3/1/1, contact time 0.2 s g_{cat} mL^{-1}). Reproduced from ref. 155 with permission from Springer Nature, copyright 2021.

analyses show that O/OH-terminated Ti_2C, V_2C, and Ti_3C_2 possess ΔG_{H^*} values close to 0 eV, ideal for the hydrogen evolution reaction (HER).[124,223] These predictions were experimentally validated by Seh *et al.*, who observed that Mo_2CT_x exhibits high activity and stability under acidic conditions, with hydrogen evolution occurring predominantly on basal planes rather than edge sites, a behavior that contrasts with conventional transition-metal dichalcogenides.[124] The O/OH terminations provide optimal proton-binding strength and maintain low charge-transfer resistance, enabling exchange current densities comparable to Pt-based systems. Beyond intrinsic activity, compositional tuning enhances both kinetics and stability. Co-doped Mo_2CT_x, developed by Kuznetsov *et al.*, exhibited substantially enhanced HER performance compared with pristine Mo_2CT_x, as evidenced by a fivefold increase in current density and a substantially reduced overpotential (Fig. 38a).[174] This improvement originates from electronic modulation induced by atomic Co substitution at Mo sites, which optimizes the hydrogen adsorption free energy ($\Delta G_H \approx 0.40$ eV *vs.* 0.61 eV for undoped Mo_2CO_2) and lowers the reaction barrier (Fig. 38b). DFT analyses revealed that Co incorporation perturbs the local electronic environment of neighboring O-terminated sites through d–p orbital hybridization, thereby strengthening interfacial coupling and accelerating the Volmer–Heyrovsky kinetics. Fe-doped Mo_2CT_x, on the other hand, selectively catalyzed the two-electron oxygen reduction reaction (ORR) pathway to H_2O_2 with nearly 100% selectivity, accompanied by a gradual *in situ* transformation into iron oxyhydroxide/graphitic carbon hybrids during operation.[175] This structural evolution highlights the dynamic adaptability of MXenes, which can reconstruct into catalytically competent oxyhydroxide phases under electrochemical conditions (Fig. 38c). Extending beyond HER and ORR, MXenes modified with Cu exhibit dopant-dependent selectivity in CO_2 reduction reaction (CO_2RR): Cu single atoms can effectively reduce the energy barrier of the rate-determining step (HCOOH* → CHO* intermediate adsorption) in the reaction path, and preferentially select the low-energy downhill pathway, thereby significantly promoting the electroreduction of CO_2 to generate CH_3OH (Fig. 38d).[224] These examples establish a consistent mechanistic framework linking surface terminations, dopant-induced d-band tuning, and reaction selectivity across diverse electrocatalytic processes.

In photocatalysis, MXenes can transition from metallic to semiconducting behavior through surface or size engineering, allowing them to act as light-harvesting catalysts. Theoretical simulations of M_2CO_2 (M = Ti, Zr, Hf) predict moderate band gaps (0.9–1.8 eV) and favorable band-edge positions for water splitting and CO_2 reduction, with oxygen termination stabilizing photoactive configurations.[225] Beyond these oxygen-terminated systems, Balcı *et al.* achieved band-gap modulation by substituting carbon atoms in Sc_2CF_2 with nonmetallic elements (Si, Ge, Sn, F, S, N, B, and B + N).[226] Among these, doping with Si, Ge, Sn, B, and B + N preserved semiconducting behavior and tuned the gap within 0.24–0.55 eV, whereas F, S, N dopants and single carbon vacancies induced metallic states. Energetic analyses confirmed that such substitutions are thermodynamically feasible during MAX-phase synthesis, offering a practical route for designing MXenes with multifunctional electronic and photocatalytic applications. Complementary first-principles calculations by Guo *et al.* identified Zr_2CO_2 and Hf_2CO_2 as highly efficient single-component photocatalysts whose band edges align with the water-splitting redox potentials.[227] Both materials exhibit strong light absorption in the 300–500 nm range and highly anisotropic carrier mobility that facilitates charge separation. Phonon and molecular dynamics simulations confirmed structural stability in both crystal lattices and aqueous environments, while adsorption and dissociation energy profiles revealed favorable H_2 generation pathways. These computational insights establish theoretical design guidelines for enhancing MXene photocatalysts through surface functionalization, heteroatom doping, and electronic structure regulation.

Experimental validation followed these predictions. Xie *et al.* confirmed that halogen modification can effectively tune MXene band structure and carrier dynamics.[228] Iodine-functionalized Ti_3C_2–I_2, synthesized *via* a microwave molten-salt route, exhibited an upward Fermi-level shift and a reduced surface work function, which enhanced charge separation and prolonged carrier lifetime (Fig. 39a). Under visible-light irradiation, Ti_3C_2–I_2 achieved 85.5% removal of gaseous elemental mercury, far surpassing unmodified MXenes. At the quantum

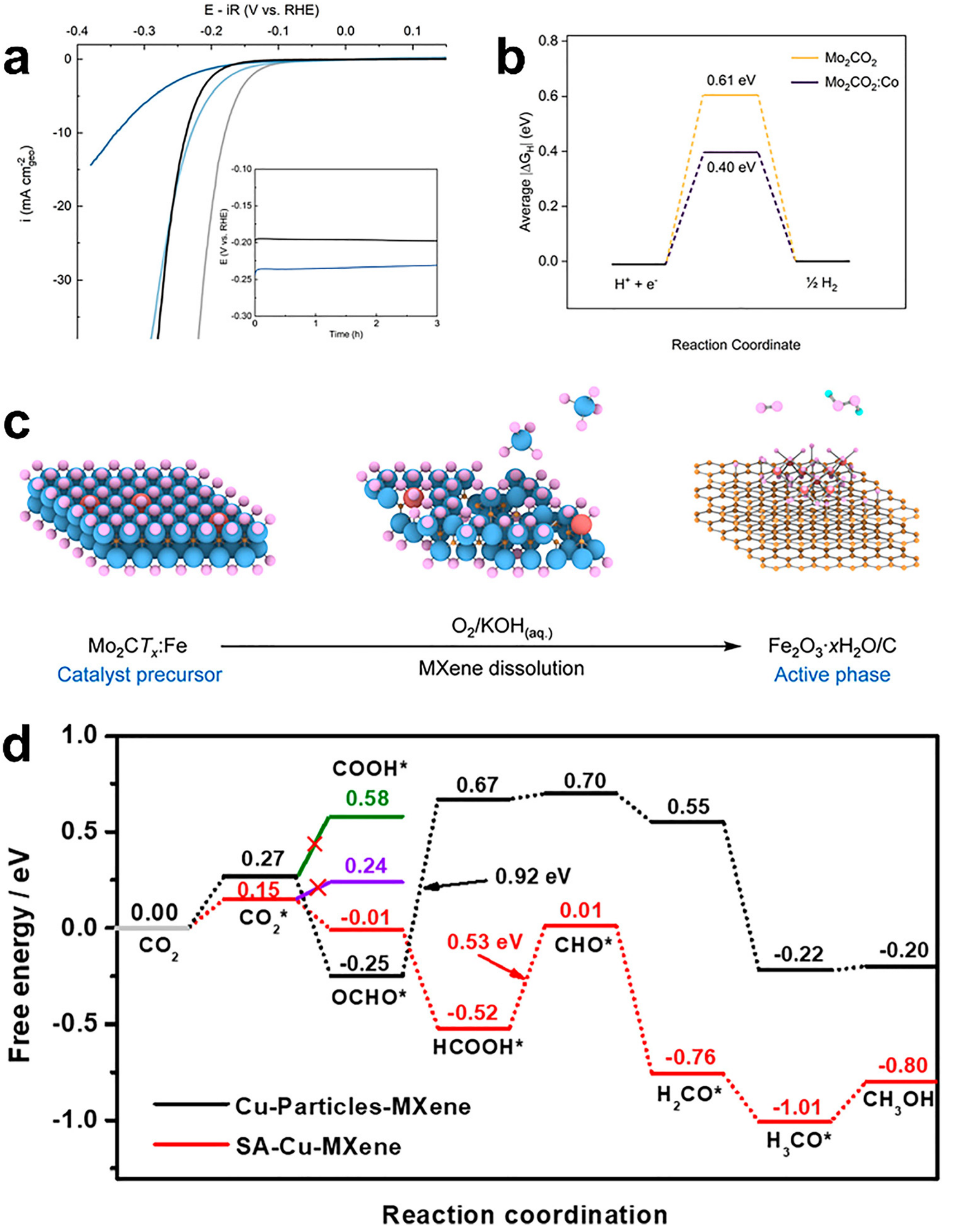

Fig. 38 (a) Background-corrected polarization curves recorded for Mo_2CT_x:Co and Mo_2CT_x using a scan rate of 10 mV s^{-1}. Inset shows chronopotentiometry data for both catalysts at 0.1 mg cm^{-2} loading held at 1 mA cm_{geo}^{-2}. (b) Reaction coordinate for the hydrogen evolution on Mo_2CO_2 and Mo_2CO_2:Co with average $|\Delta G_H|$ values computed for the hydrogen adsorption. (c) Dynamic transformation of MXenes into catalytically competent oxyhydroxide phases under electrochemical conditions. (d) Free energy diagram of CO_2 to CH_3OH on Cu–O_3 structure. Reproduced from (a) and (b) ref. 174, (c) ref. 175, and (d) ref. 224 with permission from American Chemical Society, copyright 2019 and 2021.

scale, Ramírez *et al.* prepared oxygen-terminated MXene quantum dots (QDs) with average sizes of ∼5 nm and yields exceeding 20% *via* laser ablation, avoiding HF use. The obtained MXene QDs demonstrated pronounced semiconductor properties, characterized by an opened band gap. (Fig. 39b).[84,85] These QDs displayed visible-light H_2 evolution rates of 2.02 mmol g^{-1} h^{-1} without photosensitizers and efficiently catalyzed CO_2 hydrogenation to CO and CH_4, with the activity order $Ti_3C_2 > Nb_2C > Ti_2C > V_2C$. Their performance correlated with calculated density of states near the Fermi level and surface oxygen coverage, confirming that termination chemistry and quantum confinement jointly dictate photocarrier dynamics and reaction efficiency.

In thermocatalysis, MXenes exhibit metallic-like activity for dehydrogenation, reforming, and nitrogen fixation reactions, where d-orbital alignment and termination chemistry govern bond activation energetics. Diao *et al.* demonstrated that Ti_2CT_x catalyzes ethylbenzene dehydrogenation with 97.5% selectivity and 92 μmol m^{-2} h^{-1} activity over 40 h, outperforming nanocarbon catalysts.[39] Experimental and computational

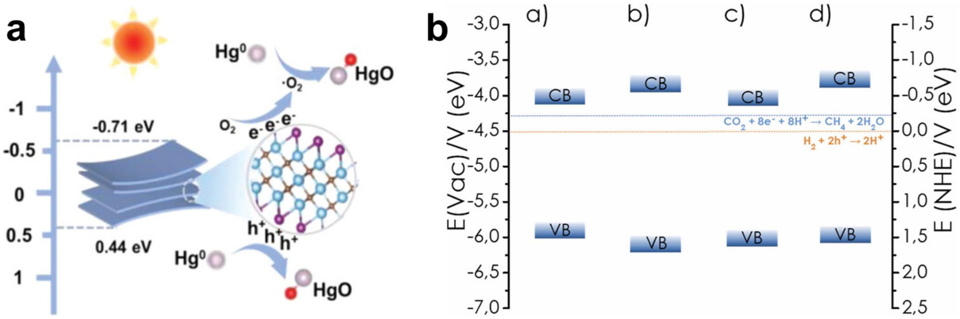

Fig. 39 (a) Band energy and mechanism diagram Ti_3C_2-I_2 for Hg^0 photo-oxidation. (b) Band energy diagram for (a) Ti_3C_2; (b) Ti_2C; (c) Nb_2C; (d) V_2C MXene QDs. The standard reduction potentials of H^+/H_2 and CO_2/CH_4 have also been indicated as references. Reproduced from (a) ref. 228 with permission from Wiley, copyright 2023 and (b) ref. 85 with permission from Elsevier, copyright 2024.

results identified C–Ti–O ensembles as the active motifs facilitating stepwise C–H cleavage, while the 2D lamellar structure prevented coke deposition and improved diffusion. In nitrogen reduction, Sfeir *et al.* reported Co-modified Mo_2CT_x catalysts achieving 9500 μmol $g_{\text{active-phase}}^{-1}$ h^{-1} NH_3 synthesis at 400 °C under 1 bar, operating stably for over 15 days.[229] Further characterization demonstrated that Co–$Mo_2C_{1-\delta}N_\delta T_x$ carbonitride species in which alternating Co and Mo sites create synergistic electron-donation and H-shuttling channels, stabilizing *NNH intermediates and lowering N$\equiv$N activation barriers. These results demonstrate that termination composition, metal substitution, and step-site exposure collectively regulate reaction selectivity and stability in thermal catalysis.

In totality, these electro-, photo-, and thermocatalytic examples confirm that the catalytic performance of MXenes is directly linked to their surface electronic configuration and chemical environment. Across all modalities, DFT-predicted descriptors such as ΔG_{H*}, work function, and d-band center accurately reflect experimental trends in activity and selectivity, validating MXenes as prototypical platforms for interface-programmable catalysis. At the same time, many high-performing systems involve substantial *in situ* reconstruction, and the exact nature of the steady-state active phase is often inferred indirectly rather than resolved unambiguously by *operando* techniques, which introduces uncertainty into some of the proposed structure–reactivity correlations.

5.1.4. Design descriptors and stability of intrinsic catalysts. The observed structure–activity trends can be rationalized using electronic descriptors such as the d-band center, work function, and adsorption free energies (ΔG_{H*}, ΔG_{*COOH}, ΔG_{*OOH}, ΔG_{*NNH}), which quantitatively link surface electronic configuration to reaction thermodynamics. Local charge density and termination-induced dipoles define acidity, basicity, and redox potential, providing predictive control over catalytic performance.

Stability remains a crucial factor under working conditions. MXenes may undergo oxidation, defect migration, or termination loss, leading to dynamically reconstructed active phases. For instance, Fe- or Co-doped Mo_2CT_x evolves into mixed oxyhydroxide–carbon composites during ORR, while $Ti_3C_2T_x$ progressively oxidizes under extended cycling. Such adaptive evolution suggests that MXenes are self-regulating catalysts, capable of reconstructing into energetically favorable, catalytically active configurations. Controlling this evolution, for example through termination stabilization, defect management, or guided reconstruction, will be key to achieving durable, high-efficiency catalytic systems. However, quantitative lifetime metrics, failure modes under technically relevant conditions, and the extent to which reconstructed phases remain MXene-derived are still poorly documented, indicating that stability descriptors lag behind activity descriptors.

To sum up, MXenes act as intrinsically active catalytic centers whose reactivity derives from the interplay between transition-metal d states, surface terminations, and defect-induced polarization. Through deliberate electronic and structural modulation, their adsorption energetics and reaction kinetics can be tuned across electro-, photo-, and thermocatalysis. The coherent integration of theoretical modelling, *operando* spectroscopy, and performance benchmarking positions MXenes as a model platform for interface-programmable catalysis, in which atomic-level electronic design translates directly into macroscopic catalytic functionality. Going forward, the key challenge is to convert this largely qualitative understanding into robust, transferable design rules that can guide the discovery of new MXene compositions and architectures without relying solely on case-by-case empirical optimization.

5.2. MXene as conductive scaffolds and electron mediators

Beyond their intrinsic catalytic activity, MXenes also play a decisive role as conductive mediators that couple redox centers and facilitate charge percolation across hybrid architectures. By integrating metallic-level conductivity, termination-dependent work functions, and excellent interfacial compatibility, MXenes create low-resistance highways for charge transport while actively modulating the direction and energetics of electron flow. In semiconductor/MXene assemblies, they can form Schottky or Ohmic contacts when behaving as metallic components, or Z-scheme/S-scheme heterojunctions when exhibiting semiconducting characteristics, depending on the electronic structure and MXene surface chemistry. This dual electronic identity enables MXenes to act both as conductive frameworks and as Fermi-level modulators, accelerating carrier separation, enhancing charge mobility, and tuning interfacial reaction kinetics. However, most reported systems still treat MXenes as electronically homogeneous phases, and the impact of local termination heterogeneity or defect-induced potential fluctuations on charge mediation remains insufficiently quantified.

5.2.1. Principles: charge highways, interfacial fields, and work-function matching. At a MXene/semiconductor junction, the relative work functions of the two phases determine the direction of electron transfer and the nature of the interfacial contact.[230,231] When MXenes act as metallic or quasi-metallic conductors and the semiconductor possesses a smaller work function (*i.e.*, a higher Fermi level), electrons spontaneously flow from the semiconductor to the MXene until Fermi-level equilibrium is reached, forming a Schottky junction with a depletion region and a built-in electric field pointing from the semiconductor toward the MXene.[232] Conversely, when the semiconductor has a larger work function (*i.e.*, a lower Fermi level), electrons transfer from the MXene to the semiconductor, producing an Ohmic contact characterized by nearly barrier-free charge flow. These charge redistributions originate from dark-state Fermi-level equilibration, which establishes an interfacial potential that subsequently governs the migration of photoexcited carriers under illumination. The pre-established built-in electric field thereby directs photogenerated electrons and holes along opposite pathways, suppressing recombination and improving charge utilization efficiency.

Surface terminations such as –O, –OH, and –F strongly influence these electronic alignments. O-terminated MXenes, with larger work functions, tend to extract electrons and thus favour Schottky-type behavior, whereas hydroxyl-rich or mixed-terminated MXenes with smaller work functions promote Ohmic-like contact, facilitating efficient carrier exchange in coupled redox reactions. Termination-induced dipoles, together with Fermi-level equilibration, generate built-in fields that bend bands and bias carrier motion, allowing controlled charge migration across the interface. When MXenes acquire semiconducting characteristics, typically through surface oxidation, elemental doping, or quantum confinement, they can couple with other semiconductors to form Z-scheme or S-scheme heterojunctions. In these cases, internal band offsets and interfacial fields guide directional charge separation while preserving strong redox potentials, a mechanism fundamentally distinct from the barrier-controlled transport in Schottky or Ohmic contacts.

The 2D lamellar morphology of MXenes provides atomically intimate interfaces and short carrier diffusion paths, while d-orbital hybridization between MXene metals and semiconductor frontier orbitals lowers interfacial resistance and stabilizes intermediates. Through these dual electronic identities, where MXenes behave as metal-like conductors in Schottky/Ohmic junctions and as semiconductor-like partners in Z- or S-scheme architectures, MXenes integrate structural percolation with electronic alignment, functioning as both conductive bridges and potential modulators in next-generation hybrid catalysts. Nevertheless, quantitative mapping of local work-function distributions, interfacial field strength, and band bending in realistic, defect-rich junctions is still scarce, which limits the development of predictive design rules beyond idealized model interfaces.

5.2.2. Electrocatalysis: conductive frameworks and Fermi-level regulation. In electrocatalytic systems, MXenes serve as ideal conductive scaffolds that couple high metallic conductivity with chemical tunability, thereby minimizing charge-transfer resistance and enabling efficient electron delivery to active centers.[233] Their adjustable Fermi levels and termination-dependent surface potentials enable precise electronic alignment with coupled electrocatalysts, reducing interfacial barriers and modulating reaction energetics. When integrated with transition-metal sulfides, phosphides, or hydroxides, MXenes act as electron reservoirs and redox mediators, converting sluggish multielectron steps into kinetically favourable pathways.

A representative example is the hierarchically porous NiCoS/$Ti_3C_2T_x$ hybrid synthesized by Zou *et al.*, in which Ni–Co mixed sulfide nanosheets were *in situ* grown on $Ti_3C_2T_x$ MXene *via* a metal–organic framework (MOF)-derived strategy.[234] The strong orbital coupling between the Ni/Co 3d and Ti 3d states markedly enhanced electron mobility and surface accessibility. During operation, NiCoS underwent a structural transformation into a NiCoOOH–NiCoS core–shell configuration, where the MXene scaffold stabilized the oxyhydroxide phase and facilitated rapid charge exchange. The resulting catalyst delivered OER activity and durability comparable to precious-metal catalysts, confirming that MXenes not only act as conductive pathways but also stabilize dynamically evolving intermediates through interfacial charge redistribution. Similarly, FeNi-layered double hydroxide (LDH)/V_2C MXene composites developed by Chen *et al.* displayed an overpotential of 250 mV at 10 mA cm^{-2} and a Tafel slope of 46.5 mV dec^{-1} for the OER in 1.0 M KOH, significantly outperforming Pt/C + RuO_2 benchmarks.[235] Spin-polarized DFT calculations reveal that in alkaline OER conditions, FeNi-LDH in the $H_2PO_2^-$/FeNi-LDH–V_2C hybrid transforms into Fe-doped NiOOH on O-terminated V_2C (Fig. 40). Mulliken charge analysis shows an electron transfer (0.42 e$^-$ per unit cell) from FeNi-LDH to V_2C, increasing the positive charge on Fe and Ni and enhancing electronic conductivity. DOS/PDOS analysis indicates that V_2C coupling increases electronic states near the Fermi level and downshifts the d-band center (from −2.44 to −3.04 eV, Fig. 40b and c), optimizing adsorption strength of OER intermediates. Free energy diagrams show that the hybrid lowers the rate-determining *OOH formation energy barrier (1.56 eV *vs.* 1.69 eV) and achieves balanced adsorption/desorption energetics, thereby improving reaction kinetics. Overall, the synergistic interaction between FeNi-LDH and V_2C promotes charge transfer and optimal intermediate binding, leading to high oxygen electrocatalytic activity.

To overcome the conductivity loss caused by MXene restacking, Wang *et al.* designed a 3D CNTs@$Ti_3C_2T_x$ framework, where vertically aligned CNT arrays grow between $Ti_3C_2T_x$ layers (Fig. 41a).[215] These CNT pillars serve simultaneously as electronic bridges and structural spacers, preventing lamellar collapse and providing well-defined ion/electron channels. The

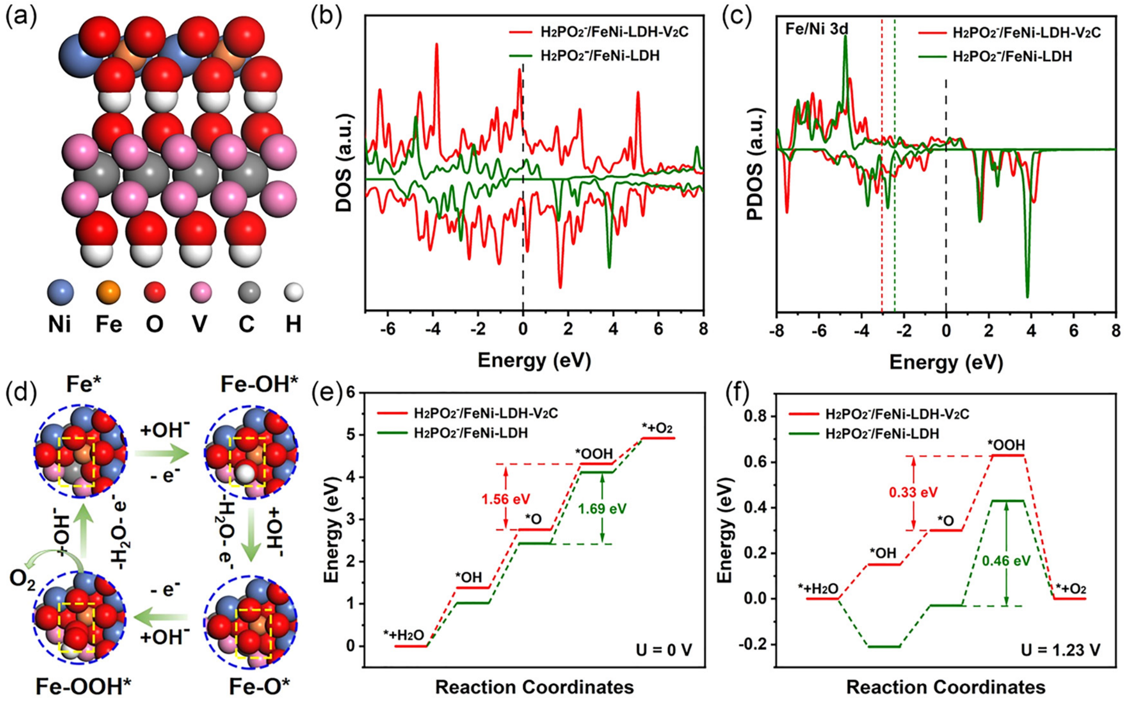

Fig. 40 (a) Side view of model structure of $H_2PO_2^-$/FeNi-LDH-V_2C hybrid system. (b) DOS of $H_2PO_2^-$/FeNi-LDH-V_2C and $H_2PO_2^-$/FeNi-LDH. (c) PDOS of the Ni and Fe 3d orbitals from $H_2PO_2^-$/FeNi-LDH-V_2C and $H_2PO_2^-$/FeNi-LDH. The dashed lines indicate the d-band center for each system. (d) The reaction pathway of OER in alkaline solution. The free energy diagrams at an equilibrium potential of 0 V (e) and 1.23 V (f) for overall OER pathway. Reproduced from ref.[235] with permission from Elsevier, copyright 2021.

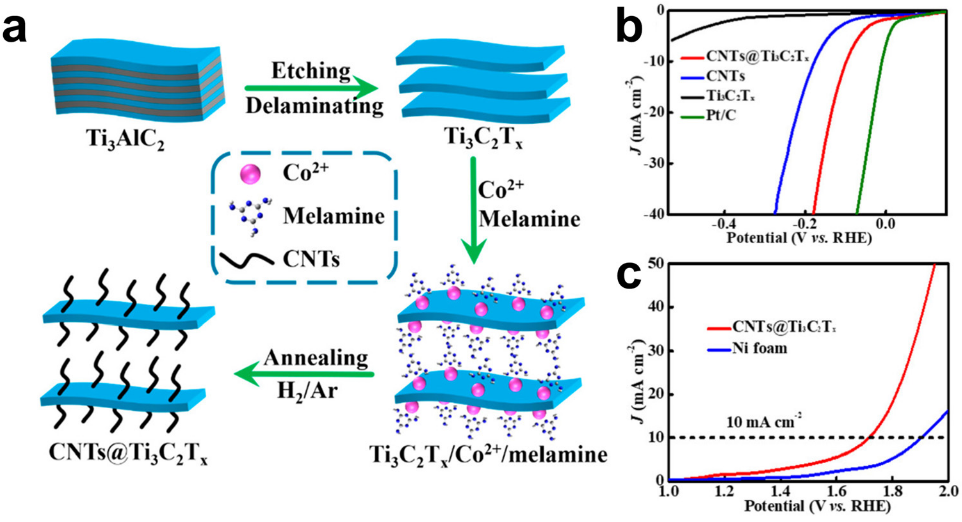

Fig. 41 (a) Schematic Illustration of the Fabrication of 3D CNTs@$Ti_3C_2T_x$. (b) Polarization curves of $Ti_3C_2T_x$, CNTs, 3D CNTs@$Ti_3C_2T_x$, and Pt/C in a typical three-electrode system (scan rate of 2 mV s^{-1} N_2-saturated 1.0 M KOH solution). (c) Polarization curves of a two-electrode alkaline electrolyze using CNTs@$Ti_3C_2T_x$//CNTs@$Ti_3C_2T_x$ and Ni foam//Ni foam as both the cathode and anode at a scan rate of 2 mV s^{-1} in 1.0 M N_2-saturated KOH. Reproduced from ref. 215 with permission from American Chemical Society, copyright 2019.

resulting hybrid exhibited an overpotential of 93 mV at 10 mA cm^{-2} and an onset potential of only 39 mV for the HER, outperforming both pristine $Ti_3C_2T_x$ and CNTs, and approaching the activity of Pt-based catalysts (Fig. 41b). Moreover, in overall water splitting, the CNTs@$Ti_3C_2T_x$ electrode required only 1.72 V to reach 10 mA cm^{-2} (Fig. 41c), highlighting the synergistic effect of ultrafast charge transport and efficient active-site exposure enabled by the open 3D configuration.

Viewed holistically, these studies demonstrate that MXenes function as electronically active backbones that couple with redox centers *via* strong orbital hybridization and Fermi-level matching. The resulting interfacial charge redistribution simultaneously lowers activation barriers, minimizes overpotentials, and stabilizes metastable intermediates during operation, offering a general mechanistic framework for the rational design of high-efficiency electrocatalysts.[236] Nonetheless, most systems have been evaluated under laboratory-scale current densities and limited cycling times, and systematic *operando* studies on MXene conductivity evolution, termination rearrangement, and long-term interface degradation under technologically relevant loads are still lacking, which constrains direct translation to practical electrolyzer conditions.

5.2.3. Photocatalysis: interfacial polarization and directional carrier flow. In photocatalytic systems, MXenes function as electron mediators and polarization regulators that accelerate photogenerated charge separation while preserving redox potentials. Their metallic conductivity and high carrier mobility allow them to serve as ultrafast electron sinks, whereas termination-controlled work functions dictate the direction of interfacial charge migration and carrier lifetime.[237–241] For example, CdS/Ti_3C_2 composites prepared by Ran *et al.* achieved a hydrogen evolution rate of 14 342 μmol h^{-1} g^{-1} and an apparent quantum efficiency of 40.1% under 420 nm irradiation, among the highest for noble-metal-free photocatalysts.[242] DFT calculations revealed that the Fermi level of Ti_3C_2 MXene lies below that of CdS, leading to dark-state electron transfer from CdS to Ti_3C_2 and establishing a Schottky junction that promotes photogenerated electron extraction and suppresses recombination (Fig. 42). Oxygen-terminated Ti_3C_2 acts as an efficient electron reservoir, mediating proton reduction through Ti–O–H intermediates. Comparable behavior has been reported in ZnS/Ti_3C_2 and $Zn_xCd_{1-x}S$/Ti_3C_2 systems, underscoring the generality of MXenes as noble-metal substitutes for hydrogen evolution.

In another example, Ti_3C_2/Bi_2WO_6 heterostructures fabricated by Cao *et al.* featured *in situ*-grown Bi_2WO_6 nanosheets forming an extensive 2D/2D interface with atomic-level contact.[207] Under simulated solar light, the composite achieved a 4.6-fold increase in total CO_2 reduction rate compared with pristine Bi_2WO_6, producing both CH_4 and CH_3OH with high selectivity. The enhancement stems from a strong interfacial electric field at the MXene/Bi_2WO_6 junction, which directs photoexcited electrons toward Ti_3C_2 and confines holes within Bi_2WO_6 (Fig. 43). The large interfacial area, excellent conductivity, and chemical stability of the MXene layer collectively accelerate charge transport and stabilize *CO_2-derived intermediates (*COOH, *CHO), enabling multielectron reduction processes inaccessible to bare Bi_2WO_6.

Beyond acting as electron sinks, MXenes actively regulate local interfacial polarization through surface dipoles and termination chemistry. Strong –O/–OH dipoles at the Ti–O interface induce local band bending and create self-driven fields that enhance charge separation even without external bias. When coupled with semiconductors in Z- or S-scheme architectures, this polarization ensures that photogenerated high-energy electrons and holes remain localized on reduction- and oxidation-active components, respectively, while low-energy carriers recombine across the MXene interface—maximizing redox efficiency and product selectivity.

Collectively, these results establish MXenes as active interfacial regulators rather than passive conductive additives. Their dual function, which combines metallic conduction for rapid electron extraction and chemical tunability for polarization control, renders them indispensable for constructing high-performance photocatalysts with efficient carrier separation, strong redox capability, and long-term operational stability. Even so, the trade-off between efficient electron extraction and potential light shielding by MXene layers, as well as the resilience of interfacial polarization under continuous illumination and realistic photocatalytic conditions, remains insufficiently clarified and calls for more systematic *operando* optical–electrical characterization.

5.2.4. Summary and outlook. MXenes have emerged as multifunctional electronic mediators that bridge structural connectivity with interfacial energetics. By coupling metallic

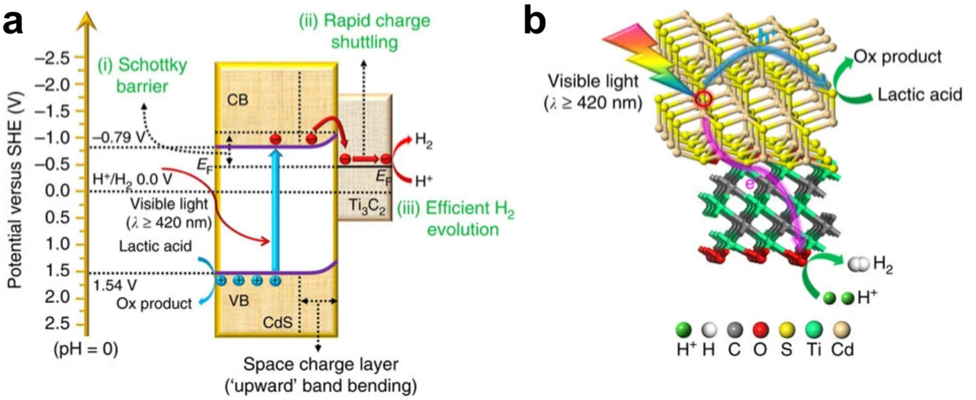

Fig. 42 (a) The charge separation and transfer in the CdS/Ti_3C_2 system under visible-light irradiation. Red and blue spheres denote photo-induced electrons and holes, respectively. (b) Proposed mechanism for photocatalytic H_2 production in the CdS/Ti_3C_2 system under visible-light illumination. Green sphere denotes H^+. White, grey, red, yellow, cyan and gold spheres denote H, C, O, S, Ti and Cd atoms, respectively. Reproduced from ref. 242 with permission from Springer Nature, copyright 2017.

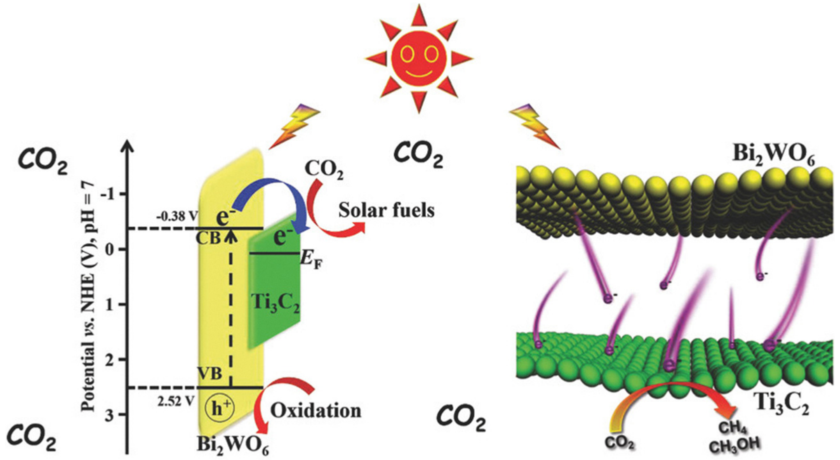

Fig. 43 Energy level structure diagram of Bi_2WO_6 and Ti_3C_2 (left), and Photo-induced electron transfer process at the interface of the hybrids (right). Reproduced from ref. 207 with permission from Wiley, copyright 2018.

conductivity, tunable work functions, and chemical adaptability, they not only minimize charge-transfer resistance but also govern carrier dynamics and reaction pathways across electro-, photo-, and hybrid catalytic systems. Their interfaces exhibit self-adjusting Fermi levels and adaptive polarization, enabling continuous charge redistribution and sustained activity under operating conditions. In parallel, MXene-containing heterostructures highlight the importance of simultaneously engineering morphology, termination chemistry, and band alignment to achieve coherent charge percolation from the atomic scale to the device level. Looking ahead, integrating MXenes into dynamic heterostructures, in which charge flow, dipole evolution, and lattice flexibility are co-optimized, will unlock new paradigms for efficient, durable, and programmable catalysis. A key priority will be to move beyond phenomenological performance enhancements toward quantitatively benchmarked descriptors of interfacial resistance, field strength, and stability under bias, supported by *operando* spectroscopy and multiscale simulations. Only then can MXene-based conductive scaffolds be designed in a truly predictive manner for next-generation electrochemical and photoelectrochemical technologies.

5.3. MXene as structural stabilizers

Beyond functioning as active centers and charge mediators, MXenes exhibit a remarkable capacity to stabilize catalytic architectures under demanding thermal, chemical, and electrochemical environments. Their 2D lamellar morphology, high conductivity, and tunable surface chemistry collectively enable them to serve as both mechanical cushions and electronic buffers, preventing catalyst deactivation through sintering, phase transformation, or leaching. Building on Sections 5.1 and 5.2, which established intrinsic activity and charge-mediation roles, this section concentrates on how MXenes encode durability *via* structure–electron co-engineering.[166,243,244]

From an interfacial and structural perspective, MXene-based stabilization manifests through four primary mechanisms. The first is immobilization and atomic dispersion, where surface terminations and interlayer confinement allow precise anchoring and distribution of catalytic species. The second is interfacial bonding and electronic stabilization, in which strong metal–support coupling modifies charge density and valence states. The third is confinement and anti-sintering, where the flexible layered framework buffers mechanical and thermal stresses to prevent particle migration and collapse. The fourth is framework reinforcement and structural protection, in which MXenes act as reinforcing backbones for porous or hybrid structures. These effects frequently act cooperatively, giving MXenes an electronic–mechanical dual buffering capacity that ensures both structural robustness and catalytic persistence.

5.3.1. Immobilization and atomic dispersion. MXenes possess abundant surface terminations (–O, –OH, –F) and negatively charged layers that can immobilize metal atoms, clusters, and nanoparticles through electrostatic attraction, coordination bonding, or intercalation.[245] This immobilization strategy suppresses aggregation and allows uniform atomic dispersion, leading to high site accessibility and low-resistance, delocalized electron communication between the active species and the MXene substrate.

A representative system was developed by Guan and co-workers, who prepared an atomic-scale RuPt–$Ti_3C_2T_x$ catalyst using a controlled impregnation–reduction method.[246] In this multi-site configuration, Ru and Pt atoms were individually anchored on the $Ti_3C_2T_x$ surface, while Ti sites within the MXene lattice provided additional electronic mediation (Fig. 44a). Structural analysis confirmed the coexistence of isolated Ru, Pt, and Ti atoms forming Ru–Ti–Pt triads. During ammonia borane hydrolysis, these distinct centers performed complementary roles: Ru activated the B–H bond, Pt facilitated O–H bond cleavage, and Ti promoted hydrogen desorption through cooperative *H transfer. This tandem mechanism yielded an exceptional turnover frequency of approximately 1291 to 1293 min^{-1}, nearly nine times higher than that of single-site Ru catalysts, highlighting how atomic immobilization combined with electronic delocalization maximizes efficiency.

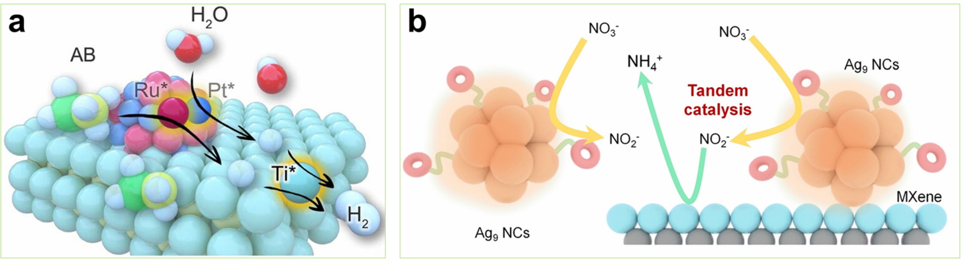

Fig. 44 (a) Schematic diagram of ammonia borane hydrolysis on RuPt–Ti multi-site. (b) Schematic diagram of the NO$_3$RR mechanisms over Ag$_9$ NCs and composited Ag$_9$/MXene catalysts. Reproduced from (a) ref. 246 and (b) ref. 247 with permission from Wiley, copyright 2024.

Similarly, Ag$_9$ nanoclusters supported on Ti$_3$C$_2$T$_x$ MXene (Ag$_9$/MXene) exhibit superior activity and durability in the electrochemical reduction of nitrate to ammonia.[247] *Operando* characterization demonstrated that the MXene scaffold prevented Ag cluster coalescence, stabilized the cluster structure, and provided a continuous conductive pathway for electron transfer (Fig. 44b). The catalytic process proceeds *via* a tandem mechanism, in which Ag sites catalyze the initial nitrate reduction to nitrite, while the MXene substrate facilitates subsequent conversion to ammonia. The system maintained structural and electrochemical stability for more than 108 h of continuous operation, underscoring how MXene confinement and conductivity together stabilize active nanoclusters and sustain long-term catalysis. Despite these advances, atomically resolved evidence for the precise coordination environment, migration pathways, and deactivation modes of immobilized species on MXenes is still scarce, and most conclusions rely on indirect spectroscopic fingerprints rather than fully resolved structural models.

5.3.2. Interfacial bonding and electronic stabilization. At the electronic level, MXenes can form SMSI or reactive metal–support interactions (RMSI) that result in charge redistribution, alloying, and valence stabilization. These effects enhance adhesion, inhibit metal leaching, and stabilize the oxidation states of the catalytic components, ensuring both durability and performance consistency during redox cycling.

Li and co-workers first demonstrated RMSI behavior between platinum and a non-oxide support using Pt/Nb$_2$CT$_x$ MXene as a model system.[248] Upon moderate reduction at around 350 °C, the surface terminations of Nb$_2$CT$_x$ were partially removed, leading to the *in situ* formation of Pt–Nb alloy motifs. This reactive interface altered the electronic structure of Pt, weakening CO adsorption and reducing susceptibility to poisoning during the water–gas shift reaction. The Pt–Nb interface also provided sites for efficient H$_2$O activation, significantly enhancing reaction kinetics. Compared with traditional oxide supports, the non-oxide MXene support promoted faster electron transfer and higher CO tolerance, proving the feasibility of non-oxide RMSI for tuning catalyst stability and activity simultaneously.

In a subsequent study, the same group exploited RMSI to achieve *in situ* alloying and intermetallic compound (IMC) formation within Pt/Ti$_3$C$_2$T$_x$ and Pt/Nb$_2$CT$_x$ systems.[200] Controlled interfacial diffusion led to the emergence of ordered Pt$_3$Ti and Pt$_3$Nb phases with Cu$_3$Au-type structures, previously unreported on oxide supports. These intermetallic catalysts demonstrated remarkable thermal stability and sustained C–H activation efficiency in light alkane dehydrogenation. High-resolution STEM images revealed coherent interfaces between the intermetallic domains and the MXene substrate, while DFT calculations showed that the electronic d-band centers were downshifted, thereby optimizing adsorption strengths and preventing overbinding. Together, these results show that MXene-templated interfacial alloying combines electronic stabilization with structural integrity, yielding catalysts that retain activity and structure under harsh conditions. On the other hand, SMSI- or RMSI-like encapsulation can, in principle, also reduce accessible surface area or alter selectivity, and systematic comparisons with oxide-based analogues across broader metal–MXene combinations are still needed to establish how general these stabilization motifs truly are.

5.3.3. Confinement and anti-sintering under harsh conditions. MXenes' flexible lamellar frameworks provide nanoscale confinement and mechanical adaptability, suppressing particle migration, agglomeration, and carbon deposition during high-temperature or reducing reactions. Their 2D galleries act as elastic cushions that absorb strain while maintaining open diffusion channels for reactant and product transport.

In the nonoxidative coupling of methane (NOCM), Li *et al.* employed Mo$_2$TiC$_2$T$_x$ MXene to anchor atomically thin platinum nanolayers (1–2 atomic layers).[201] The strong Pt–Mo interfacial bonding not only anchored the ultrathin metallic layer but also modulated its electronic structure, shifting the Pt 5d band upward and weakening CH$_3$* adsorption. These changes facilitated methyl radical desorption and minimized deep dehydrogenation, effectively suppressing carbon accumulation. Under reaction conditions at 750 °C, the catalyst achieved approximately 7% CH$_4$ conversion and more than 98% selectivity toward C$_2$ hydrocarbons (C$_2$H$_4$/C$_2$H$_6$), maintaining stable operation for 72 h with approximately one percentage point decrease in conversion after oxidative regeneration. This example demonstrates how MXene confinement, interfacial bonding, and electronic modulation jointly stabilize active nanostructures against high-temperature degradation (Fig. 45a).

A comparable stabilization mechanism was observed by Wei *et al.* in Pd metallene/Nb$_2$C MXene composites.[249] Through spontaneous redox substitution at room temperature, 3D Pd nanoparticles were transformed into 2D metallenes firmly

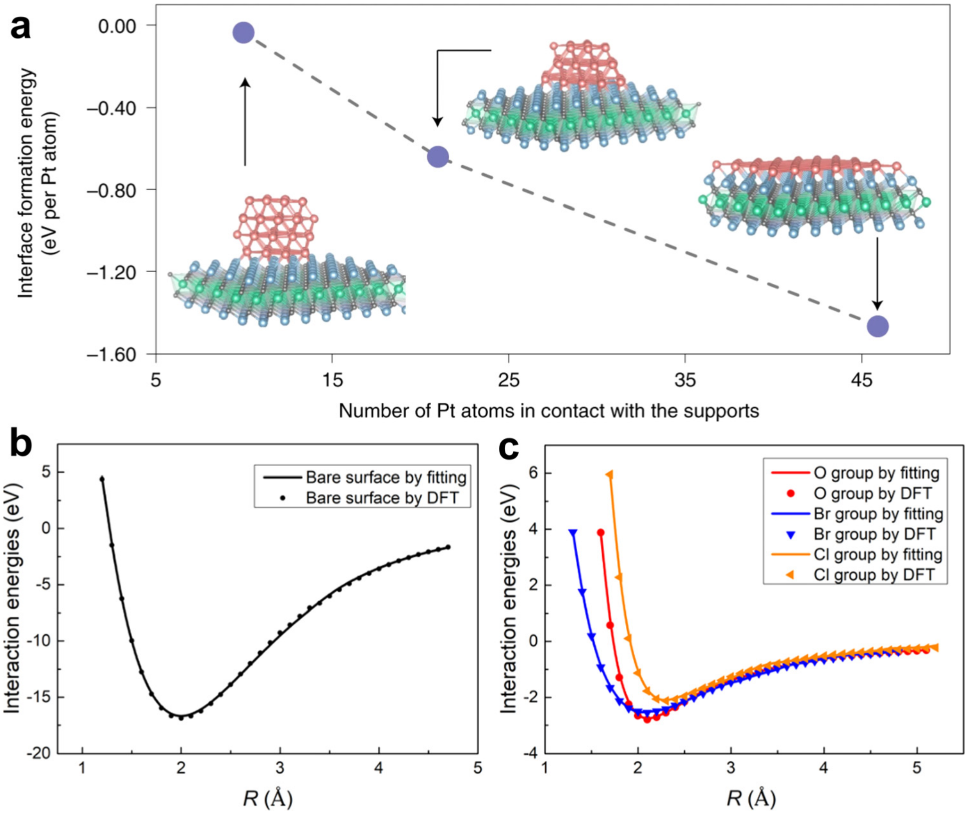

Fig. 45 (a) DFT calculated energy per Pt atom of different nanostructured architectures on the surface of $Mo_2TiC_2T_x$ MXene. Interaction energies for the DFT calculations and the fitted Morse potential curve with the structures of (b) Pd_4/Nb_2C, (c) Pd_4/O_2Nb_2C, Pd_4/Br_2Nb_2C and Pd_4/Cl_2Nb_2C. Reproduced from (a) ref. 201 and (b) and (c) ref. 249 with permission from Springer Nature, copyright 2021 and 2023.

anchored to Nb_2C (Fig. 45b and c). Electron transfer from subsurface Nb atoms to Pd promoted the formation of a stable "tripod" configuration with a cyclohexane-like six-membered ring geometry. This structure facilitated rapid olefin adsorption–desorption cycles and suppressed overhydrogenation. Even with a Pd loading of only 0.5 wt.%, the catalyst achieved a turnover frequency of 10 372 h^{-1} and 96% selectivity in the semi-hydrogenation of phenylacetylene. The combination of mechanical confinement and charge redistribution in this system exemplifies the multifunctional stabilization capability of MXenes under dynamic reaction conditions. Nevertheless, the long-term phase stability of MXene supports themselves at elevated temperatures, including potential oxidation, carbide–oxide transformation, or termination loss, is rarely tracked beyond tens of hours, so the ultimate limits of MXene-based confinement under industrially relevant timescales remain to be clarified.

5.3.4. Framework reinforcement and structural protection. Beyond discrete nanoparticles or clusters, MXenes also reinforce porous and hybrid frameworks, enhancing mechanical, thermal, and hydrothermal resilience. Their sheet-like morphology provides load-bearing structural layers, while their conductive and hydrophilic surfaces facilitate interfacial bonding and charge transfer within complex networks.

Gu and co-workers integrated $Ti_3C_2T_x$ MXene into the copper-based MOF HKUST-1, forming a HKUST-1/$Ti_3C_2T_x$ hybrid with superior structural and catalytic properties.[250] The addition of MXene increased the surface area from 1210 m^2 g^{-1} for pristine HKUST-1 to 1380 m^2 g^{-1} for the composite, while preserving its crystallinity. Under hydrothermal conditions at 70 °C, the hybrid maintained structural integrity, whereas the unmodified MOF suffered severe collapse (Fig. 46). In the styrene oxide ring-opening reaction, the MXene-containing catalyst reached 76.7% conversion within 20 minutes, compared with only 23.1% for pure HKUST-1, and retained activity over six cycles. The improvement arises from multiple effects: MXene layers act as hydrolytic barriers that prevent cleavage of metal–ligand bonds, their high porosity accelerates molecular diffusion, and the strong interfacial polarization between MXene sheets and Cu sites facilitates charge redistribution during catalysis. This example demonstrates how MXene incorporation simultaneously enhances framework stability, mass transport, and electron mobility, thereby transforming fragile porous materials into robust hybrid catalysts suitable for industrial applications. Even so, demonstrations are still restricted to a limited number of MOF and zeolite frameworks under relatively mild hydrothermal or chemical conditions, and systematic assessment of scalability, regenerability, and resistance to real feed impurities will be required before MXene-reinforced frameworks can be credibly positioned as industrial stabilizers.

5.3.5. Summary and outlook. MXenes act as comprehensive structural stabilizers that integrate mechanical confinement

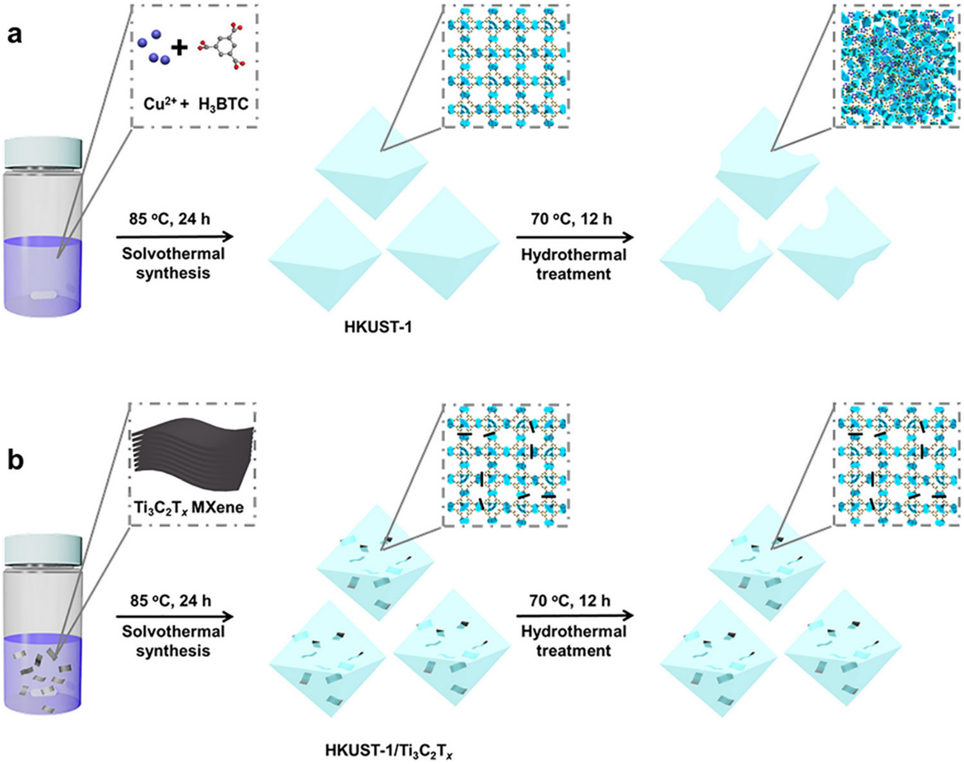

Fig. 46 Schematic diagram for the synthesis and hydrothermal stability of (a) HKUST-1 and (b) HKUST-1/$Ti_3C_2T_x$ hybrid materials. The hybrid materials can maintain the structure well after hydrothermal treatment at 70 °C for 12 h, while the structure of pure HKUST-1 is broken. Reproduced from ref. 250 with permission from American Chemical Society, copyright 2021.

with electronic regulation. Through coordination anchoring, they immobilize catalytic species and ensure atomic dispersion; through interfacial coupling (SMSI/RMSI), they stabilize valence states and prevent leaching; through lamellar confinement, they inhibit sintering and carbon deposition; and through framework reinforcement, they endow hybrid materials with mechanical and hydrothermal durability.

Importantly, these stabilization pathways are mutually reinforcing rather than independent. Atomic-scale charge redistribution complements mechanical flexibility at the mesoscale, producing catalysts that evolve adaptively while maintaining structure and function. Future efforts should focus on precisely controlling termination chemistry, interlayer spacing, and alloying dynamics to direct structural evolution under *operando* conditions. Integrating real-time spectroscopic and microscopic characterization with first-principles simulations will be essential to elucidate the interplay between charge flow, strain relaxation, and stability. In addition, unified metrics for stability, such as standardized stress tests, deactivation fingerprints, and reconstruction maps, are still lacking for MXene-based stabilizers and will be crucial for comparing different systems on a common footing. Ultimately, MXenes transcend their role as passive supports to become adaptive structural stabilizers, materials that encode durability, selectivity, and reactivity directly within their interfacial architecture, while providing a robust platform for multi-energy synergistic catalysis discussed in Section 5.4.

5.4. MXene in multi-energy synergistic catalysis

Modern catalysis increasingly demands materials capable of integrating multiple energy inputs, such as light, heat, electricity, and even mechanical or acoustic stimuli, into a unified reaction pathway. In such multi-energy synergistic systems, the catalyst not only provides chemically active sites but also serves as an energy transducer and relay hub, converting and redistributing diverse energy forms to optimize reaction kinetics and selectivity. Traditional catalysts that are optimized for a single energy mode often suffer from limited efficiency or incomplete utilization of the available input, whereas materials that can couple photo-, electro-, and thermally driven processes exhibit superior activity and energy efficiency.

MXenes, with their metallic-level conductivity, broadband optical absorption, high specific surface area, and surface-engineerable terminations, naturally satisfy the criteria for multi-energy catalysis. Their free-electron density and plasmonic response enable efficient light-to-heat conversion; their high carrier mobility supports rapid electron and heat transport; and their termination-dependent work functions allow dynamic Fermi-level alignment with other semiconductors or metals. These features allow MXenes to act simultaneously as conductive scaffolds, plasmonic heaters, and polarization mediators, transforming them into multifunctional platforms that channel energy flow across coupled catalytic processes. However, quantitative benchmarks that disentangle the relative contributions of photothermal, plasmonic, and purely electronic effects are still sparse, which complicates rigorous comparison with established single-mode catalysts.

5.4.1. Fundamental mechanisms of energy coupling. In multi-field reaction environments, MXenes participate in several cooperative energy-conversion processes that couple optical, electrical, and thermal channels. First, photothermal conversion in MXenes primarily arises from broadband optical absorption followed by rapid non-radiative electron–phonon relaxation within their conductive layers. This process efficiently converts photon energy into localized heat on sub-nanosecond timescales, distinct from resistive (Joule) heating that occurs under an applied electrical current. The resulting local temperature rise can accelerate endothermic surface reactions such as CO_2 reduction, CH_4 reforming, and ammonia decomposition by lowering activation barriers. Second, the plasmonic response, which has been observed in metallic MXenes such as $Ti_3C_2T_x$, $Mo_2TiC_2T_x$, and related compositions, induces localized electromagnetic fields and can generate energetic ("hot") carriers. These plasmon-excited electrons and near-field effects enhance light absorption and facilitate charge transfer to adsorbed molecules or adjacent catalytic phases, thereby coupling optical excitation with interfacial electron dynamics. Third, interfacial polarization arising from work-function mismatch or asymmetric terminations (*e.g.*, –O *vs.* –OH) establishes built-in electric fields that direct charge migration under illumination or applied bias. Depending on the electronic character of the coupled components, these interfacial fields can facilitate Schottky or Ohmic contacts in metal–semiconductor junctions, or drive Z-scheme and S-scheme charge-transfer pathways in semiconductor-based heterostructures, thereby enhancing carrier separation efficiency and accelerating interfacial charge flow. Finally, under electrochemical operation, electrothermal coupling emerges from resistive (Joule) heating within the highly conductive MXene network combined with efficient electron–phonon interactions. Because of their low heat capacity and high thermal diffusivity, thin MXene films can undergo rapid, spatially localized temperature modulation, which complements charge transport and may assist thermoelectric or photoelectrochemical processes. Collectively, these effects establish MXenes as energy-responsive interfacial junctions, where light, electricity, and heat converge through coupled photothermal, plasmonic, and electrothermal mechanisms to drive otherwise kinetically limited catalytic transformations. At the same time, direct *in situ* mapping of local temperature, field strength, and hot-carrier flux at MXene interfaces remains technically challenging, so most mechanistic assignments still rely on indirect proxies and model calculations rather than fully resolved experimental observables.

5.4.2. Photothermal catalysis for CO_2 conversion. In photothermal catalytic CO_2 reduction, MXenes exhibit the dual advantages of efficient light-to-heat conversion and structural robustness. Wu *et al.* designed a Ru cluster catalyst supported on Mo_2TiC_2 MXene (Ru/Mo_2TiC_2), integrating broadband solar absorption with strong metal–support coupling.[251] Under concentrated solar irradiation, the catalyst efficiently promoted the reverse water–gas shift (RWGS) reaction, converting CO_2 and renewable hydrogen into CO with remarkable selectivity. The optimized system delivered a CO yield of 4.0 mol g_{Ru}^{-1} h^{-1}, surpassing nanoparticle-based analogues by more than an order of magnitude and ranking among the most active photothermal RWGS catalysts reported to date.

Operando spectroscopy revealed that the active interface consisted of $Ru/RuO_x/MoO_x/Mo_2TiC_2$ heterolayers, where the intimate Ru–MXene contact induced strong charge delocalization and thermal stability even at elevated temperatures. The MXene support provided exceptional photothermal conversion efficiency, rapidly increasing the surface temperature under solar flux and thereby accelerating the endothermic reaction kinetics. Furthermore, the interfacial MoO_x layer optimized CO adsorption–desorption equilibria, suppressing CH_4 formation and enhancing CO selectivity. Quantitatively, the photothermal efficiency of Ru/Mo_2TiC_2 was 2.6 times higher than that of Ru nanoparticles supported on Mo_2TiC_2 and over 80 times higher than that of SiO_2-supported Ru clusters. These results demonstrate that the coupled photothermal and interfacial electronic effects in MXene-based catalysts can fundamentally reshape reaction energetics by coupling photon absorption, thermal activation, and electron transfer. Nevertheless, most demonstrations are still performed under well-controlled laboratory conditions with idealized CO_2/H_2 feeds, and systematic evaluation under diluted streams, realistic solar flux profiles, and long-term cycling is needed to determine whether such photothermal advantages can be translated into process-relevant CO_2 conversion technologies.

5.4.3. Photoelectrocatalysis for water oxidation. In photoelectrochemical (PEC) water splitting, MXene-derived nanostructures enable simultaneous photonic, electronic, and plasmonic enhancement. Tang *et al.* fabricated cobalt-terminated Janus Ti_3C_2 MXene QDs (Co-MQDs) as Schottky photoanodes for water oxidation.[252] By adjusting the thermal anchoring temperature, the cobalt content and surface configuration could be precisely tuned. The introduced Co terminals served not only as oxygen-evolution active sites but also as plasmonic antennas, producing localized surface plasmon resonance (LSPR) that extended light absorption well into the visible region (Fig. 47).

Simultaneously, the asymmetric Janus structure established a Schottky barrier between Co sites and the Ti_3C_2 core, which facilitated photogenerated electron–hole separation and reduced recombination losses. The overall activity benefited from three synergistic effects: (i) LSPR-enhanced light harvesting at Co terminals, (ii) Schottky-driven charge rectification at the Co–MXene interface, and (iii) accelerated oxygen evolution kinetics at Co sites. The optimized Co-MQD-48 photoanode achieved a photocurrent density of 2.99 mA cm^{-2} and a carrier-transfer efficiency of 87.6% at 1.23 V (*vs.* the reversible hydrogen electrode, RHE), representing 194% and 236% improvements, respectively, over pristine MXene QDs, and maintained 2.79 mA cm^{-2} after 10 h continuous operation. This system illustrates how plasmonic excitation, Schottky modulation, and catalytic activity can be seamlessly integrated within a single

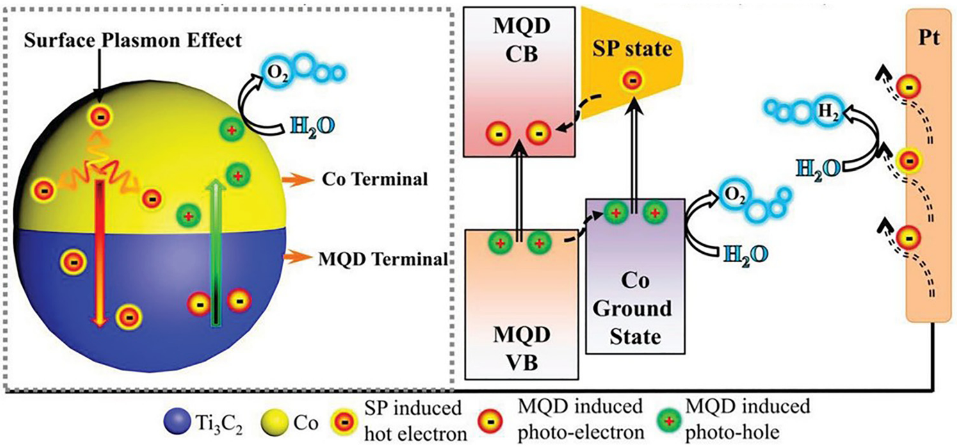

Fig. 47 Schematic illustration of light harvesting and carrier separation mechanism of the Janus-structured Co-MQD. Under illumination, due to the unique Schottky-junction at Co/MQD interface, the hot electrons generated from Co NP are immediately injected to MQD. Meanwhile, accompanied by the excitation of MQD, the photoelectron of MQD and hot electron in Co will be transported to the counter electrode. At the same time the photo-hole produced by excited MQD will go through Co terminal and oxidize OH^- into O_2, which makes Co terminal act as the water oxidation reaction center. Reproduced from ref.[252] with permission from Wiley, copyright 2020.

MXene nanostructure to enable efficient multi-energy coupling. However, these proof-of-concept architectures are typically evaluated in model electrolytes and on small-area electrodes, and issues such as scaling, long-term mechanical integrity of MXene films, and compatibility with integrated PEC device architectures remain largely unaddressed.

5.4.4. Enhanced electrocatalysis by plasmon-induced thermalization. The electrocatalytic activity of MXenes can be boosted by utilizing their plasmonic response to electromagnetic waves. Wu *et al.* presented an effective strategy to enhance their intrinsic electrochemical performance by exploiting their localized surface plasmon resonance (LSPR) in the visible to near-infrared (Vis–NIR) range.[253] LSPR generates two key effects: a thermoplasmonic effect that reduces the endothermic enthalpy and potential barrier for the hydrogen evolution reaction (HER), and a hot-electron effect, which lasts from sub-femtoseconds to picoseconds, that improves interfacial charge transfer and lowers activation energy (Fig. 48). Together, these effects increase HER activity of various MXenes (Nb_2CT_x, $Ti_3C_2T_x$, $V_4C_3T_x$) more than fivefold, with enhanced kinetics and faradaic efficiency across the full pH range. Specifically, the thermoplasmonic effect yields a 40–61% current increase for $Ti_3C_2T_x$ under different pH conditions, while the hot-electron effect provides a 20–48% rise in faradaic efficiency and a 41–65% (in acid) or 21–36% (in alkaline) reduction in activation energy. This LSPR-based approach is broadly effective for multiple MXene types in varied chemical environments. Yet, controlling light penetration depth, local temperature gradients, and potential hot-spot degradation in practical electrode geometries remains non-trivial, and more refined thermo-electrochemical models are needed to avoid overestimating plasmonic gains in technologically relevant configurations.

5.4.5. Perspectives and future directions. The above studies exemplify how MXenes, through their coupled optical, electrical, and thermal functionalities, act as energy-relay centers that harmonize multiple excitation pathways. By integrating photothermal heating, plasmon-induced charge excitation, and field-driven carrier separation, MXenes transcend conventional catalyst design to establish a multi-energy coordination paradigm.

Going ahead, rational design of MXenes for multi-energy catalysis will benefit from three complementary approaches. First, tailoring band structures and surface terminations will enable selective coupling to distinct energy channels, for example by optimizing the balance between hot-electron lifetime and thermal dissipation. Second, engineering interfacial architectures, such as hybrid plasmonic heterojunctions or hierarchical conductive networks, will allow dynamic modulation of energy flow and localized field distribution. Third, integrating *operando* spectroscopies with multiscale simulations will be crucial to resolve transient processes such as hot-carrier generation, phonon–electron coupling, and localized heating at reaction sites. In parallel, robust and comparable metrics for multi-energy conversion efficiency and stability will be required to move beyond qualitative enhancement claims and to benchmark MXene-based systems against incumbent catalytic technologies.

By uniting these approaches, MXene-based materials are poised to evolve from passive conductors or cocatalysts into programmable energy mediators, materials capable of orchestrating light, heat, and charge to achieve synchronized reaction control. This multifunctional adaptability positions MXenes at the forefront of multi-energy synergistic catalysis, where the seamless integration of diverse energy forms paves the way toward efficient CO_2 valorization, solar-driven chemical synthesis, and next-generation sustainable energy conversion technologies.

5.5. Mechanistic insights and common principles

The preceding sections collectively demonstrate that the catalytic versatility of MXenes originates from the interplay of

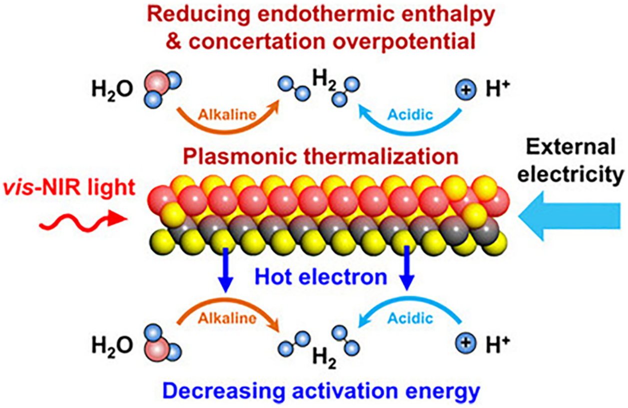

Fig. 48 Schematic illustration of the positive contribution of the LSPR-induced photothermal and hot-electron effect to improve the electrocatalytic HER performance of MXenes. Reproduced from ref. 253 with permission from Wiley, copyright 2021.

tunable electronic structure, interfacial coupling, and structural adaptability. Whether serving as intrinsic active centers, conductive scaffolds, structural stabilizers, or multi-energy mediators, MXenes display a consistent mechanistic behavior in which charge redistribution and interfacial polarization govern catalytic kinetics and selectivity. These observations motivate a unified mechanistic picture that links electronic tuning, interface chemistry, and dynamic structural responses across diverse catalytic environments.

5.5.1. Unified mechanistic framework. Across electro-, photo-, and thermochemical systems, MXene-based catalysis can be described by three mutually reinforcing processes (Fig. 49). First, MXenes act as electronically adaptive mediators whose Fermi level, work function, and d-band position respond sensitively to composition and surface terminations. This tunability dictates charge-transfer directionality, adjusts intermediate adsorption strengths, and aligns redox potentials with adjacent catalytic phases. Fermi-level equilibration establishes built-in electric fields that facilitate carrier separation and lower activation barriers, providing a direct electronic link between band structure and catalytic function.

At the same time, strong orbital hybridization and interfacial polarization within MXene-based junctions produce localized potential gradients and charge delocalization. These interactions accelerate electron exchange and stabilize key transition states, thereby reshaping reaction coordinates through cooperative reactivity between MXene metal centers and neighbouring components. Such polarized interfaces operate as programmable electronic fields that bridge atomic-level polarization with macroscopic reaction selectivity.

In addition, MXenes exhibit an unusual degree of structural adaptability under operating conditions. Their layered lattices permit controlled surface reconstruction, termination evolution, and defect migration without substantial loss of crystallinity. These processes often lead to *in situ*-generated oxycarbide, carbonitride, or alloy-like phases that sustain activity over extended operation. This adaptive behavior distinguishes MXenes from more rigid oxides or metals, although the pathways and kinetics of phase evolution remain insufficiently resolved. The coupling of charge redistribution with lattice relaxation therefore provides a foundation for sustained reactivity and long-term stability.

5.5.2. Causal relationship from interfacial polarization to reaction kinetics. The relationship between MXene electronic structure and catalytic behavior follows a continuous cause–effect chain linking interfacial polarization with reaction kinetics. Local electric fields arising from polarization modulate adsorption configurations and activation barriers, thereby steering reaction pathways, product selectivity, and turnover frequency. In this sense, charge redistribution functions not as a passive outcome of contact equilibration but as an active driver of thermodynamic and kinetic control at the surface. However, quantifying the magnitude and spatial distribution of these interfacial fields under realistic conditions remains challenging, and current mechanistic assignments often rely on

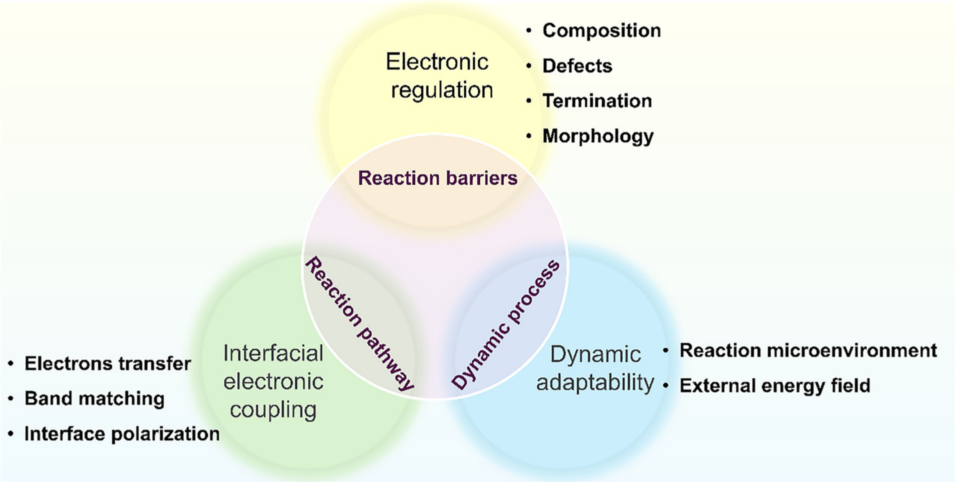

Fig. 49 Unified mechanistic framework of MXene-based catalysis.

indirect observables such as shifts in binding energies or changes in reaction orders. Developing reliable, quantitative metrics for field-induced catalytic effects will be essential for fully validating this continuum model and for integrating MXenes into predictive mechanistic frameworks.

5.5.3. Outlook: toward predictive interface design. Advancing MXene-based catalysis from empirical optimization to predictive design requires an integrated understanding of charge flow, interfacial fields, and reaction energetics under *operando* conditions. Real-time spectroscopies, including XPS, XAS, diffuse reflectance infrared Fourier transform spectroscopy (DRIFTS), and femtosecond transient absorption spectroscopy (fs-TAS), will be central to resolving transient charge redistribution, bond activation, and structural evolution, while first-principles simulations and *ab initio* molecular dynamics can quantify interfacial polarization and correlate field effects with reaction barriers.

The convergence of these approaches will enable interface-programmable catalytic models in which local electronic parameters directly predict macroscopic reactivity. A key limitation is the absence of standardized electronic and structural descriptors capable of comparing different MXene compositions and termination chemistries on a unified scale. Establishing such descriptors will accelerate rational catalyst discovery and allow generalizable design rules to emerge. Ultimately, MXenes exemplify a new paradigm of interface-governed, energy-coupled catalysis, wherein electronic mediation, interfacial polarization, and dynamic adaptability act in concert to enable selective, efficient, and durable transformations across multiple energy domains.

6. Conclusion and perspectives

6.1. A unified view of MXene catalysis

Over the past decade, MXenes have evolved from laboratory curiosities to model catalysts and prototypical platforms for understanding and controlling catalytic interfaces. Their layered architecture, tunable surface terminations, and metallic conductivity collectively endow them with an unprecedented degree of surface programmability. This review has shown that the catalytic excellence of MXenes stems not from a single structural feature, but from the synergistic interplay among three coexisting attributes: (i) electronic plasticity that enables charge redistribution and Fermi-level regulation; (ii) interfacial intelligence that governs band alignment, polarization, and reaction selectivity; and (iii) structural adaptability that preserves activity under harsh chemical and thermal environments.

Viewed through this integrated lens, MXenes bridge the long-standing gap between active-site engineering and interfacial field control, transforming catalyst design from static architectures into dynamically responsive systems. A key outcome of this perspective is that MXenes act not merely as 2D hosts, but as programmable catalytic mediators whose surface terminations, dopants, and heterointerfaces collectively dictate charge flow, intermediate stabilization, and reaction energetics across electro-, photo-, and thermochemical catalysis.

6.2. Challenges and opportunities ahead

Even with the remarkable progress achieved so far, several critical challenges (Fig. 50) must be addressed before MXene-based catalysis can reach its full potential.[254–259] One major challenge is the development of synthesis strategies that reliably produce MXenes with well-defined terminations, controllable defect populations, and reproducible catalytic surfaces, since small variations in etching conditions or precursor crystallinity can lead to significant differences in adsorption behavior and charge-transfer characteristics. These difficulties become even more pronounced when scaling MXene production, because HF-free etching, molten-salt routes, electrochemical methods, and chemical vapor deposition each face practical limitations related to throughput, by-product formation, cost, and batch-to-batch variability. Such variability complicates the integration of MXenes into structured catalytic reactors and remains a significant obstacle for consistent catalytic performance at scale.

Long-term stability presents an additional fundamental challenge. MXenes are prone to oxidation, termination depletion, hydration, and interlayer restacking under catalytic operating conditions. Recent studies increasingly indicate that stability is becoming the primary limiting factor for practical MXene catalysis, often more critical than intrinsic activity. A deeper understanding of degradation pathways and the establishment of standardized protocols for evaluating stability across electro-, photo-, and thermocatalytic conditions are urgently needed.

A further challenge arises from the difficulty of quantitatively engineering MXene-based interfaces, which is a common obstacle in elucidating heterogeneous catalytic reaction mechanisms. The catalytic behavior of MXene heterostructures depends on interfacial charge redistribution, Fermi-level equilibration, orbital hybridization, and the formation of directional electric fields at junctions, where MXenes are coupled with metals, semiconductors, or carbon materials. Although these interfacial phenomena determine activation barriers and reaction selectivity, they remain difficult to observe directly. Progress in *operando* and ultrafast spectroscopies such as XPS, XAS, DRIFTS, and fs-TAS will be essential for probing transient charge transfer, surface reconstruction, and field evolution under realistic catalytic environments. Moreover, inconsistencies in mechanistic interpretations across the literature, including the differentiation of photothermal *versus* electronic contributions and the identification of *in situ* reconstructed oxyhydroxide phases, highlight the need for more rigorous mechanistic validation.

At the same time, these challenges provide important opportunities for advancing catalysis. Precise control over composition, defects, and surface terminations can enable rational design of active sites with tunable adsorption energies and reaction pathways, facilitating selective CO_2 conversion, N_2 activation, and C–H functionalization. Data-driven discovery

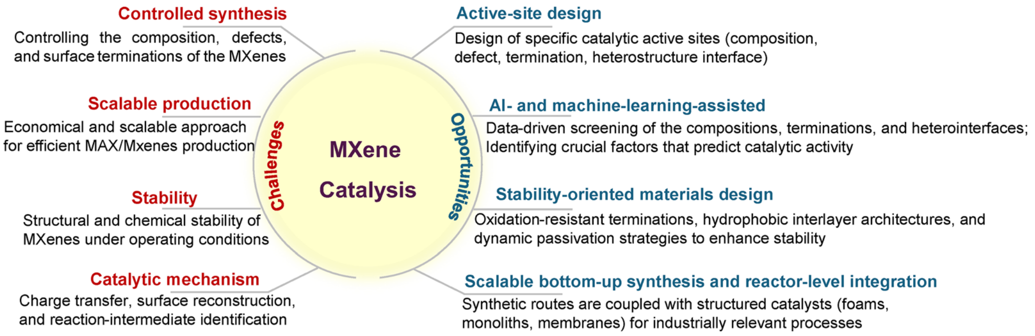

Fig. 50 Schematic diagram of challenges and opportunities in Mxene for catalysis.

offers further potential, since machine-learning-assisted screening can efficiently explore the large combinatorial space of MXene compositions, termination patterns, and heterostructure configurations to identify catalytically optimal structures. Improved durability can be pursued through stability-oriented strategies such as oxidation-resistant termination chemistries, hydrophobic interlayer architectures, intercalated spacers, and dynamic passivation approaches. Finally, the development of scalable bottom-up synthesis and reactor-level integration is emerging as a crucial direction in which CVD growth, molten-salt synthesis, and self-templating schemes are combined with structured catalytic forms such as foams, monoliths, and membranes to achieve industrially relevant performance. Overall, the future progress of MXene catalysis will depend on how dynamically evolving surfaces and interfaces govern catalytic function and on translating this understanding into practical catalyst design, operation, and scale-up.

6.3. Concluding outlook

The evolution of MXenes marks a broader transformation in the fundamental philosophy of catalysis. Their surface and interface programmability allow the design of materials that adapt and self-regulate under reaction conditions, where structural flexibility and electronic response work cooperatively rather than independently. The frontier ahead lies not merely in discovering new MXene compositions, but in mastering their dynamic interfaces as active reaction environments. Achieving this will require predictive frameworks that explicitly link termination states, band alignment, and real-time structural evolution with catalytic outcomes.

A central unresolved question is how to balance adaptability with structural stability, since the same features that enable responsive interfaces can also make MXenes susceptible to termination loss, reconstruction, and oxidation. Realizing this vision will require interdisciplinary integration that combines surface science, materials synthesis, *in situ* spectroscopy, and computational chemistry to develop predictive rules that connect electronic structure with catalytic performance. In this context, MXenes provide both a challenge and an opportunity: a challenge to unravel the complexity of adaptive interfaces, and an opportunity to create the next generation of programmable catalysts that merge structural robustness with energy responsiveness.

From a long-term perspective, advancing MXenes toward practical catalysis will depend on unifying surface design, AI-guided exploration, stability engineering, and scalable manufacturing, thereby moving MXenes from promising fundamental materials to deployable catalytic modules. This emerging paradigm not only redefines the future of MXenes but also lays the foundation for the rational design of next-generation catalytic systems.

Conflicts of interest

There are no conflicts to declare.

Data availability

The present Review has not generated new scientific data. Any issue regarding the present submission will be addressed by the corresponding authors.

Acknowledgements

Financial support by the Spanish Ministry of Science and Innovation (CEX-2021-001230-S and PID2024-161014 NB-I00 funded by MCIN/AEI/10.13039/501100011033), Generalitat Valenciana (CIPROM/2024/071) and Advanced Materials programme Graphica MFA/2022/023 with funding from European Union NextGenerationEU PRTR-C17.I1) and European Commission through the ERC Adv. Grant 101141466 DISCOVERY is gratefully acknowledged. F.X. and J.Y. thank the support by the National Natural Science Foundation of China (22378371, 52003213, 22361142704, 22238009, U24A2071, and W2512051), the Natural Science Foundation of Hubei Province of China (2025AFD020, 2022CFA001), and the Fundamental Research Funds for the Central Universities, China University of Geosciences (Wuhan) (No. CUG22061).

References

1 B. W. J. Chen, L. Xu and M. Mavrikakis, *Chem. Rev.*, 2021, **121**, 1007–1048.
2 C. Vogt and B. M. Weckhuysen, *Nat. Rev. Chem.*, 2022, **6**, 89–111.

3 F. Zaera, *Chem. Soc. Rev.*, 2013, **42**, 2746–2762.

4 A. Corma, H. García and F. X. Llabrés I Xamena, *Chem. Rev.*, 2010, **110**, 4606–4655.

5 A. Corma and H. García, *Chem. Rev.*, 2003, **103**, 4307–4366.

6 Q. Fu and X. Bao, *Chem. Soc. Rev.*, 2017, **46**, 1842–1874.

7 D. Deng, K. S. Novoselov, Q. Fu, N. Zheng, Z. Tian and X. Bao, *Nat. Nanotechnol.*, 2016, **11**, 218–230.

8 S. Navalon, A. Dhakshinamoorthy, M. Alvaro and H. Garcia, *Chem. Rev.*, 2014, **114**, 6179–6212.

9 M. Naguib, V. N. Mochalin, M. W. Barsoum and Y. Gogotsi, *Adv. Mater.*, 2014, **26**, 992–1005.

10 A. VahidMohammadi, J. Rosen and Y. Gogotsi, *Science*, 2021, **372**, eabf1581.

11 M. Naguib, M. Kurtoglu, V. Presser, J. Lu, J. Niu, M. Heon, L. Hultman, Y. Gogotsi and M. W. Barsoum, *Adv. Mater.*, 2011, **23**, 4207.

12 Z. Ling, C. E. Ren, M.-Q. Zhao, J. Yang, J. M. Giammarco, J. Qiu, M. W. Barsoum and Y. Gogotsi, *Proc. Natl. Acad. Sci. U. S. A.*, 2014, **111**, 16676–16681.

13 J. Yan, C. E. Ren, K. Maleski, C. B. Hatter, B. Anasori, P. Urbankowski, A. Sarycheva and Y. Gogotsi, *Adv. Funct. Mater.*, 2017, **27**, 1701264.

14 C. (John) Zhang, B. Anasori, A. Seral-Ascaso, S. Park, N. McEvoy, A. Shmeliov, G. S. Duesberg, J. N. Coleman, Y. Gogotsi and V. Nicolosi, *Adv. Mater.*, 2017, **29**, 1702678.

15 M. Ghidiu, M. R. Lukatskaya, M. Q. Zhao, Y. Gogotsi and M. W. Barsoum, *Nature*, 2015, **516**, 78–81.

16 R. Khan, R. M. N. Kalla, T. Ramachandran, A. G. Al-Sehemi, Y. A. Kumar, P. Somu and J. Lee, *J. Alloys Compd.*, 2025, **1039**, 182874.

17 T. Y. Ma, J. L. Cao, M. Jaroniec and S. Z. Qiao, *Angew. Chem., Int. Ed.*, 2016, **55**, 1138–1142.

18 L. Zhao, B. Dong, S. Li, L. Zhou, L. Lai, Z. Wang, S. Zhao, M. Han, K. Gao, M. Lu, X. Xie, B. Chen, Z. Liu, X. Wang, H. Zhang, H. Li, J. Liu, H. Zhang, X. Huang and W. Huang, *ACS Nano*, 2017, **11**, 5800–5807.

19 K. Guan, X. Li, Q. Xie, L. Huang, H. Zhang, G. Li and W. Lei, *Chem. Eng. J.*, 2024, **492**, 151978.

20 Y. Zhao, T. Ramachandran, A. Ghosh, A. G. Al-Sehemi, Y. A. Kumar, S. S. Rao, A. K. Yadav and D. Mani, *Biomass Bioenergy*, 2025, **200**, 108052.

21 J. Liu, H. Zhang, R. Sun, Y. Liu, Z. Liu, A. Zhou and Z. Yu, *Adv. Mater.*, 2017, **29**, 1702367.

22 W.-T. Cao, F.-F. Chen, Y.-J. Zhu, Y.-G. Zhang, Y.-Y. Jiang, M.-G. Ma and F. Chen, *ACS Nano*, 2018, **12**, 4583–4593.

23 A. Iqbal, F. Shahzad, K. Hantanasirisakul, M.-K. Kim, J. Kwon, J. Hong, H. Kim, D. Kim, Y. Gogotsi and C. M. Koo, *Science*, 2020, **369**, 446–450.

24 J. Lv, T. Li, X. Li, H. Li, S. Zhang and H. Zhang, *J. Alloys Compd.*, 2025, **1043**, 184239.

25 B. Xu, M. Zhu, W. Zhang, X. Zhen, Z. Pei, Q. Xue, C. Zhi and P. Shi, *Adv. Mater.*, 2016, **28**, 3333–3339.

26 S. J. Kim, H.-J. Koh, C. E. Ren, O. Kwon, K. Maleski, S.-Y. Cho, B. Anasori, C.-K. Kim, Y.-K. Choi, J. Kim, Y. Gogotsi and H.-T. Jung, *ACS Nano*, 2018, **12**, 986–993.

27 T. Ramachandran and R. K. Raji, *J. Ind. Eng. Chem.*, 2026, **153**, 58–79.

28 I. Amin, H. van den Brekel, K. Nemani, E. Batyrev, A. de Vooys, H. van der Weijde, B. Anasori and N. R. Shiju, *ACS Appl. Mater. Interfaces*, 2022, **14**, 43749–43758.

29 J. Ding, H. Zhao and H. Yu, *Chem. Eng. J.*, 2022, **430**, 132838.

30 C. Dai, H. Lin, G. Xu, Z. Liu, R. Wu and Y. Chen, *Chem. Mater.*, 2017, **29**, 8637–8652.

31 H. Lin, Y. Wang, S. Gao, Y. Chen and J. Shi, *Adv. Mater.*, 2018, **30**, 1703284.

32 X. Zhao, L.-Y. Wang, C.-Y. Tang, X.-J. Zha, Y. Liu, B.-H. Su, K. Ke, R.-Y. Bao, M.-B. Yang and W. Yang, *ACS Nano*, 2020, **14**, 8793–8805.

33 Á. Morales-García, F. Calle-Vallejo and F. Illas, *ACS Catal.*, 2020, **10**, 13487–13503.

34 Z. Li and Y. Wu, *Small*, 2019, **15**, 1804736.

35 I. M. Chirica, A. G. Mirea, Ş. Neaţu, M. Florea, M. W. Barsoum and F. Neaţu, *J. Mater. Chem. A*, 2021, **9**, 19589–19612.

36 Y. Yang, Y. Xu, Q. Li, Y. Zhang and H. Zhou, *J. Mater. Chem. A*, 2022, **10**, 19444–19465.

37 A. Hamzehlouy and M. Soroush, *Mater. Today Catal.*, 2024, **5**, 100054.

38 M. Naguib, W. Tang, K. L. Browning, G. M. Veith, V. Maliekkal, M. Neurock and A. Villa, *ChemCatChem*, 2020, **12**, 5733–5742.

39 J. Diao, M. Hu, Z. Lian, Z. Li, H. Zhang, F. Huang, B. Li, X. Wang, D. S. Su and H. Liu, *ACS Catal.*, 2018, **8**, 10051–10057.

40 R. Thakur, M. Hoffman, A. VahidMohammadi, J. Smith, M. Chi, B. Tatarchuk, M. Beidaghi and C. A. Carrero, *ChemCatChem*, 2020, **12**, 3639–3643.

41 E. B. Deeva, A. Kurlov, P. M. Abdala, D. Lebedev, S. M. Kim, C. P. Gordon, A. Tsoukalou, A. Fedorov and C. R. Müller, *Chem. Mater.*, 2019, **31**, 4505–4513.

42 M. Sai Bhargava Reddy and S. Aich, *Coord. Chem. Rev.*, 2024, **500**, 215542.

43 J. Peng, X. Chen, W.-J. Ong, X. Zhao and N. Li, *Chem*, 2019, **5**, 18–50.

44 X. Liu, T. Chen, Y. Xue, J. Fan, S. Shen, Md. S. A. Hossain, M. A. Amin, L. Pan, X. Xu and Y. Yamauchi, *Coord. Chem. Rev.*, 2022, **459**, 214440.

45 P. Kuang, J. Low, B. Cheng, J. Yu and J. Fan, *J. Mater. Sci. Technol.*, 2020, **56**, 18–44.

46 M. Naguib, M. Kurtoglu, V. Presser, J. Lu, J. Niu, M. Heon, L. Hultman, Y. Gogotsi and M. W. Barsoum, *Adv. Mater.*, 2011, **23**, 4248–4253.

47 B. Anasori, M. R. Lukatskaya and Y. Gogotsi, *Nat. Rev. Mater.*, 2017, **2**, 16098.

48 M. W. Barsoum, *Prog. Solid State Chem.*, 2000, **28**, 201–281.

49 J. Pang, R. G. Mendes, A. Bachmatiuk, L. Zhao, H. Q. Ta, T. Gemming, H. Liu, Z. Liu and M. H. Rummeli, *Chem. Soc. Rev.*, 2019, **48**, 72–133.

50 T. Ramachandran, M. P. Pachamuthu, G. Karthikeyan, F. Hamed and M. Rezeq, *Mat. Sci. Semicond. Proc.*, 2024, **179**, 108486.

51 T. Ramachandran, F. Hamed, Y. A. Kumar, R. K. Raji and H. H. Hegazy, *J. Energy Storage*, 2023, **73**, 109299.

52 Y. A. Kumar, G. R. Reddy, T. Ramachandran, D. K. Kulurumotlakatla, H. S. M. Abd-Rabboh, A. A. Abdel Hafez, S. S. Rao and S. W. Joo, *J. Energy Storage*, 2024, **80**, 110303.

53 A. M. Bogale, T. Ramachandran, L. T. Tufa, B. B. Badassa, M. E. Suk, R. Pitcheri, J. Lee, S. K. Jilcha, A. Y. Tiky, B. A. Zenebe, N. K. Amare, M. M. Solomon and F. B. Tesema, *Mat. Sci. Semicond. Proc.*, 2025, **200**, 109958.

54 T. Ramachandran, S. Palanisamy and R. K. Raji, *J. Adv. Electro. Storage*, 2025, **1**, 1–20.

55 T. Ramachandran, N. Roy, H. H. Hegazy, I. S. Yahia, Y. A. Kumar, M. Moniruzzaman and S. W. Joo, *J. Alloys Compd.*, 2025, **1010**, 177248.

56 K. R. G. Lim, M. Shekhirev, B. C. Wyatt, B. Anasori, Y. Gogotsi and Z. W. Seh, *Nat. Synth.*, 2022, **1**, 601–614.

57 X. Zhan, C. Si, J. Zhou and Z. Sun, *Nanoscale Horiz.*, 2020, **5**, 235–258.

58 G. Murali, J. K. Reddy Modigunta, Y. H. Park, J.-H. Lee, J. Rawal, S.-Y. Lee, I. In and S.-J. Park, *ACS Nano*, 2022, **16**, 13370–13429.

59 M. Naguib, M. W. Barsoum and Y. Gogotsi, *Adv. Mater.*, 2021, **33**, 2103393.

60 Y. Wei, P. Zhang, R. A. Soomro, Q. Zhu and B. Xu, *Adv. Mater.*, 2021, **33**, 2103148.

61 M. Downes, C. E. Shuck, B. McBride, J. Busa and Y. Gogotsi, *Nat. Protoc.*, 2024, **19**, 1807–1834.

62 A. Gentile, S. Marchionna, M. Balordi, G. Pagot, C. Ferrara, V. Di Noto and R. Ruffo, *ChemElectroChem*, 2022, **9**, e202200891.

63 T. Zhang, L. Pan, H. Tang, F. Du, Y. Guo, T. Qiu and J. Yang, *J. Alloys Compd.*, 2017, **695**, 818–826.

64 A. Feng, Y. Yu, Y. Wang, F. Jiang, Y. Yu, L. Mi and L. Song, *Mater. Des.*, 2017, **114**, 161–166.

65 X. Wang, X. Shen, Y. Gao, Z. Wang, R. Yu and L. Chen, *J. Am. Chem. Soc.*, 2015, **137**, 2715–2721.

66 P. Srivastava, A. Mishra, H. Mizuseki, K.-R. Lee and A. K. Singh, *ACS Appl. Mater. Interfaces*, 2016, **8**, 24256–24264.

67 O. Mashtalir, M. Naguib, V. N. Mochalin, Y. Dall'Agnese, M. Heon, M. W. Barsoum and Y. Gogotsi, *Nat. Commun.*, 2013, **4**, 1716.

68 A. Thakur, N. Chandran, K. Davidson, A. Bedford, H. Fang, Y. Im, V. Kanduri, B. C. Wyatt, S. K. Nemani, V. Poliukhova, R. Kumar, Z. Fakhraai and B. Anasori, *Small Methods*, 2023, **7**, 2300030.

69 S. Wang, F. Wang, Y. Jin, X. Meng, B. Meng, N. Yang, J. Sunarso and S. Liu, *J. Membr. Sci.*, 2021, **638**, 119697.

70 C. Huang, S. Shi and H. Yu, *ACS Energy Lett.*, 2021, **6**, 3464–3472.

71 Y. Wang, J. Fu, J. Xu, H. Hu and D. Ho, *ACS Appl. Mater. Interfaces*, 2023, **15**, 12232–12239.

72 Y. Wang, B. Zhou, Q. Tang, Y. Yang, B. Pu, J. Bai, J. Xu, Q. Feng, Y. Liu and W. Yang, *Adv. Mater.*, 2024, **36**, 2410736.

73 P. Urbankowski, B. Anasori, T. Makaryan, D. Er, S. Kota, P. L. Walsh, M. Zhao, V. B. Shenoy, M. W. Barsoum and Y. Gogotsi, *Nanoscale*, 2016, **8**, 11385–11391.

74 T. Li, L. Yao, Q. Liu, J. Gu, R. Luo, J. Li, X. Yan, W. Wang, P. Liu, B. Chen, W. Zhang, W. Abbas, R. Naz and D. Zhang, *Angew. Chem., Int. Ed.*, 2018, **57**, 6115–6119.

75 J. D. Gouveia and J. R. B. Gomes, *Catal. Today*, 2023, **424**, 113848.

76 M. Li, J. Lu, K. Luo, Y. Li, K. Chang, K. Chen, J. Zhou, J. Rosen, L. Hultman, P. Eklund, P. O. Å. Persson, S. Du, Z. Chai, Z. Huang and Q. Huang, *J. Am. Chem. Soc.*, 2019, **141**, 4730–4737.

77 Y. Li, H. Shao, Z. Lin, J. Lu, L. Liu, B. Duployer, P. O. Å. Persson, P. Eklund, L. Hultman, M. Li, K. Chen, X.-H. Zha, S. Du, P. Rozier, Z. Chai, E. Raymundo-Piñero, P.-L. Taberna, P. Simon and Q. Huang, *Nat. Mater.*, 2020, **19**, 894–899.

78 Y. Guo, X. Zhang, S. Jin, Q. Xia, Y. Chang, L. Wang and A. Zhou, *J. Adv. Ceram.*, 2023, **12**, 1889–1901.

79 W. Sun, S. A. Shah, Y. Chen, Z. Tan, H. Gao, T. Habib, M. Radovic and M. J. Green, *J. Mater. Chem. A*, 2017, **5**, 21663–21668.

80 M. Shen, W. Jiang, K. Liang, S. Zhao, R. Tang, L. Zhang and J. Wang, *Angew. Chem., Int. Ed.*, 2021, **60**, 27013–27018.

81 S.-Y. Pang, Y.-T. Wong, S. Yuan, Y. Liu, M.-K. Tsang, Z. Yang, H. Huang, W.-T. Wong and J. Hao, *J. Mater. Chem. A*, 2019, **141**, 9610–9616.

82 X. Zhang, W. Zhang and H. Zhao, *Ultrason. Sonochem.*, 2022, **86**, 106024.

83 Y. Liu, Q. Tang, M. Xu, J. Ren, C. Guo, C. Chen, W. Geng, W. Lei, X. Zhao and D. Liu, *Chem. Eng. J.*, 2023, **468**, 143439.

84 R. Ramírez, A. Melillo, S. Osella, A. M. Asiri, H. Garcia and A. Primo, *Small Methods*, 2023, **7**, 2300063.

85 R. Ramírez-Grau, M. Cabrero-Antonino, H. García and A. Primo, *Appl. Catal., B*, 2024, **341**, 123316.

86 X. Xiao, H. Yu, H. Jin, M. Wu, Y. Fang, J. Sun, Z. Hu, T. Li, J. Wu, L. Huang, Y. Gogotsi and J. Zhou, *ACS Nano*, 2017, **11**, 2180–2186.

87 C. Xu, L. Wang, Z. Liu, L. Chen, J. Guo, N. Kang, X.-L. Ma, H.-M. Cheng and W. Ren, *Nat. Mater.*, 2015, **14**, 1135–1141.

88 D. Geng, X. Zhao, L. Li, P. Song, B. Tian, W. Liu, J. Chen, D. Shi, M. Lin, W. Zhou and K. P. Loh, *2D Mater.*, 2016, **4**, 011012.

89 D. Wang, C. Zhou, A. S. Filatov, W. Cho, F. Lagunas, M. Wang, S. Vaikuntanathan, C. Liu, R. F. Klie and D. V. Talapin, *Science*, 2023, **379**, 1242–1247.

90 T. Ramachandran, R. M. N. Kalla, R. Khan, A. Ghosh, Y. A. Kumar, J. Lee and K. V. V. C. Mouli, *Surf. Interface*, 2025, **72**, 107420.

91 M. Sokol, V. Natu, S. Kota and M. W. Barsoum, *Trends Chem*, 2019, **1**, 210–223.

92 X. Jiang, A. V. Kuklin, A. Baev, Y. Ge, H. Ågren, H. Zhang and P. N. Prasad, *Phys. Rep.*, 2020, **848**, 1–58.

93 P. Kuang, Z. Ni, J. Yu and J. Low, *Mater. Rep. Energy*, 2022, **2**, 100081.

94 T. Schultz, N. C. Frey, K. Hantanasirisakul, S. Park, S. J. May, V. B. Shenoy, Y. Gogotsi and N. Koch, *Chem. Mater.*, 2019, **31**, 6590–6597.

95 L. Tian, F. Liang, L. Dong, J. Li, Q. Jia, H. Zhang, S. Yan and S. Zhang, *J. Am. Ceram. Soc.*, 2021, **104**, 1110–1119.

96 R. Ibragimova, P. Rinke and H.-P. Komsa, *Chem. Mater.*, 2022, **34**, 2896–2906.

97 E. Marquis, F. Benini, B. Anasori, A. Rosenkranz and M. C. Righi, *Nano Converg.*, 2023, **10**, 16.

98 T. Hu, J. Yang and X. Wang, *Phys. Chem. Chem. Phys.*, 2017, **19**, 31773–31780.

99 X. Bai and J. Guan, *Small Struct.*, 2023, **4**, 2200354.

100 Y. Gao, Z. Tang, X. Chen, J. Yan, Y. Jiang, J. Xu, Z. Tao, L. Wang, Z. Liu and G. Wang, *Aggregate*, 2023, **4**, e248.

101 L. Tian, J. Li, F. Liang, S. Chang, H. Zhang, M. Zhang and S. Zhang, *J. Colloid Interface Sci.*, 2019, **536**, 664–672.

102 X. Zhang, T. Zhang, J. Xiao, Q. Jin, Z. Wang, C. Zhang, S. Fu and H. Gao, *J. Colloid Interface Sci.*, 2023, **630**, 502–511.

103 P. Nikhil, S. Vasanth, N. Ponpandian and C. Viswanathan, *J. Energy Storage*, 2023, **72**, 108414.

104 S. Zhao, H.-B. Zhang, J.-Q. Luo, Q.-W. Wang, B. Xu, S. Hong and Z.-Z. Yu, *ACS Nano*, 2018, **12**, 11193–11202.

105 Y.-Z. Zhang, J. K. El-Demellawi, Q. Jiang, G. Ge, H. Liang, K. Lee, X. Dong and H. N. Alshareef, *Chem. Soc. Rev.*, 2020, **49**, 7229–7251.

106 H. Lin, S. Gao, C. Dai, Y. Chen and J. Shi, *J. Am. Chem. Soc.*, 2017, **139**, 16235–16247.

107 R. Li, L. Zhang, L. Shi and P. Wang, *ACS Nano*, 2017, **11**, 3752–3759.

108 J. Qu, G. Zhou, M. Zhang, L. Shang and W. Yu, *Sol. Energy Mater. Sol. Cells*, 2023, **251**, 112164.

109 C. Tsounis, P. V. Kumar, H. Masood, R. P. Kulkarni, G. S. Gautam, C. R. Müller, R. Amal and D. A. Kuznetsov, *Angew. Chem., Int. Ed.*, 2023, **62**, e202210828.

110 Y.-J. Wan, K. Rajavel, X.-M. Li, X.-Y. Wang, S.-Y. Liao, Z.-Q. Lin, P.-L. Zhu, R. Sun and C.-P. Wong, *Chem. Eng. J.*, 2021, **408**, 127303.

111 A. Dhakshinamoorthy, R. Ramírez-Grau, H. Garcia and A. Primo, *Chem. Eur. J.*, 2024, **30**, e202400576.

112 D. D. Kruger, H. García and A. Primo, *Adv. Sci.*, 2024, **11**, 2307106.

113 M. Smirnova, B. Scheibe, R. Ramírez-Grau, H. García and A. Lewandowska-Andralojc, *Int. J. Hydrogen Energy*, 2024, **88**, 1098–1107.

114 R. Ramírez Grau, P. Garcia-Aznar, G. Sastre, S. Goberna-Ferrón, O. Pavel, A. Tirsoaga, B. Cojocaru, D. G. Popescu, V. I. Parvulescu, A. Primo and H. García, *J. Am. Chem. Soc.*, 2025, **147**, 3315–3332.

115 R. Ramírez-Grau, M. Cabrero-Antonino, F. Rey Cortes, G. Mínguez-Vega, M. G. Quesne, C. R. A. Catlow, J. A. Mata, H. García and A. Primo, *Int. J. Hydrogen Energy*, 2025, **193**, 152298.

116 C. E. Ren, M. Q. Zhao, T. Makaryan, J. Halim, M. Boota, S. Kota, B. Anasori, M. W. Barsoum and Y. Gogotsi, *ChemElectroChem*, 2016, **3**, 689–693.

117 S. Shi, B. Qian, X. Wu, H. Sun, H. Wang, H. Zhang, Z. Yu and T. P. Russell, *Angew. Chem., Int. Ed.*, 2019, **58**, 18171–18176.

118 Y. Deng, T. Shang, Z. Wu, Y. Tao, C. Luo, J. Liang, D. Han, R. Lyu, C. Qi, W. Lv, F. Kang and Q. Yang, *Adv. Mater.*, 2019, **31**, 1902432.

119 D. Ontiveros, F. Viñes and C. Sousa, *J. Mater. Chem. A*, 2023, **11**, 13754–13764.

120 D. Ontiveros, S. Vela, F. Viñes and C. Sousa, *ACS Catal.*, 2025, **15**, 14403–14413.

121 A. Shayesteh Zeraati, S. A. Mirkhani, P. Sun, M. Naguib, P. V. Braun and U. Sundararaj, *Nanoscale*, 2021, **13**, 3572–3580.

122 A. Agresti, A. Pazniak, S. Pescetelli, A. Di Vito, D. Rossi, A. Pecchia, M. Auf der Maur, A. Liedl, R. Larciprete, D. V. Kuznetsov, D. Saranin and A. Di Carlo, *Nat. Mater.*, 2019, **18**, 1228–1234.

123 L. Zhao and B. Li, *Tungsten*, 2020, **2**, 176–193.

124 Z. W. Seh, K. D. Fredrickson, B. Anasori, J. Kibsgaard, A. L. Strickler, M. R. Lukatskaya, Y. Gogotsi, T. F. Jaramillo and A. Vojvodic, *ACS Energy Lett.*, 2016, **1**, 589–594.

125 Y. Guan, Y. Cong, R. Zhao, K. Li, X. Li, H. Zhu, Q. Zhang, Z. Dong and N. Yang, *Small*, 2023, **19**, 2301276.

126 M. Han, K. Maleski, C. E. Shuck, Y. Yang, J. T. Glazar, A. C. Foucher, K. Hantanasirisakul, A. Sarycheva, N. C. Frey, S. J. May, V. B. Shenoy, E. A. Stach and Y. Gogotsi, *J. Am. Chem. Soc.*, 2020, **142**, 19110–19118.

127 B. C. Wyatt, Y. Yang, P. P. Michałowski, T. Parker, Y. Morency, F. Urban, G. Kadagishvili, M. Tanwar, S. P. Muhoza, S. K. Nemani, A. Bedford, H. Fang, Z. D. Hood, J. Jang, K. Kamath, B. G. Wright, R. Disko, A. Thakur, S. Han, N. Ghosh, X. Xu, Z. Fakhraai, Y. Gogotsi, A. Vojvodic, D. Jiang and B. Anasori, *Science*, 2025, **389**, 1054–1058.

128 S. K. Nemani, B. Zhang, B. C. Wyatt, Z. D. Hood, S. Manna, R. Khaledialidusti, W. Hong, M. G. Sternberg, S. K. R. S. Sankaranarayanan and B. Anasori, *ACS Nano*, 2021, **15**, 12815–12825.

129 B. Anasori, Y. Xie, M. Beidaghi, J. Lu, B. C. Hosler, L. Hultman, P. R. C. Kent, Y. Gogotsi and M. W. Barsoum, *ACS Nano*, 2015, **9**, 9507–9516.

130 W. Hong, B. C. Wyatt, S. K. Nemani and B. Anasori, *MRS Bull*, 2020, **45**, 850–861.

131 T. L. Tan, H. M. Jin, M. B. Sullivan, B. Anasori and Y. Gogotsi, *ACS Nano*, 2017, **11**, 4407–4418.

132 B. Ahmed, A. El Ghazaly and J. Rosen, *Adv. Funct. Mater.*, 2020, **30**, 2000894.

133 Y. Wen, T. E. Rufford, X. Chen, N. Li, M. Lyu, L. Dai and L. Wang, *Nano Energy*, 2017, **38**, 368–376.

134 H. Kumar, N. C. Frey, L. Dong, B. Anasori, Y. Gogotsi and V. B. Shenoy, *ACS Nano*, 2017, **11**, 7648–7655.

135 C. Lu, L. Yang, B. Yan, L. Sun, P. Zhang, W. Zhang and Z. Sun, *Adv. Funct. Mater.*, 2020, **30**, 2000852.

136 L. Gao, W. Bao, A. V. Kuklin, S. Mei, H. Zhang and H. Ågren, *Adv. Mater.*, 2021, **33**, 2004129.

137 A. N. Enyashin and A. L. Ivanovskii, *J. Solid State Chem.*, 2013, **207**, 42–48.

138 J. Zhu, M. Wang, M. Lyu, Y. Jiao, A. Du, B. Luo, I. Gentle and L. Wang, *ACS Appl. Nano Mater.*, 2018, **1**, 6854–6863.

139 T. Zhang, C. E. Shuck, K. Shevchuk, M. Anayee and Y. Gogotsi, *J. Am. Chem. Soc.*, 2023, **145**, 22374–22383.

140 X. Li, Z. Huang, C. E. Shuck, G. Liang, Y. Gogotsi and C. Zhi, *Nat. Rev. Mater.*, 2022, **6**, 389–404.

141 V. Natu and M. W. Barsoum, *J. Phys. Chem. C*, 2023, **127**, 20197–20206.
142 T. Bashir, S. A. Ismail, J. Wang, W. Zhu, J. Zhao and L. Gao, *J. Energy Chem.*, 2023, **76**, 90–104.
143 T. Su, X. Ma, J. Tong, H. Ji, Z. Qin and Z. Wu, *J. Mater. Chem. A*, 2022, **10**, 10265–10296.
144 M. Mozafari and M. Soroush, *Mater. Adv.*, 2021, **2**, 7277–7307.
145 J. Sun, B. Liu, Q. Zhao, C. H. Kirk and J. Wang, *Adv. Mater.*, 2023, **35**, 2306072.
146 M. Jiang, D. Wang, Y. Kim, C. Duan, D. V. Talapin and C. Zhou, *Angew. Chem., Int. Ed.*, 2024, **63**, e202409480.
147 H.-W. Wang, M. Naguib, K. Page, D. J. Wesolowski and Y. Gogotsi, *Chem. Mater.*, 2016, **28**, 349–359.
148 Q. Peng, J. Guo, Q. Zhang, J. Xiang, B. Liu, A. Zhou, R. Liu and Y. Tian, *J. Am. Chem. Soc.*, 2014, **136**, 4113–4116.
149 T. Zhang, L. Chang, X. Zhang, H. Wan, N. Liu, L. Zhou and X. Xiao, *Nat. Commun.*, 2022, **13**, 6731.
150 V. Kamysbayev, A. S. Filatov, H. Hu, X. Rui, F. Lagunas, D. Wang, R. F. Klie and D. V. Talapin, *Science*, 2020, **369**, 979–983.
151 C. Zhou, D. Wang, F. Lagunas, B. Atterberry, M. Lei, H. Hu, Z. Zhou, A. S. Filatov, D. Jiang, A. J. Rossini, R. F. Klie and D. V. Talapin, *Nat. Chem.*, 2023, **15**, 1722–1729.
152 D. Li, W. Zheng, S. M. Gali, K. Sobczak, M. Horák, J. Polčák, N. Lopatik, Z. Li, J. Zhang, D. Sabaghi, S. Zhou, P. P. Michałowski, E. Zschech, E. Brunner, M. Donten, T. Šikola, M. Bonn, H. I. Wang, D. Beljonne, M. Yu and X. Feng, *Nat. Mater.*, 2024, **23**, 1085–1092.
153 I. Persson, J. Halim, H. Lind, T. W. Hansen, J. B. Wagner, L. Näslund, V. Darakchieva, J. Palisaitis, J. Rosen and P. O. Å. Persson, *Adv. Mater.*, 2019, **31**, 1805472.
154 I. Persson, J. Halim, T. W. Hansen, J. B. Wagner, V. Darakchieva, J. Palisaitis, J. Rosen and P. O. Å. Persson, *Adv. Funct. Mater.*, 2020, **30**, 1909005.
155 H. Zhou, Z. Chen, E. Kountoupi, A. Tsoukalou, P. M. Abdala, P. Florian, A. Fedorov and C. R. Müller, *Nat. Commun.*, 2021, **12**, 5510.
156 R. Morales-Salvador, J. D. Gouveia, Á. Morales-García, F. Viñes, J. R. B. Gomes and F. Illas, *ACS Catal.*, 2021, **11**, 11248–11255.
157 Á. Morales-García, A. Fernández-Fernández, F. Viñes and F. Illas, *J. Mater. Chem. A*, 2018, **6**, 3381–3385.
158 J. D. Gouveia, Á. Morales-García, F. Viñes, J. R. B. Gomes and F. Illas, *ACS Catal.*, 2020, **10**, 5049–5056.
159 A. Jurado, Á. Morales-García, F. Viñes and F. Illas, *ACS Catal.*, 2022, **12**, 15658–15667.
160 Y. Jiao, H. Li, Y. Jiao and S.-Z. Qiao, *J. Am. Chem. Soc.*, 2023, **145**, 15572–15580.
161 J. L. Hart, K. Hantanasirisakul, A. C. Lang, B. Anasori, D. Pinto, Y. Pivak, J. T. van Omme, S. J. May, Y. Gogotsi and M. L. Taheri, *Nat. Commun.*, 2019, **10**, 522.
162 X. Sang, Y. Xie, M.-W. Lin, M. Alhabeb, K. L. Van Aken, Y. Gogotsi, P. R. C. Kent, K. Xiao and R. R. Unocic, *ACS Nano*, 2016, **10**, 9193–9200.
163 T. A. Le, Q. V. Bui, N. Q. Tran, Y. Cho, Y. Hong, Y. Kawazoe and H. Lee, *ACS Sustain. Chem. Eng.*, 2019, **7**, 16879–16888.
164 Y. Wen, R. Li, J. Liu, Z. Wei, S. Li, L. Du, K. Zu, Z. Li, Y. Pan and H. Hu, *J. Colloid Interface Sci.*, 2021, **604**, 239–247.
165 Y. Qi, X. Hou, Z. He, F. He, T. Wei, G. Meng, H. Hu, Q. Liu, G. Hu and X. Liu, *Chem. Commun.*, 2024, **60**, 8728–8731.
166 H. Gu, X. Li, J. Zhang and W. Chen, *Small*, 2022, **18**, 2105883.
167 H. Bao, Y. Qiu, X. Peng, J. Wang, Y. Mi, S. Zhao, X. Liu, Y. Liu, R. Cao, L. Zhuo, J. Ren, J. Sun, J. Luo and X. Sun, *Nat. Commun.*, 2021, **12**, 238.
168 D. Zhao, Z. Chen, W. Yang, S. Liu, X. Zhang, Y. Yu, W. C. Cheong, L. Zheng, F. Ren, G. Ying, X. Cao, D. Wang, Q. Peng, G. Wang and C. Chen, *J. Am. Chem. Soc.*, 2019, **141**, 4086–4093.
169 S. Park, Y.-L. Lee, Y. Yoon, S. Y. Park, S. Yim, W. Song, S. Myung, K.-S. Lee, H. Chang, S. S. Lee and K.-S. An, *Appl. Catal., B*, 2022, **304**, 120989.
170 S. Zhou, Y. Zhao, R. Shi, Y. Wang, A. Ashok, F. Héraly, T. Zhang and J. Yuan, *Adv. Mater.*, 2022, **34**, 2204388.
171 X. L. Li, W. Y. Lieu, L. Wang, D. Yan, Y. Li, T. Ghosh, Y. Li, J. Lu, Z. W. Seh and H. Y. Yang, *ACS Energy Lett.*, 2024, **9**, 4929–4938.
172 W. Peng, M. Luo, X. Xu, K. Jiang, M. Peng, D. Chen, T. Chan and Y. Tan, *Adv. Energy Mater.*, 2020, **10**, 2001364.
173 K. Yu, S. Wang, Q. Li, T. Hou, Y. Xin, R. He, W. Zhang, S. Liang, L. Wang and W. Zhu, *Nano Res.*, 2022, **15**, 2862–2869.
174 D. A. Kuznetsov, Z. Chen, P. V. Kumar, A. Tsoukalou, A. Kierzkowska, P. M. Abdala, O. V. Safonova, A. Fedorov and C. R. Müller, *J. Am. Chem. Soc.*, 2019, **141**, 17809–17816.
175 D. A. Kuznetsov, Z. Chen, P. M. Abdala, O. V. Safonova, A. Fedorov and C. R. Müller, *J. Am. Chem. Soc.*, 2021, **143**, 5771–5778.
176 P. Yang, Y. Long, W. Huang and D. Liu, *Appl. Catal., B*, 2023, **324**, 122245.
177 D. D. Kruger, J. J. Delgado, F. J. Recio, S. Goberna-Ferrón, A. Primo and H. García, *J. Mater. Chem. A*, 2024, **12**, 25291–25303.
178 J. Gu, Q. Zhu, Y. Shi, H. Chen, D. Zhang, Z. Du and S. Yang, *ACS Nano*, 2020, **14**, 891–898.
179 D. Zhang, S. Wang, R. Hu, J. Gu, Y. Cui, B. Li, W. Chen, C. Liu, J. Shang and S. Yang, *Adv. Funct. Mater.*, 2020, **30**, 2002471.
180 Y. Yue, N. Liu, W. Liu, M. Li, Y. Ma, C. Luo, S. Wang, J. Rao, X. Hu, J. Su, Z. Zhang, Q. Huang and Y. Gao, *Nano Energy*, 2018, **50**, 79–87.
181 S. Zhao, H.-B. Zhang, J.-Q. Luo, Q.-W. Wang, B. Xu, S. Hong and Z.-Z. Yu, *ACS Nano*, 2018, **12**, 11193–11202.
182 K. Li, M. Liang, H. Wang, X. Wang, Y. Huang, J. Coelho, S. Pinilla, Y. Zhang, F. Qi, V. Nicolosi and Y. Xu, *Adv. Funct. Mater.*, 2020, **30**, 2000842.
183 T. Shang, Z. Lin, C. Qi, X. Liu, P. Li, Y. Tao, Z. Wu, D. Li, P. Simon and Q. Yang, *Adv. Funct. Mater.*, 2019, **29**, 1903960.
184 A. Vaughn, J. Ball, T. Heil, D. J. Morgan, G. I. Lampronti, G. Maršalkaitė, C. L. Raston, N. P. Power and S. Kellici, *Chem. Eur. J.*, 2017, **23**, 8128–8133.

185 Z. Yang, Y. Wang, Y. Hu, Y. Zhuang, X. Ji, G. Yang and M. He, *Int. J. Biol. Macromol.*, 2023, **243**, 124828.

186 C. Wei, Q. Zhang, Z. Wang, W. Yang, H. Lu, Z. Huang, W. Yang and J. Zhu, *Adv. Funct. Mater.*, 2023, **33**, 2211889.

187 K. A. S. Usman, S. Qin, L. C. Henderson, J. Zhang, D. Y. Hegh and J. M. Razal, *Mater. Horiz.*, 2021, **8**, 2886–2912.

188 W. Peng, J. Han, Y.-R. Lu, M. Luo, T.-S. Chan, M. Peng and Y. Tan, *ACS Nano*, 2022, **16**, 4116–4125.

189 Y. Wu, W. Wei, R. Yu, L. Xia, X. Hong, J. Zhu, J. Li, L. Lv, W. Chen, Y. Zhao, L. Zhou and L. Mai, *Adv. Funct. Mater.*, 2022, **32**, 2110910.

190 Y. Li, J. Zhang, Q. Chen, X. Xia and M. Chen, *Adv. Mater.*, 2021, **33**, 2100855.

191 F. Liu, S. Jin, Q. Xia, A. Zhou and L.-Z. Fan, *J. Energy Chem.*, 2021, **62**, 220–242.

192 F. Ezzah Ab Latif, A. Numan, N. M. Mubarak, M. Khalid, E. C. Abdullah, N. A. Manaf and R. Walvekar, *Coord. Chem. Rev.*, 2022, **471**, 214755.

193 J. Jiang, F. Li, J. Zou, S. Liu, J. Wang, Y. Zou, K. Xiang, H. Zhang, G. Zhu, Y. Zhang, X. Fu and J.-P. Hsu, *Sci. China Mater.*, 2022, **65**, 2895–2910.

194 Y. Shi, Z. Du and S. Yang, *Adv. Funct. Mater.*, 2024, **34**, 2404653.

195 W. Kong, J. Deng and L. Li, *J. Mater. Chem. A*, 2022, **10**, 14674–14691.

196 Q. Zhang, J. Wang, Q. Yu, Q. Li, R. Fan, C. Li, Y. Fan, C. Zhao, W. Cheng, P. Ji, J. Sheng, C. Zhang, S. Xie, G. Henkelman and H. Li, *Nat. Synth.*, 2024, **4**, 252–261.

197 Z. Cui, P. Zhao, H. Wang, C. Li, W. Peng, X. Fan and J. Liu, *Appl. Catal., B*, 2024, **348**, 123862.

198 Z. Cui, P. Zhao, H. Wang, C. Li, W. Peng and J. Liu, *Adv. Funct. Mater.*, 2024, **34**, 2410941.

199 W. Chen, P. Li, J. Yu, P. Cui, X. Yu, W. Song and C. Cao, *Nano Res.*, 2022, **15**, 9544–9553.

200 Z. Li, L. Yu, C. Milligan, T. Ma, L. Zhou, Y. Cui, Z. Qi, N. Libretto, B. Xu, J. Luo, E. Shi, Z. Wu, H. Xin, W. N. Delgass, J. T. Miller and Y. Wu, *Nat. Commun.*, 2018, **9**, 5258.

201 Z. Li, Y. Xiao, P. R. Chowdhury, Z. Wu, T. Ma, J. Z. Chen, G. Wan, T.-H. Kim, D. Jing, P. He, P. J. Potdar, L. Zhou, Z. Zeng, X. Ruan, J. T. Miller, J. P. Greeley, Y. Wu and A. Varma, *Nat. Catal.*, 2021, **4**, 882–891.

202 J. Low, L. Zhang, T. Tong, B. Shen and J. Yu, *J. Catal.*, 2018, **361**, 255–266.

203 F. Xu, W. Mei, P. Hu, L. Zheng, J. Zhang, H. Cao, H. García and J. Yu, *Angew. Chem., Int. Ed.*, 2025, **64**, e202513364.

204 Q. Xu, L. Zhang, B. Cheng, J. Fan and J. Yu, *Chem*, 2020, **6**, 1543–1559.

205 F. He, B. Zhu, B. Cheng, J. Yu, W. Ho and W. Macyk, *Appl. Catal., B*, 2020, **272**, 119006.

206 L. Zhang, J. Zhang and J. Yu, *Chem*, 2025, 102719.

207 S. Cao, B. Shen, T. Tong, J. Fu and J. Yu, *Adv. Funct. Mater.*, 2018, **28**, 1800136.

208 J. Li, Z. Li, X. Liu, C. Li, Y. Zheng, K. W. K. Yeung, Z. Cui, Y. Liang, S. Zhu, W. Hu, Y. Qi, T. Zhang, X. Wang and S. Wu, *Nat. Commun.*, 2021, **12**, 1224.

209 Y. Liu, P. Zhang, N. Sun, B. Anasori, Q. Zhu, H. Liu, Y. Gogotsi and B. Xu, *Adv. Mater.*, 2018, **30**, 1707334.

210 P. Zhang, N. Sun, R. A. Soomro, S. Yue, Q. Zhu and B. Xu, *ACS Appl. Energy Mater.*, 2021, **4**, 11844–11853.

211 T. Zhou, C. Wu, Y. Wang, A. P. Tomsia, M. Li, E. Saiz, S. Fang, R. H. Baughman, L. Jiang and Q. Cheng, *Nat. Commun.*, 2020, **11**, 2077.

212 X. Gao, X. Du, T. S. Mathis, M. Zhang, X. Wang, J. Shui, Y. Gogotsi and M. Xu, *Nat. Commun.*, 2020, **11**, 6160.

213 P. Yan, R. Zhang, J. Jia, C. Wu, A. Zhou, J. Xu and X. Zhang, *J. Power Sources*, 2015, **284**, 38–43.

214 H. Li, R. Chen, M. Ali, H. Lee and M. J. Ko, *Adv. Funct. Mater.*, 2020, **30**, 2002739.

215 X. Wang, S. Wang, J. Qin, X. Xie, R. Yang and M. Cao, *Inorg. Chem.*, 2019, **58**, 16524–16536.

216 X. Lu, J. Zhu, W. Wu and B. Zhang, *Electrochim. Acta*, 2017, **228**, 282–289.

217 K. Nakajima, R. Noma, M. Kitano and M. Hara, *J. Phys. Chem. C*, 2013, **117**, 16028–16033.

218 Y. Xu, Y. Yang, M. Wu, X. Yang, X. Bie, S. Zhang, Q. Li, Y. Zhang, C. Zhang, R. E. Przekop, B. Sztorch, D. Brzakalski and H. Zhou, *Acta Phys.-Chim. Sin.*, 2024, **40**, 2304003.

219 A. Anouar, E. Romero Salicio, P. García-Aznar, A. Grirrane, A. Forneli, G. Sastre, H. Garcia and A. Primo, *J. Catal.*, 2025, **450**, 116328.

220 O. Pavel, A. Tirsoaga, B. Cojocaru, D. Popescu, R. Ramírez-Grau, P. González-Durán, P. García-Aznar, L. Tian, G. Sastre, A. Primo, V. Parvulescu and H. Garcia, *EES Catal.*, 2025, **3**, 856–869.

221 Y. Li, B. Lan, B. Guan, C. Dai, F. Zhang and Z. Lin, *Acta Phys.-Chim. Sin.*, 2024, **40**, 2306031.

222 R. Abedi, G. Barati Darband, A. R. Oveisi, S. Daliran, A. Fathollahi and H. Garcia, *Coord. Chem. Rev.*, 2026, **549**, 217371.

223 G. Gao, A. P. O'Mullane and A. Du, *ACS Catal.*, 2017, **7**, 494–500.

224 Q. Zhao, C. Zhang, R. Hu, Z. Du, J. Gu, Y. Cui, X. Chen, W. Xu, Z. Cheng, S. Li, B. Li, Y. Liu, W. Chen, C. Liu, J. Shang, L. Song and S. Yang, *ACS Nano*, 2021, **15**, 4927–4936.

225 H. Zhang, G. Yang, X. Zuo, H. Tang, Q. Yang and G. Li, *J. Mater. Chem. A*, 2016, **4**, 12913–12920.

226 E. Balcı, Ü. Ö. Akkuş and S. Berber, *J. Mater. Chem. C*, 2017, **5**, 5956–5961.

227 Z. Guo, J. Zhou, L. Zhu and Z. Sun, *J. Mater. Chem. A*, 2016, **4**, 11446–11452.

228 C. Xie, L. Xu, J. Peng, L. Zhang, X. Wang, J. Deng, M. Capron and V. Ordomsky, *Adv. Funct. Mater.*, 2023, **33**, 2213782.

229 A. Sfeir, C. E. Shuck, A. Fadel, M. Marinova, H. Vezin, J.-P. Dacquin, Y. Gogotsi, S. Royer and S. Laassiri, *J. Am. Chem. Soc.*, 2024, **146**, 20033–20044.

230 R. Liu, P. Wang, X. Wang, F. Chen and H. Yu, *Acta Phys.-Chim. Sin.*, 2025, **41**, 100137.

231 W. Gao, Y. Liu, C. Chen, Z. Lian, R. Ye, C. Qi and J. Hu, *Chin. J. Catal.*, 2025, **74**, 319–328.

232 M. Cabrero-Antonino, A. Uscategui-Linares, R. Ramírez-Grau, P. García-Aznar, G. Sastre, J. Zhang, S. Goberna-Ferrón, J. Albero, J. Yu, H. García, F. Xu and A. Primo, *Angew. Chem., Int. Ed.*, 2025, **64**, e202503860.

233 W. Sun, Y. Wang, K. Xiang, S. Bai, H. Wang, J. Zou, Arramel and J. Jiang, *Acta Phys.-Chim. Sin.*, 2024, **40**, 2308015.

234 H. Zou, B. He, P. Kuang, J. Yu and K. Fan, *ACS Appl. Mater. Interfaces*, 2018, **10**, 22311–22319.

235 Y. Chen, H. Yao, F. Kong, H. Tian, G. Meng, S. Wang, X. Mao, X. Cui, X. Hou and J. Shi, *Appl. Catal., B*, 2021, **297**, 120474.

236 P. Kuang, M. He, B. Zhu, J. Yu, K. Fan and M. Jaroniec, *J. Catal.*, 2019, **375**, 8–20.

237 Y. Cai and F. X. Xiao, *Acta Phys.-Chim. Sin.*, 2024, **40**, 2306048.

238 Q. Li, H. Zhang, H. Gu, Y. Cui, R. Gao and W. L. Dai, *Acta Phys.-Chim. Sin.*, 2025, **41**, 100031.

239 C. Liu, H. Yu, J. Li, X. Yu, Z. Yu, Y. Song, F. Zhang, Q. Zhang and Z. Zou, *Acta Phys.-Chim. Sin.*, 2025, **41**, 100075.

240 M. Xu, Z. Li, R. Shen, X. Zhang, Z. Zhang, P. Zhang and X. Li, *Chin. J. Catal.*, 2025, **70**, 431–443.

241 S. Mansoor, Z. Hu, Y. Zhang, M. Tayyab, M. Khan, Z. Akmal, L. Zhou, J. Lei, M. Nasir and J. Zhang, *Chin. J. Catal.*, 2025, **71**, 234–245.

242 J. Ran, G. Gao, F.-T. Li, T.-Y. Ma, A. Du and S.-Z. Qiao, *Nat. Commun.*, 2017, **8**, 13907.

243 B. R. Anne, J. Kundu, M. K. Kabiraz, J. Kim, D. Cho and S. Choi, *Adv. Funct. Mater.*, 2023, **33**, 2306100.

244 B. Huang, N. Li, W.-J. Ong and N. Zhou, *J. Mater. Chem. A*, 2019, **7**, 27620–27631.

245 S. E. Midré, L. Tian, H. García, S. Goberna-Ferrón and A. Primo, *ACS Appl. Energy Mater.*, 2025, **8**, 14542–14553.

246 S. Guan, Z. Yuan, S. Zhao, Z. Zhuang, H. Zhang, R. Shen, Y. Fan, B. Li, D. Wang and B. Liu, *Angew. Chem., Int. Ed.*, 2024, **63**, e202408193.

247 L. Liu, S. Zheng, H. Chen, J. Cai and S. Zang, *Angew. Chem., Int. Ed.*, 2024, **63**, e202316910.

248 Z. Li, Y. Cui, Z. Wu, C. Milligan, L. Zhou, G. Mitchell, B. Xu, E. Shi, J. T. Miller, F. H. Ribeiro and Y. Wu, *Nat. Catal.*, 2018, **1**, 349–355.

249 Z. Wei, Z. Zhao, C. Qiu, S. Huang, Z. Yao, M. Wang, Y. Chen, Y. Lin, X. Zhong, X. Li and J. Wang, *Nat. Commun.*, 2023, **14**, 661.

250 C. Gu, C. Lu, Y.-X. Gao, P. Tan, S.-S. Peng, X.-Q. Liu and L.-B. Sun, *Inorg. Chem.*, 2021, **60**, 1380–1387.

251 Z. Wu, J. Shen, C. Li, C. Zhang, K. Feng, Z. Wang, X. Wang, D. M. Meira, M. Cai, D. Zhang, S. Wang, M. Chu, J. Chen, Y. Xi, L. Zhang, T.-K. Sham, A. Genest, G. Rupprechter, X. Zhang and L. He, *ACS Nano*, 2023, **17**, 1550–1559.

252 R. Tang, S. Zhou, C. Li, R. Chen, L. Zhang, Z. Zhang and L. Yin, *Adv. Funct. Mater.*, 2020, **30**, 2000637.

253 X. Wu, J. Wang, Z. Wang, F. Sun, Y. Liu, K. Wu, X. Meng and J. Qiu, *Angew. Chem., Int. Ed.*, 2021, **60**, 9416–9420.

254 Y. A. Kumar, T. Ramachandran, A. Ghosh, A. G. Al-Sehemi, N. P. Reddy and M. Moniruzzaman, *J. Energy Storage*, 2025, **121**, 116507.

255 T. Ramachandran, R. K. Raji and I. Hussain, *Sustain. Energy Fuels*, 2025, **9**, 6116–6149.

256 K. V. V. Chandra Mouli, R. M. N. Kalla, T. Ramachandran, Y. A. Kumar, M. Moniruzzaman and J. Lee, *Int. J. Hydrogen Energy*, 2024, **90**, 1–24.

257 K. V. V. Chandra Mouli, D. Mani, T. Ramachandran, Y. Anil Kumar, A. Ghosh, P. Somu and R. Mangiri, *Mater. Chem. Phys.*, 2026, **348**, 131660.

258 T. Ramachandran, R. M. N. Kalla, A. G. Al-Sehemi, Y. A. Kumar, R. Khan, A. Ghosh, S. S. Rao and J. Lee, *Colloids Surf., A*, 2025, **726**, 137844.

259 R. Mangiri, T. Ramachandran, Y. A. Kumar, A. Ghosh, A. G. Al-Sehemi, A. K. Yadav and D. Mani, *Mater. Today Chem.*, 2025, **48**, 102864.